FACULTY OF SCIENCE
UNIVERSITY OF COPENHAGEN

Ph.D Thesis

Observational signatures of near-extremal rotating black holes

Haopeng Yan

Supervisor: Niels Anne Jacob Obers

Submitted: 10/07/2020

This thesis has been submitted to the PhD School of The Faculty of Science, University of Copenhagen.

ACKNOWLEDGEMENTS

I would like to greatly thank my supervisor Prof. Niels Obers for giving me a lot of guidance, help and encouragements on the research works in this thesis and on my PhD courses and other research topics. Discussions with Niels was always very pleasant, sometimes even exciting with brainstorms. I also thank Niels for providing me interesting research projects and sharing notes with me and for providing me opportunities to participate several conferences and workshops. I also thank Niels for his help on my career. Thanks a lot.

I am grateful to my collaborators Minyong and Shupeng. It has been a pleasure to work with them.

I thank Jay and Maria for reading the manuscript of one of my publications and providing useful comments. I also thank the anonymous referees for their useful comments on the manuscripts of my publications.

I am grateful to the teachers at the high energy group for teaching me string theory and gauge/gravity duality. I am also grateful to the group journal club and seminars. I thank others who helped me on breading my knowledge.

I thank the group secretary Pia for her help on many technical things.

I thank the colleagues at NBI. In particular, I thank Lorenzo and Mattia for the good time at NBI and at Copenhagen. I thank Shanzhong for organizing joyful entertainment activities.

I thank my landlord Uncle Wang for providing me a good environment to live and for giving me many help in life.

Finally, I thank Ruipeng and my family for their endless support.

ABSTRACT

We are entering an exciting new era of imaging black holes with the help of the Event Horizon Telescope (EHT). This has stimulated many theoretical works predicting the signals that EHT may possibly observe and examining the type of properties of gravity that the signals can inform us. While these signals may in general depend on a complex nearby environment of a black hole, it is possible to expect some universal and striking signals for the case of near-extremal rotating black holes due to the existence of an enhanced conformal symmetry in the near-horizon region of such black holes. These particular signals may serve as a typical signature for identifying a near-extremal rotating black hole in the Universe. Moreover, the enhanced symmetry supplies powerful tools which enable one to do analytical computations for these interesting signals. From a practical perspective, astronomical observations have suggested that plenty of supermassive black holes are rotating very rapidly (i.e., they are in the near-extremal limit). Therefore, this thesis will focus on the optical observational signatures of high-spin black holes. In particular, we study the images of a point-like orbiting emitter (referred to as a "hot spot") near the Innermost Stable Circular Orbit (ISCO) of a high-spin black hole. Images of such an emitter may reveal important features of the black hole event horizon since the emitter resides in the near-horizon region, thus the images can further inform us of the properties of the underlying gravity theory. We analytically compute the shadow of a near-extremal rotating black hole and the optical observables of a near-ISCO hot spot. A key feature of the optical appearance of such an orbiting hot spot is that there are many images of it moving on a vertical portion of the black hole shadow and having a rich structure. The computations rely on the geometric properties of the black hole spacetime and the motion of massive particles and photons in it. Many studies on black

hole imaging are based on the assumption that the underlying gravity theory is general relativity (GR) and the motion of lights follows geodesic equations in the spacetime. Here we study alternative possibilities: a) we compute the influence of a plasma on the observational signature by taking into account its interactions with photons; b) we compute the observational signature based on gravity theories that go beyond GR, in particular the Scalar-Tensor-Vector (STVG) modified gravity (MOG) and the heterotic string theory. The obtained results may not only provide other possible templates for the EHT to test, but also propose a new way to distinguish different gravity theories.

PUBLICATIONS

[1] M. Guo, N. A. Obers, and **H. Yan**, "*Observational signatures of near-extremal Kerr-like black holes in a modified gravity theory at the Event Horizon Telescope*," *Phys. Rev.* **D98** no. 8, (2018) 084063,`arXiv:1806.05249 [gr-qc]`.

This work was published under lead-authorship of H. Y..

[2] **H. Yan**, "*Influence of a plasma on the observational signature of a high-spin Kerr black hole*," *Phys. Rev.* **D99** no. 8, (2019) 084050, `arXiv:1903.04382 [gr-qc]`.

This work was published under single-authorship of H. Y..

[3] M. Guo, S. Song, and **H. Yan**, "*Observational signature of a near-extremal Kerr-Sen black hole in the heterotic string theory*," *Phys. Rev.* **D101** no. 2, (2020) 024055, `arXiv:1911.04796 [gr-qc]`.

This work was published under lead-authorship of H. Y..

CONTENTS

1

INTRODUCTION

As predicted by Einstein's general theory of relativity (GR), black holes are extreme objects in many ways. They are the simplest objects with "no hair" while at the same time they are the most elusive objects with strange singularities and "untouchable" event horizons; apart from being fascinating mathematical, abstract objects, they are also the most compact and energetic sources in the universe so that they are the brightest "stars" in the sky—even though they themselves are invisible. Therefore, the visual appearances of black holes are very mythical, attracting a lot of attentions not only among the scientific community but also among the public.

Black hole imaging is a "source-ray-observer" problem. The light *sources* for an image of black hole are those luminous materials that illuminate this invisible black hole. The *rays* connecting light sources with an observer follow null geodesics in the exterior of the black hole and are extremely bent in the vicinity of black hole due to the large spacetime curvature. The *observer* is uaually taken to be very far away from the black hole where the spacetime is asymptotically flat. The observed images are determined by emission profiles of sources, gravitational focusing, gravitational redshifts and Doppler shifts. Roughly, a black hole casts a dark shadow in a bright background. Behaviors of photons near the black hole play a dominant role in determining the detailed structure of the black hole image. The black hole image therefore tests gravity in its strong-field regime.

In this thesis, we specifically study the images of near-extremal rotating black holes. In particular, we assume there is a point source ("hot spot") orbiting near the innermost stable circular orbit (ISCO) of the black hole which is in the near-horizon region. We analytically calculate the apparent boundary of a black hole shadow and the observables of the hot spot. Even though the spacetime geometry is determined by the underlying gravity theory, all we need for calculating the images is merely a black hole metric which solves the field equations of gravity and determines how particles and photons move. The near-horizon geometry of a near-extremal rotating black hole possesses an enhanced symmetry which strongly constrains the motion of photons [4]. Therefore, images of a near-ISCO hot spot might provide typical signals for a near-extremal rotating black hole [5]. We will consider a black hole in GR surrounded by a plasma, and we also consider black holes in two of the alternative theories to GR: the scalar-tensor-vector gravity and string theory.

Next, I briefly introduce some of the historical efforts to "see" astrophysical black holes: astronomical observations providing evidence for their existence, theoretical preparations for imaging them, and potential observational signals of high-spin black holes.

1.1 ASTRONOMICAL OBSERVATIONS OF BLACK HOLES

While the term black hole[1] was only popularized after a lecture by John Wheeler in New York in 1967, the concept of a black hole had already been proposed by John Michell [7] in 1784. Roughly speaking, a black hole is something invisible due to its strong gravity such that nothing can escape, not even light. Michell proposed such an object in the context of Newtonian gravity and named it as dark star. In the modern sense, a black hole is a region of spacetime with an *event horizon* as its boundary—a one-way membrane through which matter and light can pass only inward to the black

1 See *The Many Definitions of a Black Hole* by Erik Curiel from views of theoretical physics, astrophysics and mathematics [6].

hole region [8]. Gravity theories like GR, as well as some alternative theories of gravity, predict that there exists such spacetime solutions which contain black holes.

Black holes are highly mysterious and fascinating objects, both in the sense of mathematical objects as well as astrophysical objects. As astrophysical objects, it is a natural human curiosity to look for some observational evidences for their existence in our universe. As early as the concept of black hole was proposed, even though not in the correct sense, Michell correctly pointed out that such astrophysical objects might be detectable through the influence of their gravitational fields on nearby materials [7].

Yet some important and indirect evidences were only confirmed until around the late 1960s. Although black holes themselves are invisible, the largest luminous bodies in the universe are thought to be powered by supermassive black holes. This is because black holes are so massive that they can accrete and heat up surrounding materials to form radioactive accretion disks. Ever since the discovery of the first radio galaxy Cygnus A (Cyg A) in 1939 and the discovery of quasars in 1950s, many other observations of active galactic nuclei (AGN) indicated that [9, 10] there exist a large amount of supermassive black holes (10^6 to 10^{10} Solar masses), each of them residing in the center of an AGN. Besides supermassive black holes, since the discovery of the first bright X-ray point source Cygnus X-1 (Cyg X-1) in 1964, many observations of X-ray binaries suggested that [11, 12] there are also a large number of stellar-mass black holes (3 to 100 Solar masses), each in a X-ray binary. Additionally, since 1995, astronomers have tracked trajectories of stars orbiting an invisible central object in our own Milky Way and found that these orbits are Keplerian orbits with a common focus, suggesting that the central object is a supermassive black hole [13]. These evidences altogether show that black holes are common astrophysical objects in our universe[2].

Thanks to the advanced technologies and their applications to observational facilities, there have been direct and spectacular observations in the past few years, including not only electromagnetic

2 See recent reviews about astrophysical black holes from [14, 15].

wave observations but also gravitational wave observations. In September 2015, the Laser Interferometer Gravitational-Wave Observatory (LIGO) collaboration detected directly the first-ever gravitational waves emitted from binary black hole coalescence [16]. Since then, LIGO/Virgo collaborations detected more coalescence events of stellar-mass black hole binaries [17, 18, 19, 20]. In April 2019, the Event Horizon Telescope (EHT) collaboration announced the first-ever image of the supermassive black hole M87* in the center of the giant elliptical galaxy Messier 87 (M87), which is the strongest evidence to date for the existence of a supermassive black hole [21, 22, 23, 24, 25, 26].

Are these evidences enough to convince ourselves that they are really black holes? Probably not unless we examine very carefully the defining feature of a black hole, the event horizon [27, 28]. Strictly speaking, the "black holes" we have discussed are technically only candidates of black holes [29]. Nevertheless, we can safely say that black hole models are the best interpretations for such massive and compact candidates even though there are still possibilities for some alternatives such as boson stars [30] or gravastars [31]. Fortunately, the LIGO/Virgo observations and the EHT observations open tantalizingly new windows for further tests. While LIGO/Virgo would detect more transient merging events to collect more data case by case, the EHT makes it possible to measure the same targets repeatedly, thus to confirm results and explore more details.

Even if they may eventually be confirmed to be black holes, it is more difficult to tell them apart from black holes in GR or those arising in alternative theories of gravity. Since gravity theory plays a fundamental role in theoretical physics, it is essential to test these gravitational theories. While there are abundant and sufficient tests in the weak field regime, testing the strong field regime is an important avenue. Therefore, we need to probe closer and closer to the event horizon where the gravity is relatively stronger. Hopefully, the EHT presents a new way to explore gravity in this extreme limit which was not accessible before [21]. Instead of treating black holes as point-like objects, like in previous electromagnetic wave observations and gravitational wave observations, the EHT zooms into the very centre of an AGN and observes a black hole at the *event-horizon-scale*.

The main concern of this doctoral thesis is the observational signatures of near-extremal rotating black holes in GR or beyond GR at the EHT. I will then briefly introduce the EHT instrument and the first EHT image, as well as its possible improvement in the future.

The EHT is an Earth-sized virtual telescope consisting of a global network of radio telescopes, see Fig. 3 for the map of EHT, uniquely designed for the imaging of supermassive black holes by using very long baseline interferometry (VLBI) [22]. The primary EHT targets are the supermassive black hole candidates M87* and Sgr A*, the latter is the compact radio source at the Galactic center of Sagittarius A. These are the most observable nearby candidates from the Earth, both have a similar apparent angular size roughtly around $40 \sim 50$ μas. This size is as small as the apparent size of grapefruit on the Moon, thus we need the telescope to have a very high resolution in order to resolve the black holes at such small scale. The angular resolution of a telescope is determined by λ/D with λ the observing wavelength and D the telescope's aperture. The first EHT image was observed at a wavelength of 1.3 mm (230 GHz) together with the Earth-sized aperture, so the observing angular resolution was 25 μas which was sufficient for the expected precision [21].

An important feature of the first image of M87* (Fig. 2) is a bright asymmetric ring surrounding a central dark region [21]. The dark region is known as the "*black hole shadow*" and embedded within the bright ring lies an interesting "*photon ring*" [32]. The image matches perfectly well with the expectations for the shadow of a rotating black hole as predicted by GR. However, fine structures of this bright ring are not resolved yet [25]. Since black hole models in alternative gravitational theories are still not ruled out, these fine structures are particularly important for screening different models, thus for testing gravity theories. Therefore, observations with higher resolution are in need, which can be attained by expanding the VLBI array and by going to shorter observing wavelength. There are ongoing plan for adding millimeter telescopes in Africa and a further plan for space-based VLBI [21, 33].

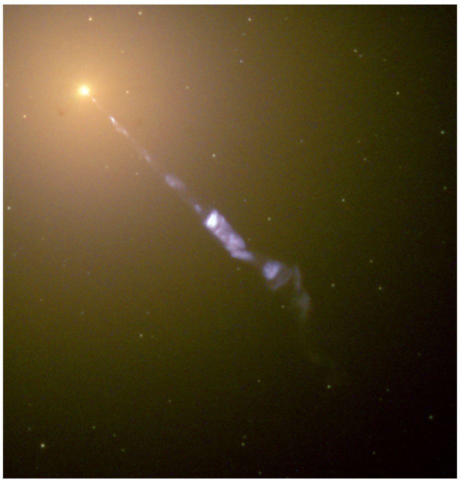

Figure 1.: Galaxy M87 with jet ejected from its core. Credit to here.

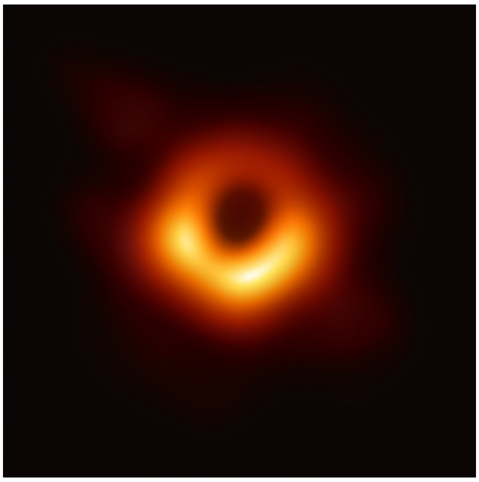

Figure 2.: EHT image of the supermassive balck hole candidate M87*. Credit to here.

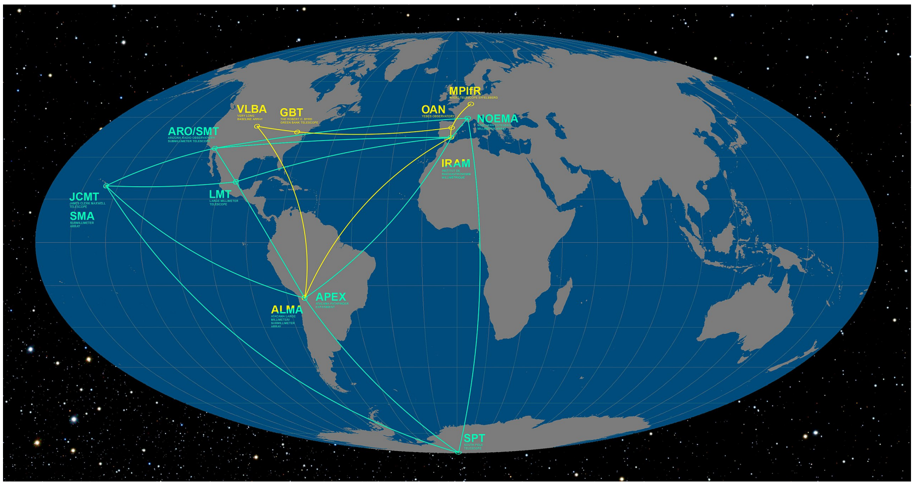

Figure 3.: Map of the Event Horizon Telescope array. Credit to here.

1.2 BRIEF HISTORY OF BLACK HOLE IMAGING

Today, we celebrate the beautiful first image of the supermassive black hole M87*. However, it seemed just impossible to image a black hole in earlier years. Yet nothing could stop scientists to ask what a black hole would look like. They started by calculating the shadow casted by a black hole and drawing plots which would depict a first glimpse of a black hole. Then, with the advanced computing power, they performed more and more sophisticated simulations to produce better and better virtual reality pictures of a black hole. Meanwhile, scientists also explored the possibility of imaging a black hole by telescopes in practice and made it eventually become true. It takes a long time from idea to reality. Here I briefly review several important theoretical steps along this fantastic journey[3].

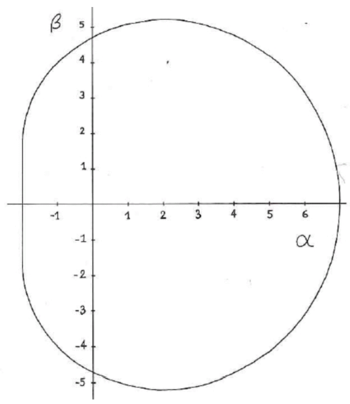

Figure 4.: Apparent boundary (critical curve) of a backlit extremal Kerr black hole as seen by a distant observer in the equatorial plane. Credit to [37].

In 1965, Synge studied the escape cone of photons from a Schwarzschild black hole and obtained the angular radius of the shadow casted by that black hole [38]. In 1972, Bardeen calculated the apparent boundary of an extremal Kerr black hole and drew his famous D-shaped shadow (see Fig. 4) [37]. Here, the so-called shadow is the optical appearance of a *bare black hole* illuminated by distant

3 See reviews about black hole imaging from [34, 33, 35, 36, 29].

sources. The boundary of a black hole shadow corresponds to the threshold between captured and escaping photons, i.e., unstable spherical photon orbits. In the literature, this boundary is often referred to as "rim", "silhouette" or simply as "shadow". To make it definite, Gralla et al [39] gave the boundary a mathematical name as *critical curve*, which is a basic and important feature of a black hole shadow and depends on the spacetime geometry of its underlying gravity theory. Therefore, critical curves for a large number of black holes in various spacetimes, either within GR or within theories beyond GR, have been exhaustively studied. Examples include Kerr-Newman black hole [40], Kerr-Taub-NUT black hole [41], Kerr-Newman-NUT black hole [42], Kerr-Sen black hole [43], Kerr-MOG black hole [44] and Einstein dilaton Gauss-Bonet black hole [45].

In 1973, Cunninggham and Bardeen [46] calculated the optical appearance of a *point source* (star) orbiting on an equatorial and circular orbit around an extremal Kerr black hole, taking into account not only the gravitational focus effect (position of the star's image) but also the gravitational redshift effect and Doppler effect (amplification of the star's luminosity). The main result was illustrated by "hat-shaped" orbits (see Fig. 5) for the apparent positions of the brightest several images. These hat-

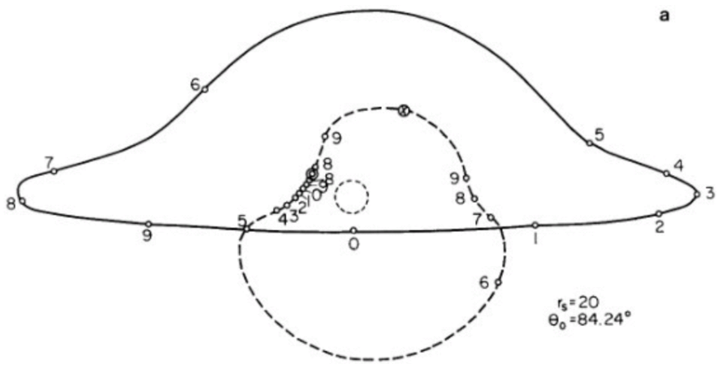

Figure 5.: Time-dependent images of a star orbiting around an extremal Kerr black hole as seen by a distant observer at an inclination $\theta_o = 84.24°$. Credit to [46].

shaped orbits had already shown the basic structures which were seen later in simulated black hole shadows. Moreover, they also plot figures for the behavior of the images' brightness as functions of observer's time. Recently, these results were reproduced in Ref. [47], described by colorful plots and video animations. A point source can also be a "hot spot" (localized emissivity enhancement) in an accretion disk, in which case the circular orbits could be much closer to the event horizon regardless of the Roche limit[4]. In 2017, Gralla et al analytically computed the optical appearance of a hot spot orbiting near the ISCO of a high spin Kerr black hole and found a very striking signature [5]. Besides, the images of a plunging source inside the ISCO have been studied by Dokuchaev and Nazarova [48, 49].

Most remarkably, in 1979, Luminet studied the appearance of a Schwarzschild black hole embedded in a geometrically thin, optically thick *accretion disk*, which is much closer to reality, and produced the first-ever simulated[5] image (Fig. 6) of a black hole [50]. The main feature of this image is a strong asymmetric bright ring surrounding a central dark region, which is exactly what the first EHT's image looks like [21]. The bright ring is actually a lensed image of the accretion disk, thus it depends crucially on the assumption of the disk model. The strong asymmetry of the bright ring is due to the Doppler effect while the boundary of the central dark region is the lensed position of the inner edge of the accretion disk. In 1988, an improved colorful image was produced by Fukue and Yokohama in which the changes of apparent frequencies in the accretion disk were taken into account [51]. In 1993, Viergutz generalized the study to that of the apparent shape of an accretion disk around a rotating Kerr black hole and produced colored contours [52, 53]. The standard assumption in these studies were that the disk ended at the ISCO without photons radiated from the plunging region inside ISCO. In order to understand the image of a disk better, recently, Gralla et al analytically calculated the shadows and rings with simple disk models which are allowed to extend all the way to the event horizon [39].

In 2000, Falcke et al studied the possibility of imaging the shadow of Sgr A* in practice with VLBI experiments at sub-millimeter wavelengths [54]. This was an important turning point in the journey

4 Roche limit is the critical orbital distance for a celestial body to hold together and avoid tidally disrupting.

5 Actually, Luminet drew it by hand using numerical data generated from the computer.

Figure 6.: First simulated image of a spherical black hole with thin accretion disk terminating at the innermost stable circular orbit (ISCO), as seen by a distant observer at 10° above the disk's plane. Credit to [50].

of black hole imaging from idea to reality. The authors developed a numerical ray-tracing code to simulate the expected images (see Fig. 7) of Sgr A* for various choices of physical parameters. They found that, when observing at a wavelength of $\sim$1.3 mm, the resolution of an Earth-sized VLBI arrays becomes comparable to the angular size of Sgr A*. Therefore, it is just possible to image the event horizon of a black hole in reality.

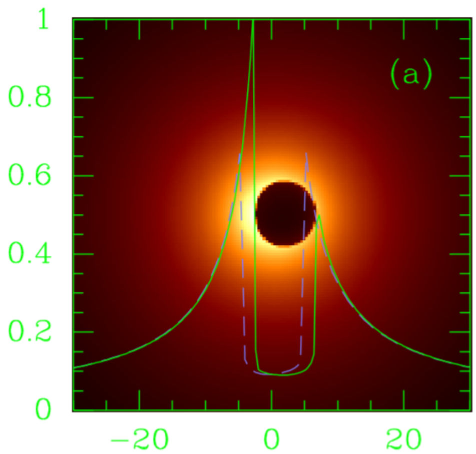

Figure 7.: Simulated image of the black hole Sgr A* surrounded by an optically thin emission region, as seen from $\theta_o = 45^\circ$. Credit to [54].

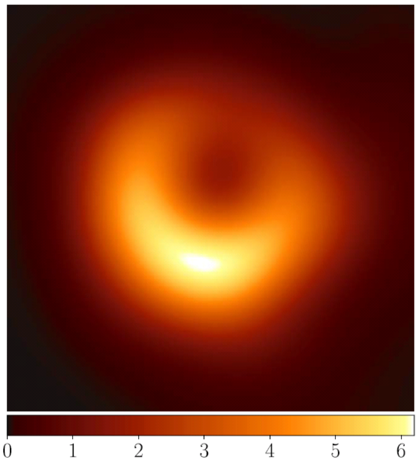

Figure 8.: Blurred GRMHD image of M87*. Credit to [25].

The current state-of-art simulations are done using numerical general relativistic magnetohydrodynamic (GRMHD) models which are much more sophisticated then before. Importantly, the observed image of M87* (Fig. 2) by EHT matches very well with the GRMHD simulated image (Fig. 8) [25].

1.3 OBSERVATIONAL SIGNALS OF HIGH-SPIN BLACK HOLES

The optical appearance of a black hole is a consequence of the propagation of photons in a finite region (where unstable spherical photon orbits exist) outside the event horizon. However, as we wish to explore the event horizon of black holes, we are particularly interested in photons which are extremely close to the event horizon. Due to the emergence of scaling symmetries, photons in the near-horizon region are not only possible to be observed but may also produce striking signals for near-extremal rotating (high-spin) black holes—rotating at near-maximally allowed theoretical limits [5]. A remarkable example of such signals is the broadening of the iron Kα line which is the strongest feature of an X-ray reflection spectrum [15, 55].

In 1999, Bardeen and Horowitz studied the near-horizon limit of an extremal Kerr black hole and found enhanced conformal symmetries arising in the near-horizon region [56]. Similar features of symmetries are also appearing in many critical low-energy condensed matter systems [57] and in large-cosmological-redshift inflation [58, 59, 60, 61]. It was shown that the scaling symmetries not only reduce the complexity of dynamics but also supply powerful computational techniques which are often used in conformal field theory. Therefore, one could analytically calculate potential observables with simplified models and find universal signals as a result of the symmetries. It is suggested from astronomical observations that a large number of astrophysical black holes, especially supermassive ones in AGN, have high spins [62]. For example, the stellar-mass black holes Cygnus X-1 [63] and GRS 1915+105 [64] both have spins $\lesssim 2\%$ below extremality; and the supermassive black hole MCG-6-30-15 [65] has a spin $\lesssim 1\%$ below extremality. Therefore, the computational tools used in conformal field theory might be applied to the study of astrophysical black holes with high-spins. Indeed, there has been plenty of studies regarding gravitational wave signals from extreme-mass-ratio-inspirals (EMRIs) or plunging sources [66, 67, 68, 69, 70, 71], relativistic jets from force-free magnetospheres [72, 73, 74, 75] and electromagnetic emission from the near-horizon region [4, 5, 55].

We will study the latter case and focus on the emission from a near-ISCO hot spot whose observational signals would (in principle) be possible to be observed by the EHT. In reality, it would require an advanced EHT with higher resolution and an appropriate EHT target which rotates rapidly and has sufficiently long-lived hot spots in the near-horizon region. However, since the astrophysical black holes are so common in the universe, it is reasonable to hope that a future EHT might eventually observe such a nice target. If observed, the expected signals would be at a new level of precision and might reveal new features of the event horizon of a black hole [5].

So far, the study of observational features of astrophysical black holes is still at its infancy. Thus, most of the studies are based on the standard Kerr black hole as predicted in GR. Nevertheless, it would be interesting to study the observational signals of black holes arising from alternative theories of gravity [76]. In particular, with the higher level of precision, these signals might be used to screen and distinguish different gravity theories.

1.4 THESIS OUTLINE

The remaining part of the thesis is organized as follows:

Chapter 2 presents review of basic knowledge on gravity and black holes, as well as formalisms for describing the black hole shadows. In particular, we introduce in detail the analytical computations of the observational quantities of an isotropically emitting point source orbiting near the ISCO of a high-spin Kerr black hole in a vacuum background, which is the central topic of this thesis. The main references for this review are [37, 46, 5].

Chapters 3, 4 and 5 consists of original works of the author and collaborators.

In chapter 3, we study the influence of a surrounding plasma on the observational signature of a high-spin Kerr black hole, in order to approach a more reliable result for astrophysical observations. To this end, we consider the refractive and dispersive effects of the plasma on light rays and ignore the gravitational effects of plasma particles as well as the absorption or scattering processes of photons. With two specific plasma models, we obtain analytical formulae for the black hole shadow and for the observational quantities of an orbiting hot spot seen by an observer located far away from the black hole. We find that the plasma has a frequency-dependent dispersive effect on the size and shape of the black hole shadow and on the image position and redshift of the hot spot. This chapter is based on the work [2].

In chapter 4, we study the observational signature of a near-extremal Kerr-MOG (KM) black hole with a near-ISCO emitter in the scale-tensor-vector modified gravity (MOG). The KM black hole metric has a mathematically similar form as the Kerr-Newman (KN) metric but has a neutral gravitational charge, rather than an electric charge. For several different values of the modified parameter of the MOG theory, we calculate the apparent size of the black hole shadow, as well as the observational quantities of the hot spot. The size of the shadow decreases when the modified parameter is increased. We find qualitatively similar signals of the hot spot image but the quantitative corrections could be considerable. This chapter is based on the work [1].

In chapter 5, we analytically study the optical appearance of an isotropic emitter orbiting near the horizon of a near-extremely rotating Kerr-Sen (KS) black hole which is an electrically charged black hole arising in heterotic string theory. We study the influence of the Sen charge on the observational quantities, including the image position, flux and redshift factor. Moreover, we compare the results with those for a near-extremal KN black hole, which is the charged rotating black hole in GR. We find quantitative corrections to the signatures of these charged black holes (both KS and KN) compared to that of a neutral Kerr black hole. We also make a comparison between the KN and KM cases. This chapter is based on the work [3].

Chapter 6 gives a short summary and final remarks.

Appendices present some computational details for the integrals and for the image flux that appear in our analysis.

2

BACKGROUND

We review the necessary background materials and introduce the main topic of this thesis. In Sec. 2.1, we introduce gravity theories—GR and its alternatives, followed by an introduction to rotating black holes in GR in Sec. 2.2, paying special attention on the extremal limit. In Sec. 2.3, we introduce the motion of particles and photons in Kerr exterior. In Secs. 2.3.2, 2.4 and 2.5, we describe respectively the *rays*, *observers* and *sources*, central to the subject of black hole imaging. In Sec. 2.6, we introduce the main topic—the images of an emitter orbiting near-ISCO of a high-spin black hole. We review the pioneering study [5] for the Kerr black hole with vacuum surroundings, which will be generalized in the following chapters.

2.1 GRAVITY, GENERAL RELATIVITY AND ALTERNATIVES

The secret that governs the motion of stars was long hidden in the night until a fantastic falling apple enlightened Newton. Surprisingly, it turns out that it is the same law that rules both the stars and the apple—the *Newton's law of universal gravitation*. The field equation of Newtonian gravity is given by[1]

$$\nabla^2\phi = 4\pi\rho, \tag{1}$$

1 Unless otherwise stated, we work in units $c = G_N = \hbar = 1$ throughout this thesis.

where ϕ is the gravitational potential and ρ is the matter density. As noted above, Newtonian gravity has an extremely good explanatory power not only for practical situations of daily life but also for astronomical scenarios that happens in the universe. However, it fails at predicting accurately the perihelion pression of Mercury's orbit, the deflection of light by the Sun, and the gravitational redshift of light.

These discrepancies between Newtonian predictions and astronomical observations were resolved by *Einstein's general theory of relativity* and are known as the three classical tests of GR. That was a great success and made GR soon become the most prominent theory of gravitation. The Einstein's field equation is given by

$$G_{\mu\nu} = 8\pi T_{\mu\nu}, \tag{2}$$

where $G_{\mu\nu} = R_{\mu\nu} - \frac{1}{2}Rg_{\mu\nu}$ is the Einstein tensor for the spacetime metric $g_{\mu\nu}$, which encodes the geometry of the spacetime; $T_{\mu\nu}$ is the energy-momentum tensor for the matter field which curves the spacetime. GR provides a completely new description of gravity as a geometric property of spacetime and has often been appreciated for its extraordinary beauty. However, GR was born as a defective theory [76] as pointed out by Einstein himself due to the appearance of spacetime singularities, where spacetime becomes ill-defined and any known physics breaks down. Moreover, GR is a classical theory and fails at the smallest scales where a quantum description is needed. It is a long-standing question to reconcile quantum theory with GR. On the other hand, even though GR is well-tested on the scales of solar system, it fails at predicting some astronomical observations on the scales of galaxies or cosmology, such as galaxies rotation curves, mass profiles of clusters and some cosmological data.

Therefore, even though GR is still the most successful theory of gravity, there are indications suggesting that alternatives are needed to accommodate GR at the quantum scales and at the cosmological scales. A gravity theory that works well at all scales would be essential for the understanding of modern physics. Thus, testing gravity in different regimes is an important subject. As unique objects predicted in many gravity theories, black holes can play special role in testing them, especially in testing the strong field regime which is more urgent than the weak-field tests. We will consider two of the alternative theories of gravity to GR, one is motivated from astronomical and cosmological interests—the *scalar-tensor-vector gravity* (STVG) or referred as *modified gravity* (MOG) [77], and the other from fundamental and theoretical interests—the *low energy heterotic string theory* [78].

Within the GR framework, dark matter is proposed to accommodate the aforementioned astronomical phenomenons on galactic or cosmological scales. However, even though it is widely accepted, the nature of dark matter is still elusive and has not been directly detected so far. The best-known alternative theory to dark matter is the Modified Newtonian Dynamics (MOND) proposed by Milgrom in 1983 [79]. The idea of MOND is to introduce a law of effective gravitational force which reduces to Newtonian dynamics at high acceleration but leads to deviations of Newtonian results at low acceleration. However, MOND is a non-relativistic theory. From the same motivation but independently, in 2005 Moffat [77] proposed a relativistic theory that—instead of modifying Newtonian dynamics—modifies GR such that the force is stronger than Newtonian far from the source but counteracted by a repulsive fifth forth at shorter distance to the source. Moffat's MOG theory is a covariant theory constructed by adding a massive vector field to the standard Einstein-Hilbert action and allowing the mass of the vector field, the coupling parameter of the vector field and the Newtonian constant to vary as scalar fields. The vector field leads to a gravitational repulsive force at a finite range. In Chapter 4, we will introduce some relevant details about the MOG theory and discuss the observational signature of a rapidly rotating black hole in MOG theory.

String theory is one of the most promising and attractive candidates for a theory of quantum gravity. Roughly speaking, the idea of string theory is simply to generalize the quantum field theory of point-like objects to a quantum theory of one-dimensional string-like objects. Interestingly, general relativity naturally emerges in this theory as its classical low energy limit. In Chapter 5, we will introduce specifically the low energy heterotic string theory and discuss the observational signature of a rapidly rotating black hole in this theory.

2.2 PROPERTIES OF BLACK HOLES

Soon after Einstein published his theory of GR, the first exact, static and spherically symmetric solution to the vacuum field equations of GR was found by Schwarzschild in 1916, which describes a non-rotating black hole, known as the *Schwarzschild black hole*. The stationary and axially symmetric solution to these vacuum field equations of GR was only found until 1963 by Kerr, which describes a rotating black hole, known as the *Kerr black hole*. Later in 1965, Newman discovered the solution to the electrovacuum field equations of GR, which generalizes the Kerr metric and describes a charged rotating black hole, known as the *Kerr-Newman black hole*. Similar solutions were also found in many alternative theories of gravity, including the MOG theory and heterotic string theory.

We will consider real astrophysical black holes in the universe which are thought to be rotating ones and can be described by Kerr-like metrics. In addition to the Kerr and Kerr-Newman (KN) metrics that arise from GR, we will also study the Kerr-MOG (KM) metric [80] arising in the MOG theory and the Kerr-Sen (KS) metric [81] present in low energy heterotic string theory. The basic properties of optical observations of black holes mostly follow from the properties of spacetime metrics, instead of the deeper level of the gravity theories. Next, after giving a brief sketch of how the Kerr(-Newman) metric is obtained from GR, we will take this metric as an example to introduce properties of a black hole.

The starting point is the action for an electrovacuum in GR, given by

$$S = \int d^4x \sqrt{-g}\left(\mathcal{L}_{\mathrm{EH}} + \mathcal{L}_{\mathrm{M}}\right), \qquad \mathcal{L}_{\mathrm{EH}} = \frac{1}{16\pi} R, \qquad \mathcal{L}_{\mathrm{M}} = -\frac{1}{4} F_{\mu\nu} F^{\mu\nu}, \tag{3}$$

where $\mathcal{L}_{\rm EH}$ is the Einstein-Hilbert Lagrangian for the gravitational field $g_{\mu\nu}$, and $\mathcal{L}_{\rm M}$ is matter Lagrangian for the electromagnetism field A_μ with $F_{\mu\nu} = \nabla_\nu A_\mu - \nabla_\mu A_\nu$ being the electromagnetism field strength tensor. The Einstein-Maxwell field equations are obtained by using the least action principle, as

$$G_{\mu\nu} = 8\pi T_{\mu\nu}, \qquad T_{\mu\nu} = \frac{1}{4\pi}\left(F_{\mu\sigma}F_\nu^{\ \sigma} - \frac{1}{4}g_{\mu\nu}F^{\sigma\delta}F_{\sigma\delta}\right), \tag{4a}$$

$$\nabla_\nu F^{\mu\nu} = 0, \qquad \nabla_\lambda F_{\mu\nu} + \nabla_\nu F_{\lambda\mu} + \nabla_\mu F_{\nu\lambda} = 0 \tag{4b}$$

where $G_{\mu\nu}$ is the Einstein tensor and $T_{\mu\nu}$ is the electromagnetic energy-momentum tensor.

The KN metric is a stationary and axisymmetric solution to these field equations and is described in Boyer-Lindquist coordinates $\{t, r, \theta, \phi\}$ by the line element

$$\begin{aligned} ds^2 &= g_{\mu\nu}dx^\mu dx^\nu \\ &= -\left(1 - \frac{2Mr}{\Sigma}\right)dt^2 + \frac{\Sigma}{\Delta}dr^2 + \Sigma d\theta^2 + \left(r^2 + a^2 + \frac{2Ma^2r}{\Sigma}\sin^2\theta\right)\sin^2\theta d\phi^2 \\ &\quad -\frac{4Mar}{\Sigma}\sin^2\theta dt d\phi, \end{aligned} \tag{5}$$

where

$$\Sigma(r,\theta) = r^2 + a^2\cos^2\theta, \qquad \Delta(r) = r^2 - 2Mr + a^2 + Q^2. \tag{6}$$

Here, M and Q are the mass and electric charge of the black hole, respectively, and $a = J/M$ is the spin (angular momentum per unit mass) of the black hole with J being its angular momentum. The Boyer-Lindquist coordinates were chosen such that they appear to be spherical-like and adapted to the Killing symmetries of the spacetime: t is the time coordinate corresponding to stationary symmetry encoded by the Killing vector ∂_t, and ϕ is the azimuthal coordinate corresponding to axisymmetry encoded by the Killing vector ∂_ϕ.

Even though there is still no rigorous mathematical proof, the conjectured "*black hole no hair theorem*" is widely appreciated [2], which states that black holes can be described by just three parameters:

2 There are interesting works examining the no hair theorem by studying the shadows of hairy black holes. See for example [28, 82].

mass M, angular momentum J and charge Q, as described above by the KN metric. Due to the fact that the interstellar medium has a high conductivity, astrophysical black holes are less likely to be charged ones for long, so the uncharged cases, $Q = 0$, are more relevant in reality. If the black hole is uncharged, then the KN metric reduces to the Kerr metric. The Kerr metric will further reduce to the non-rotating Schwarzschild metric for $a = 0$.

For any stationary, axisymmetric and asymptotically flat spacetime, it is useful to express its metric in the following standard form in Boyer-Lindquist coordinates [83],

$$ds^2 = -e^{2\nu}dt^2 + e^{2\psi}(d\phi - \Omega_{bh}dt)^2 + e^{2\mu_1}dr^2 + e^{2\mu_2}d\theta^2, \tag{7}$$

where ν, ψ, μ_1, μ_2 and Ω_{bh} are functions of r and θ. For Kerr metric, we have

$$e^{2\nu} = \frac{\Sigma\Delta}{\Xi}, \qquad e^{2\psi} = \frac{\Xi\sin^2\theta}{\Sigma}, \qquad e^{2\mu_1} = \frac{\Sigma}{\Delta}, \qquad e^{2\mu_2} = \Sigma, \qquad \Omega_{bh} = \frac{2Mar}{\Xi}, \tag{8}$$

where

$$\Delta = r^2 - 2Mr + a^2, \qquad \Sigma = r^2 + a^2\cos^2\theta, \qquad \Xi = (r^2 + a^2)^2 - a^2\Delta\sin^2\theta. \tag{9}$$

The metric becomes singular at the roots of either $\Sigma = 0$ or $\Delta = 0$. We then briefly discuss the corresponding singularities and restrict ourself to the spacetimes of black hole type.

The equation $\Sigma = 0$ is solved on a ring of $r = 0$ and $\theta = \frac{\pi}{2}$. It turns out that the singularity on this ring is a true singularity since the spacetime curvature $R^{\mu\nu\rho\sigma}R_{\mu\nu\rho\sigma}$ diverges on it, which is thus referred to as the *ring singularity*. The equation $\Delta = 0$ is solved at a pair of *event horizons*

$$r_\pm = M \pm \sqrt{M^2 - a^2}, \tag{10}$$

which only correspond to coordinate singularities. For $M^2 < a^2$, the equation $\Delta = 0$ does not have real roots, the metric then describes a *naked singularity*. A naked singularity is assumed to be prevented in an observable spacetime according to the *Cosmic Censorship Conjecture*. For $M^2 = a^2$, the metric describes an extremal black hole and the horizons coincide at $r = M$. For $M^2 > a^2$, the metric describes a non-extremal black hole spacetime with two distinct event horizons at $r_\pm$, the inner one is a Cauchy horizon, the outer one is the event horizon ("one-way membrane") of a black hole in the usual sense.

As our concern is a black hole, we put the following constraint on the parameters of Kerr metric: $0 \leq a \leq M$. Again, M and a are the mass and spin of the black hole, r_+ given in Eq. (10) is its event horizon which ranges from $2M$ to M. Moreover, Ω_{bh} in Eq. (8) is the frame-dragging angular velocity of the black hole determined completely by the spacetime geometry. The domain outside the event horizon, $r > r_+$, is referred to as the exterior region while the domain inside, $r < r_+$, is the black hole region; the event horizon of the black hole, $r = r_+$, is a null surface. Nothing in the black hole region can escape from this surface, even light. Therefore, an observer in the exterior of black hole can never measure information beyond the event horizon. To study the optical appearance of a black hole, we only need to systematically study the photon propagations in the exterior region of the black hole.

Since the Kerr metric is stationary, a static observer does not exist everywhere in the Kerr exterior. In a region near the event horizon, all four basis vectors ∂_t, ∂_r, ∂_θ and ∂_ϕ are spacelike, no observer can remain "at rest" and move along the Boyer-Lindquist t coordinate. That is, we have in particular $g_{tt} > 0$ in this region and an observer is "forced to rotate" due to the "frame-dragging" effects of the black hole's rotation. The static limit is obtained for $g_{tt} = 0$, i.e., $\Sigma - 2Mr = 0$, solving which gives the ergosurfaces

$$r_{0\pm} = M \pm \sqrt{M^2 - a^2 \cos^2\theta}. \tag{11}$$

The region $r_+ < r < r_{0+}$ is called the ergoregion. A static observer exists only outside the outer ergosurface r_{0+}.

2.2.1 *Near-extremal black holes*

The Kerr metric has further interesting properties in the (near-)extremal limit. As we discussed before, the extremal limit is obtained for

$$J = M^2, \qquad a = M, \tag{12}$$

which corresponds to $\Delta = 0$. Then from $g_{rr} = \Sigma/\Delta$ we see that the proper spatial distance from a constant t surface to the event horizon is infinite, that is, there is a long throat near the horizon of an extremal Kerr black hole [56]. When zooming into this throat, there exists three distinct scaling limits [66]. For near-extremal Kerr, we introduce

$$\kappa = \sqrt{1 - (\frac{a}{M})^2} \ll 1. \tag{13}$$

We also introduce the dimensionless Bardeen-Horowitz coordinates [56] to describe the different extremal limits,

$$\tilde{T} = \frac{\kappa^p t}{2M}, \qquad \tilde{\Phi} = \phi - \frac{t}{2M}, \qquad \tilde{R} = \frac{r - M}{\kappa^p M}, \tag{14}$$

where $0 \leq p \leq 1$. Letting $\kappa \to 0$ at fixed Bardeen-Horowitz coordinates, different choices of p correspond to different decoupled spacetime regions. We also introduce $R = \kappa^p \tilde{R}$ for convenience. For $p = 0$, this describes the usual limit of the extremal Kerr exterior in which $R \sim 1$. For $0 < p < 1$, this describes the *near-horizon extremal Kerr* (NHEK) region since $\kappa \ll \kappa^p \ll 1$ and $R \sim \kappa^p$. For $p = 1$, this describes the even deeper *near-horizon near-extremal Kerr* (near-NHEK) region since $\kappa = \kappa^p \ll 1$ and $R \sim \kappa$. It has been shown that near-NHEK and NHEK are locally diffeomorphic, and the near-NHEK corresponds a smaller patch of the NHEK patch. Explicitly, the NHEK geometry takes the form [56]

$$ds^2 = 2M^2\Gamma(\theta)\Big[- \tilde{R}^2 d\tilde{T}^2 + \frac{d\tilde{R}^2}{\tilde{R}} + d\theta^2 + \Lambda(\theta)^2 (d\tilde{\Phi} + \tilde{R} d\tilde{T})^2 \Big], \tag{15}$$

where

$$\Gamma(\theta) = \frac{1+\cos^2\theta}{2}, \qquad \Lambda(\theta) = \frac{2\sin\theta}{1+\cos^2\theta}. \tag{16}$$

In addition to the $\partial_{\tilde{T}}$ and $\partial_{\tilde{\Phi}}$ symmetries, the NHEK metric acquires an enhanced scaling symmetry such that the metric is invariant under the transformation

$$(\tilde{T}, \tilde{R}) \to (\frac{\tilde{T}}{c}, c\tilde{R}) \tag{17}$$

for any constant c.

The usual extremal Kerr metric resolves physics in the far region (away from the event horizon), while the (near-)NHEK metric resolves physics in the near-horizon region. When studying physical processes that extend from the near-horizon region all the way to the far region, we need both of the limiting metrics and they are on equal footing since each of these breaks in another region [66][84]. The far region is asymptotically flat, so that computations involving spacetime geometry are much simplified. In the (near-)NHEK region, the enhanced symmetries also make it possible to perform analytical computations. Combining these by using the method of matched asymptotic expansions (MAE) between the two distinct regions, one can analytically compute some problems which can only be numerically accessed in the more general case [66].

2.3 PARTICLE MOTION

In order to get some insights into the underlining spacetime features and to analytically calculate observables of black holes, we study of equations of motion for arbitrary particles, both massive and massless, in the exterior region of black holes.

We consider a spacetime with line element $ds^2 = g_{\mu\nu}dx^\mu dx^\nu$. The equations of motion for a free particle moving along a trajectory $x^\mu(s)$ in this spacetime are the geodesic equations, which in general form are given by

$$\partial_s^2 x^\mu + \Gamma^\mu_{\alpha\beta}\partial_s x^\alpha \partial_s x^\beta = 0, \tag{18}$$

where ∂_s denotes derivative with respect to the affine parameter s, and $\Gamma^\mu_{\alpha\beta}$ are the Christoffel symbols. These are a set of coupled second order non-linear differential equations, which in general can only be computed numerically. For analytical study of the geodesics, we need to consider certain symmetries of the spacetime which generate corresponding integrals of motion and allow us to reduce the geodesic equations to first order by using the Hamilton-Jacobi (H-J) method.

We review the derivation for the first order equations in the Kerr spacetime [85], which can be easily generalized to Kerr-like spacetimes with the same symmetries. The four-momentum of a particle is $p^\mu = \partial_s x^\mu$, where, for a timelike particle, the affine parameter s is related to the particle's proper time τ by $s = \tau/\mu$, with μ the mass of the particle. The first constant of motion is the Hamiltonian

$$H = \frac{1}{2}g^{\mu\nu}p_\mu p_\nu = -\frac{\mu^2}{2}. \tag{19}$$

Using the two Killing vectors of the Kerr metric, we can then obtain two constants of motion for a free particle: the energy E and the angular momentum parallel to the axis of symmetry L, as measured by a static observer at infinity,

$$E = -g_{\mu\nu}p^\mu(\partial_t)^\nu = -p_t, \qquad L = g_{\mu\nu}p^\mu(\partial_\phi)^\nu = p_\phi. \tag{20}$$

However, this is not enough to make the system completely integrable. Fortunately, in the Kerr spacetime, there is also a hidden symmetry corresponding an additional constant. This new constant was found by Cater by separating the variables in the H-J equation [85]

$$g^{\mu\nu}\partial_\mu S \partial_\nu S = -\mu^2, \tag{21}$$

where we have assumed there is a separable solution for the Hamilton principle function

$$S(t,\, r,\, \theta,\, \phi) = -\frac{1}{2}\mu^2 s - Et - L\phi + S_r(r) + S_\theta(\theta). \tag{22}$$

Then we have

$$e^{-2\nu}(-E + \Omega_{bh} L)^2 + e^{-2\mu_1} p_r^2 + e^{-2\mu_2} p_\theta^2 + e^{-2\psi} L^2 = -\mu^2, \tag{23}$$

where ν, ψ, μ_1, μ_2 and Ω_{bh} are functions of r and θ, given in Eq. (8). Using $p_\mu = \partial_\mu S$ one can obtain the separation constant for the r and the θ motion,

$$\begin{aligned} \mathcal{K} &= p_\theta^2 + \left(aE\sin\theta - \frac{L}{\sin\theta}\right)^2 + a^2\mu^2\cos^2\theta \\ &= -\left[\Delta p_r^2 - \frac{1}{\Delta}\left((r^2+a^2)E - aL\right)^2 + \mu^2 r^2\right]. \end{aligned} \tag{24}$$

Here, the expression in the first line is only a function of θ while the expression in the second line is only a function of r. The separation constant is related to the Carter constant $\mathcal{Q}$ by

$$\mathcal{Q} = \mathcal{K} - (L - aE)^2. \tag{25}$$

By solving the H-J equation, one can obtain the expressions for the first order differential equations of motion for particles

$$\Sigma p^r = \pm\sqrt{\tilde{\mathcal{R}}(r)}, \tag{26a}$$

$$\Sigma p^\theta = \pm\sqrt{\tilde{\Theta}(\theta)}, \tag{26b}$$

$$\Sigma p^\phi = -\left[aE - \frac{L}{\sin^2\theta}\right] + \frac{a}{\Delta}\left[E(r^2+a^2) - La\right], \tag{26c}$$

$$\Sigma p^t = -a\left(aE\sin^2\theta - L\right) + \frac{a^2+r^2}{\Delta}\left[E(r^2+a^2) - La)\right], \tag{26d}$$

where

$$\tilde{\mathcal{R}}(r) = \left[E(r^2+a^2) - La\right]^2 - \Delta\left[\mathcal{Q} + (L-aE)^2 + \mu^2 r^2\right], \tag{27}$$

$$\tilde{\Theta}(\theta) = \mathcal{Q} - \cos^2\theta\left[a^2(\mu^2 - E^2) + L^2\csc^2\theta\right]. \tag{28}$$

Here, $\tilde{\mathcal{R}}$ and $\tilde{\Theta}$ are respectively the radial and angular "effective potentials". The vanishing of either of these corresponds to a turning point along a trajectory.

Trajectories of particles are thus labeled by their conserved quantities of motion: μ, E, L and $\mathcal{Q}$. Without loss of generality, we may take $\mu = 1$ for massive particles while take $\mu = 0$ for massless particles (photons).

Note that the H-J method can also be used to study light propagations in a certain distribution of plasma on Kerr spacetime, in which case the equations of motion for photons are no longer geodesics. In chapter 3, we will study the influence of a plasma on the photon motion and on the optical appearance of a black hole.

2.3.1 *Massive particle*

The motion of massive particles in the exterior of a black hole is of relevance for emitting sources. We analysis several orbits for test particles in the Kerr exterior and introduce the corresponding regions around the black hole. For mathematical simplicity without loss of physical importance, we consider only test particles lying in the equatorial plane and orbiting around the black hole on circular orbits [83].

We have $\theta_s = \frac{\pi}{2}$ for orbits in the equatorial plane, where the subscript s denotes the source. For a circular orbit at radius $r = r_s$, we have $dr_s/ds = 0$ and $d^2r_s/ds^2 = 0$. Then from Eq. (27) we have $\tilde{\mathcal{R}}(r_s) = 0$ and $\tilde{\mathcal{R}}'(r_s) = 0$, where prime represents the derivative to r_s. Solving these equations simultaneously for E and L gives

$$\frac{E}{\mu} = \frac{r_s^{3/2} - 2Mr_s^{1/2} \pm aM^{1/2}}{r_s^{3/4}P^{1/2}}, \qquad \frac{L}{\mu} = \frac{\pm M^{1/2}(r_s^2 \mp 2aM^{1/2}r_s^{1/2} + a^2)}{r_s^{3/4}P^{1/2}}, \tag{29}$$

where $P = r_s^{3/2} - 3Mr_s^{1/2} \pm 2aM^{1/2}$ and, here and hereafter, the upper/lower sign refers to direct/retrograde orbits. The coordinate angular momentum of the orbit can be obtained with the help of Eqs. (26),

$$\Omega_s = \frac{d\phi}{dt} = \frac{\pm M^{1/2}}{r_s^{3/2} \pm aM^{1/2}}. \tag{30}$$

The existence of circular orbits requires that the denominator of Eqs. (29) is real, i.e., $P \geq 0$. The critical case of equality corresponding to the innermost boundary of the circular orbits for particles with $E/\mu \to \infty$. However, since a physical particle can not have infinity energy the critical orbits corresponds to nothing but a photon orbit (ph), which is obtained for $P = 0$,

$$r_{\rm ph} = 2M\Big[1 + \cos\Big(\frac{2}{3}\arccos \mp \frac{a}{M}\Big)\Big]. \tag{31}$$

For orbits in the region $r_s > r_{\rm ph}$, we are interested in those bound ones with $E/\mu < 1$ since otherwise the orbits can not stably exist. The marginally bound circular orbit (mb) has $E/\mu = 1$, we refer to such orbit as the Innermost Bound Circular Orbit (IBCO),

$$r_{\rm IBCO} = r_{\rm mb} = 2M \mp a + 2M^{1/2}(M \mp a)^{1/2}. \tag{32}$$

Note that not all bound circular orbits are stable. For such orbits to be stable we require that $\tilde{\mathcal{R}}''(r_s) \leq 0$ with equality corresponding to the marginally stable circular orbit (ms), also referred to as the Innermost Stable Circular Orbit (ISCO),

$$r_{\rm ISCO} = r_{\rm ms} = M\Big[3 + Z_2 \mp \sqrt{(3 - Z_1)(3 + Z_1 + 2Z_2)}\Big], \tag{33}$$

where

$$Z_1 = 1 + (1 - a_*^2)^{1/3}[(1 + a_*)^{1/3} - (1 - a_*)^{1/3}], \quad Z_2 = \sqrt{3a_*^2 + Z_1^2}, \quad a_* = \frac{a}{M}. \tag{34}$$

Once a particle passes the ISCO, $r < r_{\rm ISCO}$, it plunges into the black hole. We call the region inside ISCO the plunging region.

These circular orbits around a Kerr black hole were summarized in Ref. [83] [see Fig. 9].

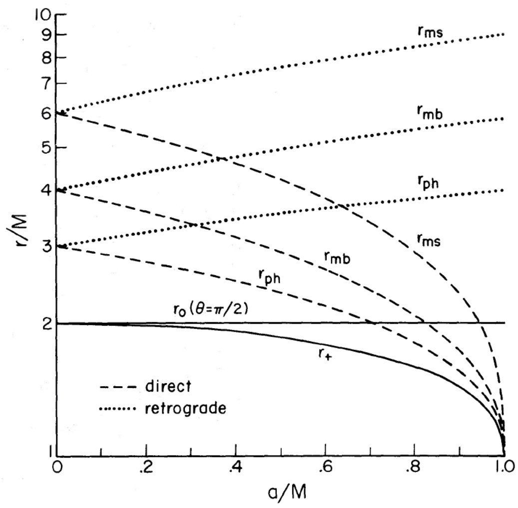

Figure 9.: Radii of prograde/retrograde (dashed/dotted) circular, equatorial orbits around a Kerr black hole with mass M and spin a. Credit to [83].

(Near-)xtremal limit. For the extremal case $a = M$, the Boyer-Lindquist radial locations of r_+, r_{ph}, r_{IBCO} and r_{ISCO} are coincident at $r = M$. However, this is a deception of the Boyer-Lindquist coordinates since timelike orbits, like the IBCO and ISCO, can never lie in the event horizon which is a null surface. In fact, the proper radial distances between these orbits are separated. For astrophysical applications to a rapidly rotating (near-extremal) black hole satisfying $\kappa = \sqrt{1-(a/M)^2} \ll 1$ [Eq. (13)], we consider the limiting behavior of these orbits. The leading order behaviour for the direct circular orbits are obtained as [83]

$$r_+ = M(1+\kappa), \tag{35}$$

$$r_{\mathrm{ph}} = M(1+\frac{2}{\sqrt{3}}\kappa), \tag{36}$$

$$r_{\mathrm{IBCO}} = M(1+\sqrt{2}\kappa), \tag{37}$$

$$r_{\mathrm{ISCO}} = M(1+2^{\frac{1}{3}}\kappa^{\frac{2}{3}}). \tag{38}$$

Note that the radius of ISCO scales differently from those of event horizon, photon orbit and IBCO. As we have reviewed in Sec. 2.2.1, these orbits are situated in a near-horizon throat region. The edge of the throat is given by the ergosurface $r_{0+} = 2M$ for all spin. We observe that ISCO is described in the NHEK limit (with $p = \frac{2}{3}$) while the others are described in the near-NHEK limit (with $p = 1$).

Next, we discuss the location of ISCO. The proper radial distance between two coordinates r_1 and r_2 is given by $d(r_1, r_2) = \int_{r_1}^{r_2} \sqrt{g_{rr}} dr$. Then we have [84]

$$d(r_+, r_{\text{ISCO}}) = \frac{M}{3} \log\left(\frac{2^4}{\kappa}\right) + \mathcal{O}(\kappa^{2/3}), \tag{39}$$

$$d(r_{\text{ISCO}}, r_{0+}) = M\left[1 + \frac{2}{3}\log\left(\frac{1}{\sqrt{2}\kappa}\right)\right] + \mathcal{O}(\kappa^{2/3}). \tag{40}$$

We see that in proper distance the ISCO is located infinitely far from both the event horizon r_+ (in near-NHEK region) and the edge of the throat r_{0+} (in extremal Kerr exterior).

2.3.2 *Massless particle*

Now we study photon trajectories (light rays) in the exterior of a black hole [37]. In the "source-ray-observer" problem of black hole imaging, light rays play a role as bonds which tie the source and the observer. On the one hand, the light rays can be labeled by photon-conserved quantities E, L and $\mathcal{Q}$ [or below in Eq. (41) the impact parameters $\hat{\lambda}$ and $\hat{q}$]. On the other hand, these conserved quantities help connect the locally measured photon motion of a source to that of an observer.

The geodesic equations for a photon are obtained taking $\mu = 0$ in Eqs. (26). From the expressions (24) and (25), we see that any photon trajectory passing through the equatorial plane always has a nonnegative Carter constant since $\mathcal{Q} = p_\theta^2 \geq 0$ when $\theta = \pi/2$. We restrict to positive $\mathcal{Q}$ since we will consider photons either emitted by an equatorial source or on spherical orbits. Furthermore, except for the measure-zero set of light rays with $E = 0$, the photon motion may be described by two independent ratios only, referred to as the *impact parameters* [37, 5],

$$\hat{\lambda} = \frac{L}{E}, \qquad \hat{q} = \frac{\sqrt{\mathcal{Q}}}{E}. \tag{41}$$

The radial and angular potentials for a photon trajectory can be written in terms of the impact parameters, we define for the null case

$$\mathcal{R}(r) = \tilde{\mathcal{R}}(r)/E^2, \qquad \Theta(\theta) = \tilde{\Theta}(\theta)/E^2, \tag{42}$$

while the potentials with tildes are for arbitrary particles, given in Eqs. (27) and (28). Complete information about rays is contained in the null geodesics. It would be helpful to investigate behaviors of rays in the parameter space of $\hat{\lambda}$ and $\hat{q}$ [86, 87]. However, here we only consider two specific cases.

There are basically two ways to study the appearance of the photons near a black hole. One way is to consider the rays received by an observer and trace along them backwards towards the region near the black hole [50]. Another way is to consider the rays connecting a given emitter and a given observer, and then obtain solutions for these rays by solving the geodesic equations [5].

Unstable spherical photon orbits.

We first consider the threshold between captured and escaping rays, which correspond to the unstable spherical photon orbits with constant radial coordinate $r = r_{\rm sp}$. For these photon orbits, we have $dr_{\rm sp}/ds = 0$ and $d^2 r_{\rm sp}/ds^2 = 0$. Then we have $\mathcal{R}(r_{\rm sp}) = 0$ and $\mathcal{R}'(r_{\rm sp}) = 0$, solving which for $\hat{\lambda}$ and $\hat{q}$ gives the critical impact parameters [37]

$$\hat{\lambda}_{\rm c} = -\frac{r_{\rm sp}^2(r_{\rm sp} - 3M) + a^2(r_{\rm sp} + M)}{a(r_{\rm sp} - M)}, \qquad \hat{q}_{\rm c} = \frac{r_{\rm sp}^{3/2}}{a(r_{\rm sp} - M)}\sqrt{4a^2 M - r_{\rm sp}(r_{\rm sp} - 3M)^2}. \tag{43}$$

For these orbits to be unstable, one needs $\mathcal{R}''(r_{\rm sp}) > 0$ which is always true for spherical photon orbits [88]. Recall that the radius of spherical orbits is constrained by the condition $\mathcal{Q} > 0$, thus we always have real positive $\hat{q}$ for such rays. Then solving $\hat{q}_c^2 > 0$ we obtain an range for $r_{\rm sp}$,

$$r_{\rm sp} \in [r_{\rm sp+}, r_{\rm sp-}], \qquad r_{\rm sp\pm} = 2M\Big[1 + \cos\Big(\frac{2}{3}\arccos \pm \frac{a}{M}\Big)\Big]. \tag{44}$$

Rays connecting source to observer.

We also consider light rays connecting a source at $(t_s, r_s, \theta_s, \phi_s)$ to an observer at $(t_o, r_o, \theta_o, \phi_o)$, where subscripts s and o stand for source and observer, respectively. By integrating up the first order differential equations of motion (26) from the source to observer along the rays, we get the integral form equations for the rays $(\hat{\lambda}, \hat{q})$ [5]:

$$\fint_{r_s}^{r_o} \frac{dr}{\pm\sqrt{\mathcal{R}(r)}} = \fint_{\theta_s}^{\theta_o} \frac{d\theta}{\pm\sqrt{\Theta(\theta)}}, \tag{45a}$$

$$\Delta\phi = \phi_o - \phi_s = \fint_{r_s}^{r_o} \frac{a(2Mr - a\hat{\lambda})}{\pm\Delta\sqrt{\mathcal{R}(r)}} dr + \fint_{\theta_s}^{\theta_o} \frac{\hat{\lambda}\csc^2\theta}{\pm\sqrt{\Theta(\theta)}} d\theta, \tag{45b}$$

$$\Delta t = t_o - t_s = \fint_{r_s}^{r_o} \frac{r^2\Delta + 2Mr(r^2 + a^2 - a\hat{\lambda})}{\pm\Delta\sqrt{\mathcal{R}(r)}} dr + \fint_{\theta_s}^{\theta_o} \frac{a^2\cos^2\theta}{\pm\sqrt{\Theta(\theta)}} d\theta, \tag{45c}$$

where the slash notation in the integrals denotes that these integrals are to be evaluated as path integrals along a trajectory. The signs $\pm$ are chosen such that the integrals are always evaluated along the direction of propagation and therefore flip every time when the light ray meets a turning point.

2.4 OBSERVER'S SKY

Each ray received by an observer corresponds to an image on the observer's sky. Description of the image depends on the choice of observer and the impact parameters of the ray.

We introduce the orthonormal frame $\{e_{(\hat{t})}, e_{(\hat{r})}, e_{(\hat{\theta})}, e_{(\hat{\phi})}\}$ for local observers with four-velocity $u^\mu = e_{(\hat{t})}$. This frame basis can be expanded in the Boyer-Lindquist coordinate basis $\{\partial_t, \partial_r, \partial_\theta, \partial_\phi\}$. An observer who moves along constants (r, θ, ϕ) would be a static observer with $u \propto \partial_t$. However, such an observer only exists outside the static limit surface [Eq. (11)]. In the ergosphere, all four Boyer-Lindquist coordinates become spacelike thus these can not correspond to a physical observer. Nevertheless, it is very convenient to use this static observer in the valid domain and this is usually referred to as the *static observer at spacial infinity*. A fruitful frame for treating physical processes in a Kerr-like geometry (7) (especially in the ergoregion) was introduced by Bardeen, known as the *locally nonrotating frame* (LNRF) [83], which is related to the Boyer-Lindquist frame by

$$e_{(t_L)} = e^{-\nu}(\partial_t + \Omega_{\rm bh}\partial_\phi), \qquad e_{(r_L)} = e^{-\mu_1}\partial_r, \qquad e_{(\theta_L)} = e^{-\mu_2}\partial_\theta, \qquad e_{(\phi_L)} = e^{-\psi}\partial_\phi. \tag{46}$$

The LNRF corotates with the Kerr-like geometry as observed by a static observer at infinity which cancels out as much as possible the "frame-dragging" effects of the rotation of the black hole. A local rest observer of LNRF has zero angular momentum due to $L = g_{\mu\nu}p^\mu(\partial_\phi)^\nu = 0$, such an observer then is called a *zero-angular-momentum observer* (ZAMO). ZAMO exists everywhere outside the event horizon. In the limit of $r \to \infty$ in Kerr spacetime (8), a ZAMO and a static observer are related by

$$e_{(t_L)} = \partial_t, \qquad e_{(r_L)} = \partial_r, \qquad e_{(\theta_L)} = r^{-1}\partial_\theta, \qquad e_{(\phi_L)} = (r\sin\theta)^{-1}\partial_\phi. \tag{47}$$

Now we introduce a pair of Cartesian coordinates to describe the positions in the observer's sky [89, 5]. We assume that the spacetime is asymptotically flat and consider a static observer at infinity. We can set up a Cartesian coordinate system $\{x,\ y,\ z\}$ for an observer at a distance r_o with origin at the centre of the apparent position of the black hole. This frame only coincides with the Boyer-Lindquist coordinates for large r while the later is spherical-like. Considering that the spacetime is axisymmetric, we may set the observer to be located at $r_o \to \infty$, $\theta_o \in [0, \pi)$ (exclude the measure-zero case $\theta_o = \pi/2$) and $\phi_o = 0$. We introduce two screen coordinates (α, β) embedded in the Cartesian space. The basis vectors are defined as

$$\hat{\alpha} = \hat{y}, \qquad \hat{\beta} = \mp\cos\theta_o\hat{x} \pm \sin\theta_o\hat{z}. \tag{48}$$

The apparent position of a photon can be described by the observer's screen coordinates (α, β),

$$\vec{x}_s = \alpha\hat{\alpha} + \beta\hat{\beta} = \mp\beta\cos\theta_o\hat{x} + \alpha\hat{y} \pm \beta\sin\theta_o\hat{z}. \tag{49}$$

On the other hand, the apparent position of a photon can also be obtained by tracing back the tangent vector of its trajectory from the observer's position to the celestial plane in the fictitious global

Cartesian system. The photon trajectory can be described by a parametric curve in the 3-dimensional observer's space as

$$\vec{x}(r) = [x(r),\ y(r),\ z(r)], \tag{50}$$

where $r = \sqrt{x^2 + y^2 + z^2}$, which is nothing but the Boyer-Lindquist radial coordinate for large value. The tangent vector of the trajectory at the observer's position (r_o, θ_o, ϕ_o) is given by $\vec{v}_o = \frac{d\vec{x}}{dr}\Big|_o$. In terms of spherical coordinate, using $x = r\sin\theta\cos\phi$, $y = r\sin\theta\sin\phi$ and $z = r\cos\theta$, we obtain

$$\vec{x}_s = \vec{x}_o - r_o\vec{v}_o = -r_o^2\cos\theta_o\frac{d\theta}{dr}\Big|_o\hat{x} - r_o^2\sin\theta_o\frac{d\phi}{dr}\Big|_o\hat{y} + r_o^2\sin\theta_o\frac{d\theta}{dr}\Big|_o\hat{z}. \tag{51}$$

From Eqs. (49) and (51), we obtain[3] [89]

$$\alpha = -r_o^2\sin\theta_o\frac{d\phi}{dr}\Big|_o, \qquad \beta = \pm r_o^2\frac{d\theta}{dr}\Big|_o. \tag{52}$$

For the Kerr case, we find that

$$\alpha = -\frac{\hat{\lambda}}{\sin\theta_o} + \mathcal{O}(\frac{1}{r_o}), \tag{53a}$$

$$\beta = \pm\sqrt{\hat{q}^2 + a^2\cos^2\theta_o - \hat{\lambda}^2\cot^2\theta_o} + \mathcal{O}(\frac{1}{r_o}) = \pm\sqrt{\Theta(\theta_o)}. \tag{53b}$$

Note that we require $\Theta(\theta_o) \geq 0$ such that photons with the impact parameters $\hat{\lambda}$ and $\hat{q}$ can reach the observer at a desired inclination.

2.5 SOURCE AND IMAGE

Now we consider the appearance of black holes relative to an observer at spacial infinity. Since black holes are invisible by themselves, the first question we should answer is what we are really looking

3 In some literatures, impact parameters are defined by these screen coordinates instead of the photon conserved parameters $(\hat{\lambda}, \hat{q})$ as what we have defined. The screen coordinates can be expressed in LNRF (46) as $\alpha = -r_o\frac{p^{(\phi_L)}}{p^{(t_L)}}$, $\beta = r_o\frac{p^{(\theta_L)}}{p^{(t_L)}}$, which are proportional to cosines of reception angles of rays to a ZAMO [37].

at? We have reviewed a series of studies in Sec. 1.2 for different light sources. Next, we introduce some technical details of calculating their images.

Bare black hole. Black holes with no nearby emitting sources are named as bare black holes. A bare black hole is illuminated instead by background light originating from very far away and casting a shadow region in the observer's sky where no light arrives. The apparent boundary of the shadow, i.e., the critical curve, is a direct consequence of the unstable spherical photon orbits. The impact parameters for such light rays are given in Eq. (43), which after plugging in the screen coordinates (53) gives the critical curve $[\alpha(r_{\rm sp}), \beta(r_{\rm sp})]$. The radius of spherical orbits should satisfy the constrains Eq. (44) and $\Theta(\theta_o) \geq 0$ [37].

In the extremal limit [5] $a \to M$, the critical curve $[\alpha(r_{\rm sp}), \beta(r_{\rm sp})]$ is obtained as

$$\alpha(r_{\rm sp}) = -\frac{1}{M\sin\theta_o}(r_{\rm sp}^2 - M^2 - 2Mr_{\rm sp}), \tag{54a}$$

$$\beta(r_{\rm sp}) = \pm\frac{1}{M}\sqrt{r_{\rm sp}^3(4M - r_{\rm sp}) + M^4\cos^2\theta_o - (r_{\rm sp}^2 - M^2 - 2Mr_{\rm sp})^2\cot^2\theta_o}, \tag{54b}$$

with $r_{\rm sp} \in [M, 4M]$. This does not in general describe a closed curve and for an open curve there are two endpoints at $[\alpha(M), \beta(M)]$. The inclination θ_o is restricted by $\Theta(\theta_o) \geq 0$, thus the condition for an open curve is obtained for $\beta(M)^2 \geq 0$ which gives $\theta_{\rm crit} < \theta_o < \pi - \theta_{\rm crit}$ with $\theta_{\rm crit} = \arctan[(4/3)^{1/4}] \approx 47^\circ$. This critical curve is shown in Fig. 4 (without the leftmost straight line) for a distant observer sitting in the equatorial plane.

Since the apparent boundary of a shadow is closed for all astrophysical black holes with $a < M$, the above discussion has missed an important piece which corresponds to photons passing through the near-horizon region. To recover it, we consider the near-horizon and near-extremal limit

$$a = M\sqrt{1-\kappa^2}, \qquad r_{\rm sp} = M(1 + \kappa R_{\rm sp}). \tag{55}$$

Then the critical curve is obtained as

$$\alpha(R_{\rm sp}) = -\frac{2M}{\sin\theta_o} + \mathcal{O}(\kappa), \tag{56a}$$

$$\beta(R_{\rm sp}) = \pm M\sqrt{3+\cos^2\theta_o - 4\cot^2\theta_o - \frac{4}{R_{\rm sp}}} + \mathcal{O}(\kappa). \tag{56b}$$

Again, the range of $R_{\rm sp}$ is constrained by Eq. (44) and $\Theta(\theta_o) \geq 0$, from which we have

$$R_{\rm sp} \in \Big[\frac{2}{\sqrt{3+\cos^2\theta_o - 4\cot^2\theta_o}}, \infty\Big) + \mathcal{O}(\kappa). \tag{57}$$

As $\kappa \to 0$, this gives the missing piece, the leftmost straight line in Fig. 4, of an open curve given by Eq. (54). This missing curve is called the NHEKline [5] as emissions near the line correspond to photons coming from the NHEK region of the spacetime. Next, we discuss the space-time-geometrical origin of the NHEKline.

NHEK photons [5]. It is observed that the NHEK source and distant observer are adapted to two distinct extremal limits (see Sec. 2.2.1), which forces the NHEK source to appear on the NHEKline. To consider the (near-)extremal limit of spacetime geometry, we have introduced the near-extremal parameter κ in Eq. (13) and the Bardeen-Horowitz coordinates $\tilde{T}$, $\tilde{\Phi}$ and $\tilde{R}$ in Eq. (14). These are related to the Boyer-Lindquist coordinates by

$$\partial_\phi = \partial_{\tilde{\Phi}}, \qquad \partial_t + \frac{1}{2M}\partial_\phi = \frac{\kappa^p}{2M}\partial_{\tilde{T}}. \tag{58}$$

A near-horizon photon with four-momentum p^μ has a finite "energy" $\tilde{E} = -p_\mu \partial^\mu_{\tilde{T}}$. Then, given $0 < p \leq 1$, from Eqs. (58) and (20) we have $\hat{\lambda} = L/E = 2M$ as $\kappa \to 0$. This means that all photons emitted in the NHEK region are constrained to be near the superradiant bound[4]. A distant observer is adapted to the usual extremal limit ($p = 0$) and has the standard observed sky described by the screen coordinates (53). Therefore, we have shown that any photons emitted in the NHEK and

4 The superradiant bound of a Kerr black hole is given by $E = \Omega_{\rm H} L$, where $\Omega_{\rm H} = \Omega_{\rm bh}(r_+) = a/(2Mr_+)$. In the extremal limt, we have $\Omega_{\rm H} = 1/(2M)$ thus $\hat{\lambda} = 2M$.

near-NHEK regions, including those emitted on ISCO [Eq. (38)], IBCO [Eq. (37)] and more general orbits, will end up on the NHEKline.

Orbiting emitter. For a point source orbiting on a tight orbit around a black hole, we will study its image explicitly in next section, paying spacial attention to an emitter in the near-horizon region of an near-extremal Kerr black hole. In following chapters, we generalize this study to the Kerr black hole surrounded by a plasma, Kerr-like black holes in MOG theory and Kerr-like black holes in heterotic string theory, respectively.

2.6 ORBITING EMITTER NEAR ISCO OF A NEAR-EXTREMAL KERR BLACK HOLE

We review the optical appearance of a point-like orbiting emitter [5] (see also the pioneering work [90, 46]). In Sec. 2.6.1, we set up the imaging problem for a general Kerr black hole in a vacuum background. We first describe the orbiting emitter and its observational quantities, and then write down the lens equations for the light rays. In Sec. 2.6.2, we solve this problem in the near-extremal limit and illustrate the results. We will introduce the necessary steps of the computations which serve as a preview for the analogues in the following chapters. Therefore, in the following chapters we only give the results and some main steps. We relegate the detailed calculations of the integrals and image flux to appendices.

2.6.1 *General setup*

2.6.1.1 *Orbiting emitter*

We consider a point source lying in the equatorial plane ($\theta_s = \pi/2$) and orbiting on a circular geodesic at radius r_s. The coordinate angular momentum of this emitter is given in Eq. (30). In order to interpret the conserved quantities for photons emitted from this source using local observables, we introduce the local rest frame of the orbiting emitter. The time-leg of this frame is just the four-velocity of the emitter, $e^{\mu}_{(t_s)} = u^{\mu}$ ($u_{\mu}u^{\mu} = -1$), while the space-legs are choose to be three spacelike unit vectors orthogonal to $e^{\mu}_{(t_s)}$,

$$e_{(t_s)} = \gamma\sqrt{\frac{\Xi}{\Delta\Sigma}}(\partial_t + \Omega_s\partial_\phi), \qquad e_{(r_s)} = \sqrt{\frac{\Delta}{\Sigma}}\partial_r, \qquad e_{(\theta_s)} = \frac{1}{\sqrt{\Sigma}}\partial_\theta, \tag{59a}$$

$$e_{(\phi_s)} = \gamma v_s\sqrt{\frac{\Xi}{\Delta\Sigma}}(\partial_t + \Omega_{\rm bh}\partial_\phi) + \gamma\sqrt{\frac{\Sigma}{\Xi}}\partial_\phi, \tag{59b}$$

where

$$v_s = \frac{\Xi}{\Sigma\sqrt{\Delta}}(\Omega_s - \Omega_{\rm bh}) \quad \text{and} \quad \gamma = \frac{1}{\sqrt{1-v_s^2}} \tag{60}$$

are the three-velocity and boost factor relative to the ZAMO [see Eq. (46)]. Here and hereafter in this subsection, the functions Ξ, Δ, Σ and $\Omega_{\rm bh}$ are given in Eqs. (9) and (8) and evaluated at (r_s, θ_s).

For photons observed by a distant observer, the conserved energy E is redshifted from its local measured energy $E_s = p^{(t_s)}$. The redshift factor g is given by

$$g = \frac{E}{E_s} = \frac{E}{p^{(t_s)}} = \frac{1}{\gamma}\sqrt{\frac{\Delta\Sigma}{\Xi}}\frac{1}{1-\Omega_s\hat{\lambda}}. \tag{61}$$

Then the conserved quantities (impact parameters) $\hat{\lambda}$ and $\hat{q}$ can be interpreted with the help of emission angles (Θ_s, Φ_s) by using $\cos\Phi_s = p^{(\phi_s)}/p^{(t_s)}$ and $\cos\Theta_s = -p^{(\theta_s)}/p^{(t_s)}$, as

$$\hat{\lambda} = \frac{\cos\Phi_s + v_s}{(\Sigma/\Xi)\sqrt{\Delta} + \Omega_s\cos\Phi_s + \Omega_{\rm bh}v_s}, \qquad \hat{q} = \mp\frac{r_s\cos\Theta_s}{g}. \tag{62}$$

Note that the cosines of emission angles are bounded in $[-1, 1]$, which will constraint the impact parameters of light rays emitted from the orbiting emitter.

2.6.1.2 *Observational quantities*

We consider the following observational quantities of the emitter relative to a distant observer, the image position, redshift factor and energy flux, which can be expressed in terms of the photon impact parameters $\hat{\lambda}$ and $\hat{q}$.

The apparent position of an image on the observer's sky is described by the screen coordinates (α, β) given in Eq. (53). The redshift factor of the image is given in Eq. (61). The energy flux of the image is determined by the product of observed intensity (flux per unit solid angle) and the apparent size of solid angle. We assume that the orbiting emitter has a proper radius $\rho \ll M$ and emits isotropically from its surface with intensity I_s in the local rest frame. The intensity relative to a distant observer is related with this local measured intensity by [91]

$$I_o = g^4 I_s. \tag{63}$$

The element of the apparent solid angle is $d\alpha d\beta / r_o^2$, then the energy flux through the apparent region of the image is given by [46]

$$F_o = \iint \frac{d\alpha d\beta}{r_o^2} g^4 I_s. \tag{64}$$

The detailed calculation of the image flux is given in App. C.

2.6.1.3 *Lens equations*

In Sec. 2.3.2, we have reviewed the equations for light rays connecting a given source to a given observer [Eqs. (45)]. Now we make specific choices for the source and observer. For the orbiting emitter, we have the following coordinates: orbital radius r_s, orbital plane $\theta_s = \pi/2$, emission time t_s and $\phi_s = \Omega_s t_s$. For a distant observer, we may choose $r_o \to \infty$, $\phi_o = 2\pi N$ with N[5] an integral (physically equivalent to $\phi_o = 0$), inclination angle $\theta_o \in (0, \pi/2)$ and reception time t_o. Then, by solving Eqs. (45) for given r_s and θ_o, one can write t_s, $\hat{\lambda}$ and $\hat{q}$ as functions of t_o. The emission time t_s is not of observable interest and may be decoupled from these equations by using $\phi_s = \Omega_s t_s$. Note that $\phi_o - \Delta\phi = \phi_s = \Omega_s t_s = \Omega_s(t_o - \Delta t)$, we then have a new equation

$$\Delta\phi - \Omega_s \Delta t = -\Omega_s t_o + 2\pi N, \tag{65}$$

5 In the time interval $[t_s, t_o]$, the winding numbers of the light ray and the emitter are, respectively, $n = \text{mod}_{2\pi}\Delta\phi$ and $n_s = \text{mod}_{2\pi}\Omega_s \Delta t$. Then from Eq. (65) (note also that $\text{mod}_{2\pi}\Omega_s t_o = 0$) we see that N is the net winding number satisfying $N = n - n_s$.

where $\Delta\phi$ and Δt are given in Eqs. (45b) and (45c). Together with Eq. (45a), we are left with two equations for the two variables $\hat{\lambda}$ and $\hat{q}$ at a given time t_o. Solving these two equations will give time-dependent rays which correspond to time-dependent images of the emitter.

Regarding to the turning points along the light rays, it is helpful to introduce labels to distinguish different rays and to eliminate the slash notions in the integral Eqs. (45). For the radial direction, we introduce $b = 0$ for direct rays with no turning point and $b = 1$ for the reflected rays with one turning point. For the angular direction, we introduce $m \geq 0$ representing the number of turning points, and introduce $s = \in \{+1, -1\}$ denoting the final sign of p_θ. The radial turning point appears at $r_{\min}$ which is the largest real root of $\mathcal{R}(r) = 0$, while angular turning points appear at $\theta_\pm$ which are roots of $\Theta(\theta) = 0$. We require $r_{\min} < r_s$ such that the light can reach a distant observer.

Then, we can reexpress the Eqs. (45a) and (65) as the Kerr *lens equations*

$$I_r + b\tilde{I}_r = G_\theta^{m,s}, \tag{66a}$$

$$J_r + b\tilde{J}_r + \frac{1}{M}(\hat{\lambda}G_\phi^{m,s} - \Omega_s a^2 G_t^{m,s}) = -\Omega_s t_o + 2\pi N, \tag{66b}$$

where we have defined $G_i^{m,s} = \hat{G}_i$ for $m = 0$ and $G_i^{m,s} = mG_i - s\hat{G}_i$ for $m \geq 0$, with $i \in \{t, \theta, \phi\}$ and

$$G_i = M\int_{\theta_-}^{\theta_+} g_i(\theta)d\theta, \qquad \hat{G}_i = M\int_{\theta_o}^{\pi/2} g_i(\theta)d\theta \tag{67}$$

and $g_\theta(\theta) = [\Theta(\theta)]^{-1/2}$, $g_\phi(\theta) = \csc^2\theta[\Theta(\theta)]^{-1/2}$ and $g_t(\theta) = \cos^2\theta[\Theta(\theta)]^{-1/2}$; and

$$I_r = M\int_{r_s}^{r_o}\frac{dr}{\sqrt{\mathcal{R}(r)}}, \qquad \tilde{I}_r = 2M\int_{r_{\min}}^{r_s}\frac{dr}{\sqrt{\mathcal{R}(r)}}, \tag{68a}$$

$$J_r = \int_{r_s}^{r_o}\frac{\mathcal{J}_r}{\sqrt{\mathcal{R}(r)}}dr \qquad \tilde{J}_r = 2\int_{r_{\min}}^{r_o}\frac{\mathcal{J}_r}{\sqrt{\mathcal{R}(r)}}dr \tag{68b}$$

$$\mathcal{J}_r = \frac{1}{\Delta}\Big[a(2Mr - a\hat{\lambda}) - \Omega_s r\Big(r^3 + a^2(r+2M) - 2aM\hat{\lambda}\Big)\Big]. \tag{68c}$$

Therefore, for each given choice of the net winding number N, and number of radial and angular turning points, b and m, and the final polar orientation s, we have a set of lens equations [Eqs. (66)] for a light ray $(\hat{\lambda}, \hat{q})$ connecting source to observer. In general, the lens equations can only be solved numerically. Nevertheless, these can be much simplified in the near-extremal regime which will be analytically computed in next section.

2.6.2 *Near-extremal case*

2.6.2.1 *Orbiting emitter and its observables*

Now we consider a near-extremal Kerr black hole and an emitter orbiting on (or near) the direct ISCO of the black hole. We have reviewed the near-extremal limiting behavior of the ISCO in Sec. 2.3.1 [see Eq. (38)]. We introduce a new small parameter $\epsilon = \kappa^{2/3} \ll 1$, thus the near-extremal limit (13) becomes

$$a = M\sqrt{1-\epsilon^3}, \tag{69}$$

under which the ISCO is put away from the event horizon at a coordinate distance $\sim \epsilon$, explicitly $r_{\text{ISCO}} = M[1 + 2^{1/3}\epsilon + \mathcal{O}(\epsilon^2)]$. The expansion of near-extremality can be viewed as an expansion in the divergent proper depth d from the ISCO to the edge of the extremal throat since at the leading order we have $\epsilon = 2^{-1/3}e^{1-d/M}$ [see Eq. (40)].

We then choose the following radial coordinate for the emitter,

$$r_s = M(1+\epsilon\bar{R}) + \mathcal{O}(\epsilon^2), \qquad \bar{R} \geq 2^{1/3}. \tag{70}$$

Photons from the emitter are then adapted to the $p = 2/3$ NHEK photons discussed in Sec. 2.5. As we have shown below Eq. (58) that the impact parameter $\hat{\lambda}$ of a NHEK photon is strongly constrained, which forces the photon to appear on the NHEKline [given by Eqs. (56) and (57)]. This can also be seen from the expansion of Eq. (62) in ϵ,

$$\hat{\lambda} = 2M + \frac{3M\bar{R}\cos\Phi_s}{1+2\cos\Phi_s}\epsilon + \mathcal{O}(\epsilon^2). \tag{71}$$

In order to keep track of the small corrections, we introduce a new quantity λ by

$$\hat{\lambda} = 2M(1 - \epsilon\lambda). \tag{72}$$

In addition, the potentials $\Theta(\theta)$ and $\mathcal{R}(r)$ should always be non-negative along a ray from the NEHK region to the far asymptotically flat region, which will put constraints on the impact parameters. In the near-extremal limit, $\Theta(\theta) > 0$ gives

$$3 - \frac{\hat{q}^2}{M^2} < 4(1 - \epsilon\lambda + \epsilon^2\lambda^2). \tag{73}$$

It is convenient to introduce a dimensionless shifted constant q by [4]

$$\hat{q}^2 = M^2(3 - q^2). \tag{74}$$

Positivity of $R(r)$ along the ray requires $q^2 > 0$.

Expansions of observables. It is convenient to work with the coordinates $R = \kappa^p \tilde{\mathcal{R}}$ [see Eq. (14)]. Our observer is at $R_o = (r_o - M)/M \approx r_o/M$. For the near-extremal case with Eqs. (69), (70), (72) and (74), we now expand in ϵ the various quantities that are of observational interests. The screen coordinates [Eq. (53)] for the apparent position are given by

$$\alpha = -\frac{2M}{\sin\theta_o} + \mathcal{O}(\epsilon), \qquad \beta = sM\sqrt{3 - q^2 + \cos^2\theta_o - 4\cot^2\theta_o} + \mathcal{O}(\epsilon). \tag{75}$$

Note that the leading order position does not depend on λ. Nonnegativity of $\Theta(\theta)$, i.e., $\beta^2 \geq 0$ gives a range of q

$$q \in \left[0, \sqrt{3 + \cos^2\theta_o - 4\cot^2\theta_o}\right]. \tag{76}$$

Of course Eqs. (75) and (76) show that the images do appear on the vertical NHEKline and vanish when the NHEKline disappears for $\theta_o < \theta_{\text{crit}} \approx 47^\circ$. The redshift factor (61) is given by

$$g = \left(\sqrt{3} + \frac{4}{\sqrt{3}}\frac{\lambda}{\bar{R}}\right)^{-1} + \mathcal{O}(\epsilon). \tag{77}$$

The direction cosines to the leading order are given by $\cos\Phi_s = \sqrt{3}/2(g - 1/\sqrt{3}) + \mathcal{O}(\epsilon)$ and $\cos\Theta_s = (-1)^{m+1} sg\sqrt{3 - q^2} + \mathcal{O}(\epsilon)$. Note that since $\cos\Phi_s \leq 1$ the redshift factor has an upper bound $g \leq \sqrt{3}$ with the equality corresponding to a net blueshift for photons emitted in the forward direction, $\Phi_s = 0$. The normalized image flux relative to the "Newtonian flux", $F_o/F_{\rm N}$ [see Eq. (336) in App. C], is given by

$$\frac{F_o}{F_{\rm N}} = \epsilon g^3 \frac{q\bar{R}\csc\theta_o}{D_s\sqrt{1-q^2/3}|\beta/M|}\left|\det\frac{\partial(B,A)}{\partial(\lambda,q)}\right|^{-1}, \tag{78}$$

where $D_s = (q^2\bar{R}^2 + 8\lambda\bar{R} + 4\lambda^2)^{1/2}$, and A and B are defined in App. C which are written in terms of radial integrals (68) and angular integrals (67). These integrals are performed in the near-extremal regime in appendices A and B. Then from the results of these integrals we find that the leading order determinant in Eq. (78) scales as $\log\epsilon$. Therefore, the normalized image flux $F_o/F_{\rm N}$ scales as $\epsilon/\log\epsilon$ at the leading order in ϵ. The orbital frequency and period of the emitter are

$$\Omega_s = \frac{1}{2M} - \frac{3\bar{R}}{8M}\epsilon + \mathcal{O}(\epsilon^2), \qquad T_s = \frac{2\pi}{\Omega_s} = 4\pi M + \mathcal{O}(\epsilon). \tag{79}$$

Exactly extremal problem. To the leading order in ϵ, the expansions of observables are identical if we instead expand these observables with $a = M$ and the same Eqs. (70), (72) and (74). This describes the image of an emitter orbiting near the ISCO of an exactly extremal black hole, and the small parameter ϵ represents the deviation from the orbit to the event horizon. Therefore, we see that the image of a near-ISCO emitter in the near-extremal case is mapped to that in an exactly extremal case. Note that the same agreement between near-extremal Kerr and extremal Kerr was also observed for the gravitational waves signals emitted by a near-ISCO source in EMRIs [66].

2.6.2.2 *Solutions of lens equations*

The observational quantities of the image are determined by the photon impact parameters $\hat{\lambda}$ and $\hat{q}$, which can be obtained by solving the lens equations (66). In this section, we solve these equations in the near-extremal limit for the new quantities λ and q. Therefore, we can get the leading order observational quantities (75), (77) and (78). When expanding the lens equations in small ϵ, we see that the leading order terms grow as $\log\epsilon$ and λ does not appear, which only determines the behaviour of angular turning points m. In order to solve for λ, we must go to the subleading $\mathcal{O}(\epsilon^0)$ equations.

First equation. We now solve the first equation in Eqs. (66),

$$I_r + b\tilde{I}_r = mG_\theta - s\hat{G}_\theta. \tag{80}$$

The radial integrals I_r and $\tilde{I}_r$ are approximately performed in App. A using the MAE method, and angular integrals G_θ, $\hat{G}_\theta$ are performed as elliptic functions in App. B, which to the leading order depend only on q but not λ. The results for the radial integrals are given by

$$I_r = -\frac{1}{q}\log\epsilon + \frac{1}{q}\log\left[\frac{4q^4 R_o}{(qD_o + q^2 + 2R_o)(qD_s + q^2\bar{R} + 4\lambda)}\right] + \mathcal{O}(\epsilon), \tag{81a}$$

$$\tilde{I}_r = \frac{1}{q}\log\left[\frac{(qD_s + q^2\bar{R} + 4\lambda)^2}{4(4-q^2)\lambda^2}\right] + \mathcal{O}(\epsilon), \tag{81b}$$

where

$$D_s = \sqrt{q^2\bar{R}^2 + 8\lambda\bar{R} + 4\lambda^2}, \qquad D_o = \sqrt{q^2 + 4R_o + R_o^2}. \tag{82}$$

Note that, as $\epsilon \to 0$, the left-hand-side of the first equation grows as $\log\epsilon$ which requires that m on the right-hand-side behaves similarly. In order to solve this equation to the subleading order, it is convenient to introduce

$$m = -\frac{1}{qG_\theta}\log\epsilon + \bar{m}, \qquad \Upsilon \equiv \frac{q^4 R_o}{q^2 + 2R_o + qD_o} e^{-qG_\theta^{\bar{m},s}} > 0. \tag{83}$$

Then the leading order equation is satisfied automatically and the subleading equation is given by

$$4^{1-b}\Upsilon(4-q^2)^{-b}\lambda^{-2b}(q^2\bar{R} + qD_s + 4\lambda)^{2b-1} = 1. \tag{84}$$

Note that in the large-R_o limit,we have $\Upsilon = [q^4\exp(-qG_\theta^{\bar{m},s})]/(q+2) + \mathcal{O}(R_o^{-1})$ which is independent of R_o to the leading order in $1/R_o$. For each given choice of m, b, s and q, the subleading equation (84) is just a quadratic equation of λ. Next we solve this equation for the $b = 0$ and

$b = 1$ separately and combine the final results. This equation does not always have a solution. The existence of a solution requires

$$\bar{R} < \frac{4\Upsilon}{q^2}\Big(1 + \frac{2}{\sqrt{4-q^2}}\Big) \quad \text{if} \quad b = 0, \tag{85a}$$

$$\bar{R} > \frac{4\Upsilon}{q^2}\Big(1 + \frac{2}{\sqrt{4-q^2}}\Big) \quad \text{if} \quad b = 1, \tag{85b}$$

under which condition the solution is given by

$$\lambda = \frac{2\Upsilon}{4-q^2}\Big[2 - q\sqrt{1 + \frac{4-q^2}{2\Upsilon}\bar{R}}\Big]. \tag{86}$$

Therefore, given m, b and s, solving the first equation (80) gives a function $\lambda(q)$ [Eq. (86)] in an allowed range of q satisfying Eq. (85).

Second equation. Then we solve the second equation in Eqs. (66)

$$J_r + b\tilde{J}_r + \frac{1}{M}(\hat{\lambda} G_\phi^{m,s} - \Omega_s a^2 G_t^{m,s}) = -\Omega_s t_o + 2\pi N. \tag{87}$$

Since the problem is periodic with a period $T_s = 2\pi/\Omega_s$, it is convenient to introduce a dimensionless time coordinate by $\hat{t}_o = t_o/T_s = t_o/(4\pi M) + \mathcal{O}(\epsilon)$ restricting to a single period $\hat{t}_o \in [0, 1]$. Then the second equation can be rewritten as

$$\hat{t}_o = N + \mathcal{G}, \qquad \mathcal{G} = -\frac{1}{2\pi}\Big(J_r + b\tilde{J}_r + 2G_\phi^{m,s} - \frac{1}{2}G_t^{m,s}\Big). \tag{88}$$

The radial integrals J_r and $\tilde{J}_r$ are computed using the MAE method in App. A which have a similar structure as the I integrals. The angular integrals $G_\phi^{m,s}$ and $G_t^{m,s}$ are given in App. B, which in the near-extremal approximation are functions of q. Combining with the solution obtained from the first equation [Eq. (86)], the second equation (88) then gives a function

$$\hat{t}_o(q) = \hat{t}_o[q, \lambda(q)] \tag{89}$$

for each given choice of m, s, b having a non-vanishing range of q. Note also that as we require $\hat{t}_o \in [0, 1]$, N is always uniquely determined for each value of q. Then, for each allowed value of

N, inverting Eq. (89) in each monotonic domain gives an inverse $q_i(\hat{t}_o)$ with i a discrete integral labeling the corresponding domain. We give an illustrating example for determining $q_i(\hat{t}_o)$ in Fig. 15 in Chapter 4.

To summarize, by solving the lens equations, we obtain the time-dependent light rays with conserved quantities $q(\hat{t}_o)$ and $\lambda[q(\hat{t}_o)]$ which corresponds to tracks of the image on observer's sky. Each track segment of the image can be labeled by (m, b, s, N, i).

2.6.2.3 *Observational appearance*

We now describe the observational quantities of the emitter's image with figures and discuss them in detail. The image depends on the choice of four physical parameters: the near-extremality of black hole spin ϵ, the orbital radius of the emitter $\bar{R}$, the observer's coordinate distance R_o and inclination θ_o. In order to make the near-extremal approximations accurate, one must choose $\epsilon \ll 1$ and $R_o \gg 1$. For the emitter to be on a stable circular orbit of this high-spin black hole, one must choose $\bar{R} \geq 2^{1/3}$. For there to exist any image at all, one must choose $47^\circ < \theta_o < 90^\circ$. We will mainly consider the following example:

$$\epsilon = 0.01, \quad \bar{R} = \bar{R}_{\text{ISCO}} = 2^{1/3}, \quad R_o = 100, \quad \theta_o = \frac{\pi}{2} - \frac{1}{10} = 84.27^\circ. \tag{90}$$

This describes a hot spot (orbiting emitter) on the ISCO of a near-extremal Kerr black hole with spin $a = 0.9999995M$, viewed by a distant observer from a nearly edge-on inclination. In addition, we also consider the results for high-spin black holes with $\epsilon = 0.15$[6] and $\epsilon = 0.001$ for comparison.

From the previous subsections, we have obtained the time-dependent impact parameters (λ, q) for each track segment of an image labeled by (m, b, s, N, i). Then, we may compute the main observational quantities of the segment: apparent position (α, β) [Eq. (75)], redshift factor g [Eq. (77)] and normalized flux F_o/F_{N} [Eq. (78)]. By including all such segments for all choices of (m, b, s, N, i),

6 Even though the approximation is not sufficiently accurate for this value, it corresponds to a physically interesting bound, the Thorne limit $a = 0.998M$, which is worth to be compared.

one may build up the complete observable information of the image. Formally, a light ray may orbit around the black hole infinitely many times between the angular turning points before reaching to the observer. Therefore, there are infinitely many choices for m and N. However, in practice we only need to consider a few values of m and N since the fluxes for others are vanishingly small. Next, we illustrate the main feature of the brightest few images.

We show the main observational quantities[7] of the most important few images[8] for three cases of high spin in Fig 10. We see that there are continuous image tracks moving on the NHEKline which are lined up by the track segments. These different continuous tracks have been coded with different colours. In each case, the green line is a bright primary image while the others are secondary images. Over each period, the primary image moves downwards while blueshifts become brighter after appearing near the center of the NHEKline. At peak flux of the iamge, there is a net blueshift $g \approx 1.6$ which corresponds to light rays emitted near the forward ϕ-direction $g \sim \sqrt{3}$. This net blueshift reflects the fact that the Doppler boost from the ultrarelativistic ISCO dominates over the gravitational redshift. The secondary images are negligible in general except when different image tracks intersect which corresponds to optical caustics. The secondary images appear with a typical redshift $g = 1/\sqrt{3}$, corresponding to $\lambda \sim 0$. For $\epsilon = 0.15$, 0.01 and 0.001, the typical image positions and redshifts remain unchanged, while the typical normalized flux of images scales as $\epsilon / \log \epsilon$.

We see that the energy of emission is shifted by the typical factors $g = \sqrt{3}$ (primary image) or $g = 1/\sqrt{3}$ (secondary image). For the emission of iron line at $E_{\mathrm{FeK}\alpha} = 6.4$ keV, the energy will be shifted to 11.1 keV and 3.7 keV, respectively. This might be a typical observational signal for a high spin black hole. Note that this is close to the unidentified spectral line at 3.5 keV [92].

7 Here, we only introduce several main features. More details will be discussed in the MOG case in Chapter 4.

8 Taking $\epsilon = 0.01$ for example, this includes track segments with (m, b, s)=$(0,0,-1)$, $(1,0,-1)$, $(1,0,1)$, $(2,0,-1)$, $(2,0,1)$, $(2,1,-1)$, $(3,0,-1)$, $(3,0,1)$, $(3,1,-1)$, $(3,1,1)$, $(4,0,1)$ and $(4,1,1)$. We have also imposed a small-q cut-off at $q = \epsilon^{1/4}/3$.

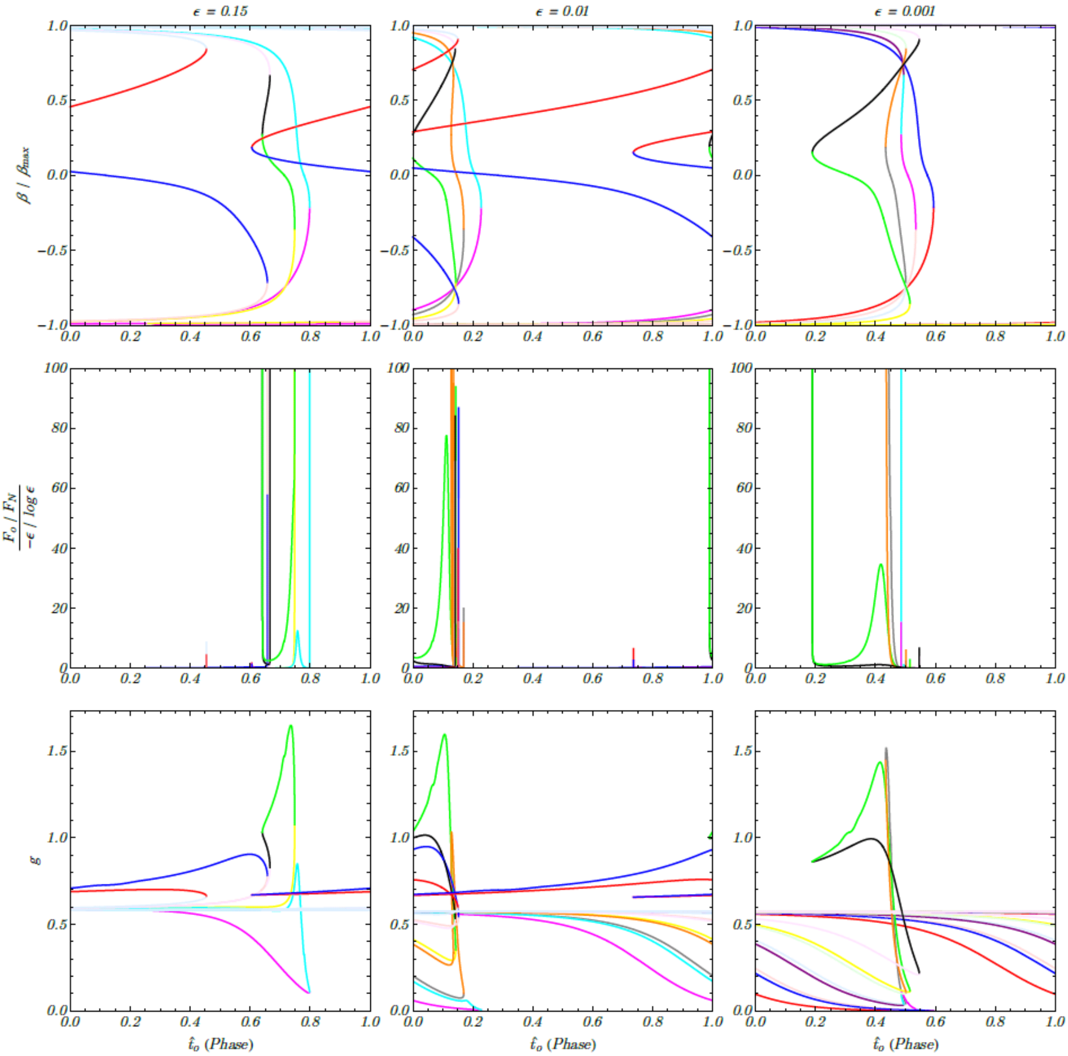

Figure 10.: Main observables of the brightest few images (see footnote 8) of an orbiting hot spot for three different values of spin. These images appear periodically on the vertical NHEKline. We have depicted each continuous image track by the same color which may consists of multiple segments labeled by (m, b, s, N, i). In each case, the green line describes a primary image while the others are for secondary images. A video animation for these images can be found here. Credit to [5]

3

INFLUENCE OF A SURROUNDING PLASMA

3.1 INTRODUCTION

Nowadays, we are entering an exciting new era of precise astronomical observations of black holes. The observations with gravitational waves have achieved a celebrating breakthrough in recent years [16, 17, 18, 19, 20]. Meanwhile, the Event Horizon Telescope (EHT) collaboration is making efforts on capturing the first image of an astrophysical black hole through electromagnetic wave observations [33]. Therefore, there is increasing interest in studying theoretical templates for those observations among the gravity community [93, 35]. The optical signature of a high-spin Kerr black hole at EHT has been studied recently in Refs. [5, 55, 94], where the authors found some striking signatures which may serve as a 'smoking gun' to identify a high-spin black hole in the universe. A generalization of these signatures for a Kerr-like black hole in a modified gravity has been discussed in Ref. [1]. In these studies, the light rays were assumed as lightlike geodesics of the spacetime without being influenced by the medium they passed through. However, an astrophysical black hole is usually surrounded by a complicated environment (such as a corona, a plasma and jets, etc.) and photons near the black hole have to pass through this before reaching to an observer far away from the black hole. In general, the influence of these surroundings on astronomical observations can not be neglected. Then, what about the signatures at EHT if we take this influence into consideration?

Though there are various forms of matter surrounding a black hole, in this chapter we will only concentrate on the influence of a plasma. Plenty of astronomical phenomena of a black hole in a plasma have been studied ever since the 1960s [95, 96] while there were also some recent studies on gravitational lensing [97, 98, 99, 100, 101, 102, 103], and shadow of black holes [104, 105, 106, 103, 107] and wormholes [108]. Here, we are aiming to find the influence of a plasma on: a) the shape and size of shadow for a high-spin black hole, and b) the image of an orbiting emitter ("hot spot") near the black hole. To achieve this target analytically, we will consider several idealized plasma models which have power-law-like distributions and satisfy a separation condition proposed by Perlick and Tsupko [107]. The shadow for a Kerr black hole in a plasma has been studied in Refs. [105, 107, 109]. However, it is worth to revisit this for a high-spin black hole since doing so helps one to understand the image of a hot spot (and thus, the signature at EHT) better. Moreover, in contrast with these works, we will calculate the shadow either using a different method or with different plasma models (or both). The complete signature at EHT should be the combined information of the black hole shadow and the signal from the hot spot. In addition to the influence on the size and shape of a black hole discussed in [107, 109], we find that there is a special segment of the shadow edge originating from the near-horizon region and is approximately the same for both of the power-law-like models (108) and (109). Moreover, the image position and redshift of the hot spot are obviously influenced by the plasma as well. Furthermore, this observational signature is frequency-dependent and there is a greater influence on light rays with lower frequencies.

This chapter is organized as follows. In Sec. 3.2, we review the photon motion in Kerr spacetime with a plasma and introduce two plasma models with radial power-law-like distributions to be considered later. In Sec. 3.3, we revisit the shadow of a Kerr black hole in the presence of a plasma, in particular, we study the extremal limit of the shadow and the near horizon extremal Kerr line (NHEKline). In Sec. 3.4, we write down the lens equations for an orbiting emitter and find solutions for a near-extremal black hole to the subleading order in the deviation from extremality. In Sec. 3.5, we present the results for the observational appearance of this orbiting emitter and illustrate these with figures. In Sec. 3.6, we give a summary and short conclusion.

3.2 PHOTON MOTION IN KERR SPACETIME WITH A PLASMA

3.2.1 *Photon motion*

We work in the Kerr spacetime which is thought to describe astrophysical black holes in our universe. The Kerr metric in Boyer-Lindquist coordinates, $x = (t, r, \theta, \phi)$, is given by

$$ds^2 = -\frac{\Delta\Sigma}{\Xi}dt^2 + \frac{\Sigma}{\Delta}dr^2 + \Sigma d\theta^2 + \frac{\Xi\sin^2\theta}{\Sigma}(d\phi - \Omega_{\rm bh}dt)^2, \tag{91}$$

where

$$\Sigma = r^2 + a^2\cos^2\theta, \qquad \Delta = r^2 - 2Mr + a^2, \tag{92a}$$

$$\Xi = (r^2 + a^2)^2 - \Delta a^2\sin^2\theta, \qquad \Omega_{\rm bh} = \frac{2aMr}{\Xi}. \tag{92b}$$

We consider that there exists a non-magnetized pressureless plasma with electron frequency [97]

$$\omega_p(x)^2 = \frac{4\pi e^2}{m_e}N_e(x), \tag{93}$$

where e is the electron charge, m_e is the electron mass, and N_e is the electron number density. In the geometric optics limit, the Hamiltonian for a photon propagation through this plasma can be written as [97]

$$H(x,p) = \frac{1}{2}\Big(g^{\mu\nu}(x)p_\mu p_\nu + \omega_p(x)^2\Big), \tag{94}$$

where p_μ are the components of the four-momentum of the photon and $g^{\mu\nu}$ are the contravariant components of the metric. $p = (p_t, p_r, p_\theta, p_\phi)$ are the canonical momentum coordinates.

Note that the plasma has a refractive effect on the photon trajectories and the index of refraction $n(x,\omega)$ is given by

$$n(x,\omega)^2 = 1 - \frac{\omega_p(x)^2}{\omega(x)^2}, \tag{95}$$

where $\omega(x)$ is the photon frequency with respect to the plasma medium. For a photon to be able to propagate through this medium, one should require

$$\omega(x) \geq \omega_p(x). \tag{96}$$

For details with regard to the plasma theory, readers may refer to Refs. [97, 98].

In order to find the equation of motion for photons in the Kerr spacetime with a plasma, we should take care of the plasma frequency. In the vacuum case $\omega_p(x) = 0$, there are four constants of the photon motion: the hamiltonian $H = 0$, the total energy $E = -p_t$, the angular momentum $L = p_\phi$ and the Carter constant $\mathcal{Q} = p_\theta^2 - \cos^2\theta(a^2 p_t^2 - p_\phi^2 \csc^2\theta)$. Provided these constants, the photon trajectories are uniquely determined and one may obtain them by solving the Hamilton-Jacobi (H-J) equation. However, this is no longer the case in general if there is a non-zero plasma. For photons propagating through a plasma, the Hamiltonian $H = 0$ still holds. If we assume that the plasma frequency depends only on r and θ, then $E = -p_t$ and $L = p_\phi$ are still constants of photon motion since $\partial_t H = 0$ and $\partial_\phi H = 0$. For later reference, we introduce ω_0 to denote the photon frequency measured at infinity, then we have $E = \hbar\omega_0$ (hereafter we set $\hbar = 1$ for convenience). Next, to make the H-J equation separable, the plasma frequency $\omega_p(r,\theta)$ should take the following form [107],

$$\omega_p(r,\theta)^2 = \frac{f_r(r) + f_\theta(\theta)}{r^2 + a^2\cos^2\theta}, \tag{97}$$

with some functions $f_r(r)$ and $f_\theta(\theta)$. Therefore, we can get a generalized separation constant,

$$\begin{aligned} \mathcal{K} : &= p_\theta^2 + (a\omega_0 \sin\theta - L\csc\theta)^2 + f_\theta(\theta) \\ &= -\Delta p_r^2 + \frac{1}{\Delta}\left[(r^2+a^2)\omega_0 - aL\right]^2 - f_r(r). \end{aligned} \tag{98}$$

Follow the convention of Refs. [4, 5], we define the generalized Carter constant as $\mathcal{Q} = \mathcal{K} - (L - aE)^2$, the explicit expression is

$$\mathcal{Q} = p_\theta^2 - \cos^2\theta(a^2\omega_0^2 - L^2\csc^2\theta) + f_\theta(\theta). \tag{99}$$

Note that, if $f_\theta(\theta)$ is a nonnegative function, we have $\mathcal{Q} - f_\theta(\theta) \geq 0$ for any photon passing through the equatorial plane since $\mathcal{Q} - f_\theta(\theta) = p_\theta^2 \geq 0$ when $\theta = \pi/2$. It is convenient to introduce the following rescaled quantities and functions,

$$\hat{\lambda} = \frac{L}{\omega_0}, \qquad \hat{q} = \frac{\sqrt{\mathcal{Q}}}{\omega_0}, \qquad \hat{f}_r = \frac{f_r}{\omega_0^2}, \qquad \hat{f}_\theta = \frac{f_\theta}{\omega_0^2}. \tag{100}$$

In the vacuum case, the trajectory of a photon is independent of its frequency and may be described only by the rescaled quantities $\hat{\lambda}$ and $\hat{q}$ [37]. In the presence of a plasma, however, the photon trajectory does depend on the photon frequency and should be described also with an additional variable ω_0 (since the functions f_r and f_θ are not variables of photons). This can be seen from the trajectory equations (101).

Provided that the surrounding plasma satisfy the separation condition (97), one can obtain the equation of motion for photons by using the H-J method, as follows,

$$\fint^r \frac{dr}{\pm\sqrt{\mathcal{R}(r)}} = \fint^\theta \frac{d\theta}{\pm\sqrt{\Theta(\theta)}}, \tag{101a}$$

$$\Delta\phi = \fint^r \frac{a(2Mr - a\hat{\lambda})}{\pm\Delta\sqrt{\mathcal{R}(r)}} dr + \fint^\theta \frac{\hat{\lambda}\csc^2\theta}{\pm\sqrt{\Theta(\theta)}} d\theta, \tag{101b}$$

$$\Delta t = \fint^r \left[r^4 + a^2(r^2 + 2Mr) - 2aMr\hat{\lambda}\right] \frac{dr}{\pm\Delta\sqrt{\mathcal{R}(r)}} + \fint^\theta \frac{a^2\cos^2\theta}{\pm\sqrt{\Theta(\theta)}} d\theta, \tag{101c}$$

where

$$\mathcal{R}(r) = \mathcal{R}_{\text{vac}}(r) - \Delta\hat{f}_r(r), \tag{102}$$

$$\Theta(\theta) = \Theta_{\text{vac}}(\theta) - \hat{f}_\theta(\theta), \tag{103}$$

with

$$\mathcal{R}_{\text{vac}}(r) = \left(r^2 + a^2 - a\hat{\lambda}\right)^2 - \Delta\left[\hat{q}^2 + \left(a - \hat{\lambda}\right)^2\right], \tag{104}$$

$$\Theta_{\text{vac}}(\theta) = \hat{q}^2 + a^2\cos^2\theta - \hat{\lambda}^2\cot^2\theta. \tag{105}$$

The functions $\mathcal{R}(r)$ and $\Theta(\theta)$ are the radial and angular potentionals in a plasma, respectively, while the functions $\mathcal{R}_{\text{vac}}(r)$ and $\Theta_{\text{vac}}(\theta)$ are the corresponding potentials in the vacuum case, respectively. Note that the trajectory equations have the same formulas as those in the vacuum case but the corrections are implied in these potentials. The integrals in these equations are to be evaluated as path integrals along each trajectory, thus, we use slash notations to distinguish these with ordinary integrals. The plus/minus sign in these equations are chosen to be the same as those of the corresponding directions of photon propagation (sign of dr or $d\theta$). The direction is changed every time when the light ray meets a turning point where either $\mathcal{R}(r)$ or $\Theta(\theta)$ vanishes.

To summarize, the plasma contributes an additional term to the Hamiltonian of a photon, which makes the H-J equation non-separable in general. By assuming that the plasma frequency satisfies the separation condition (97), the equation of motion for photons can be obtained and the influence of a plasma appears only from the radial potential $\mathcal{R}(r)$ and angular potential $\Theta(\theta)$.

3.2.2 *Plasma models*

As the black hole is stationary and axisymmetric, we will consider several specific distributions for the surrounding plasma which depend only on r and θ. The simplest and well-studied model is the radial power-law density [98] which depends only on r and satisfies

$$\omega_p(r)^2 = \frac{4\pi e^2 N_e(r)}{m_e}, \qquad N_e(r) = \frac{N_0}{r^h}, \tag{106}$$

where N_0 is a constant and $h \geq 0$. Unfortunately, this does not satisfy the separation condition (97), thus the above mentioned procedure for obtaining photon motion can not be applied. Nevertheless, we may assume the plasma density has an additional θ dependence such that the separation condition is satisfied, and we make a choice for $f_r(r)$ and $f_\theta(\theta)$ in Eq. (97) as [107]

$$f_r(r) = Cr^k, \qquad f_\theta(\theta) \geq 0, \tag{107}$$

where $C > 0$ and $0 \leq k \leq 2$. Since the plasma density is supposed to be negligible at infinity, we are going to consider two models with $k = 0$ and $k = 1$.

Model 1: A plasma density with $f_r(r) = 0$, $f_\theta(\theta) = \omega_c^2 M^2$ [or equivalently $f_r(r) = \omega_c^2 M^2$, $f_\theta(\theta) = 0$] such that $\omega_p^2 \sim \frac{1}{r^2}$ at large r,

$$\omega_p(r,\theta)^2 = \frac{\omega_c^2 M^2}{r^2 + a^2 \sin^2\theta}. \tag{108}$$

Model 2: A plasma density with $f_r(r) = \omega_c^2 M r$, $f_\theta(\theta) = 0$ such that $\omega_p^2 \sim \frac{1}{r}$ at large r,

$$\omega_p(r,\theta)^2 = \frac{\omega_c^2 M r}{r^2 + a^2 \sin^2\theta}. \tag{109}$$

We have introduced a constant ω_c in these models. For later reference, we will also introduce a rescaled constant, $\hat{\omega}_c = \omega_c/\omega_0$. We name the plasma distributions with the form of Eqs. (97) and (107) the power-law-like models for the reason that the distributions are approximately the same as the power-law models at large r.

Since we are interested in the optical appearance of a black hole, we may expect the existence of a light ray anywhere in the outside of the black hole. As mentioned following Eq. (100), light propagation in a plasma does depend on the photon frequency ω_0. The condition (96) gives a constraint between the plasma frequency ω_p and the photon frequency ω_0 [107],

$$\omega_p(r,\theta)^2 \leq \omega(r,\theta)^2 = -g_{tt}(r,\theta)^{-1}\omega_0^2, \tag{110}$$

where

$$g_{tt} = 1 - \frac{2Mr}{r^2 + a^2 \sin^2\theta}. \tag{111}$$

As we have already seen from the Eqs. (101), in the presence of a plasma, the relevant quantity to describe a photon trajectory (and thus the observables) is the ratio of plasma frequency and photon frequency which can be represented by the ratio $\hat{\omega}_c$ for these two models. Note that this ratio may reflect two kinds of different physics. On the one hand, if we consider the photons only with a given frequency, different ratios represent different case studies of plasmas with different densities. On the other hand, for a given plasma distribution, different ratios represent the chromatic effect of the plasma. Later we will study the dependence of the optical appearance on the ratio $\hat{\omega}_c$.

For the models (108) and (109), we always have $\omega_p < \omega_c$. Therefore, the photon trajectory is similar as it would propagate in vacuum spacetime if $\hat{\omega}_c \ll 1$ [as from Eq. (95) the refraction index $n \to 1$]. However, if $\hat{\omega}_c \gg 1$, it is even impossible for a photon to propagate in the plasma.

Even though the plasma models discussed here are highly idealized, it is possible to extract some approximate effects of a real plasma by using these toy models. Therefore, we will assume the plasma density satisfies the separation condition (97) and mostly focus on the power-law-like models throughout the rest of this chapter. For convenience, later we will also use the subscripts s and o to represent the source of photons and the observer, respectively.

3.3 SHADOW OF AN EXTREMAL KERR BLACK HOLE IN A PLASMA

In Ref. [107], the Kerr shadow in a plasma has been analytically calculated by using the celestial angles [42] which is appropriate for any position of the observer. Moreover, it is also firstly shown in [107] that the analytical approach based on solving the trajectory equations is possible only for a plasma distribution with the form of (97)[1] (as was reviewed in Sec. 3.2). In addition, the shadow also has been numerically performed in Ref. [109]. The numerical approach is, in principle, possible for any distribution of plasma (for example, the power-law form and exponential form have been discussed in [109]).

Here, we revisit the shadow for a Kerr black hole in the presence of a plasma by using the screen coordinates [37] (also refer to as impact parameters in literature) which is appropriate for observers at large distances. In particular, we will study the extremal limit of the shadow and take care of

1 Previously, Atamurotov et al. [105] have analytically calculated the shadow of a Kerr black hole in a plasma but without taking into consideration the separation condition.

the photons in the near-horizon region, whose images are supposed to appear on a vertical line in the vacuum case, the so-called NHEKline [5]. In Sec. 3.4, we will further study the image of an orbiting emitter (hot spot) in this near-horizon region to seek for more signals related to astronomical observations.

The edge of a shadow corresponds to unstable spherical photon orbits around a black hole. For spherical photon orbits we have

$$\mathcal{R}(r) = \mathcal{R}'(r) = 0, \tag{112}$$

where prime denotes derivative with respect to r. Solving these equations, we have

$$\hat{\lambda} = -\frac{M(a^2 - r^2) + \Delta r\sqrt{1-\delta}}{a(r-M)}, \tag{113a}$$

$$\hat{q} = \frac{r^{3/2}}{a(r-M)}\Big[2M\Delta\Big(1+\sqrt{1-\delta}\Big) - r(r-M)^2 + (r-2M)\Delta\delta - \frac{a^2(r-M)^2}{r^3}\hat{f}_r(r)\Big]^{1/2}, \tag{113b}$$

where we have introduced

$$\delta = \frac{r-M}{2r^2}\hat{f}_r'(r). \tag{114}$$

Note that in the near-horizon limit $r \to M$, we have $\delta \to 0$. As discussed below Eq. (99), photon orbits crossing the equatorial plane satisfy

$$\hat{q}^2 - \hat{f}_\theta(\theta) \geq 0. \tag{115}$$

Plugging Eqs. (113b) into Eq. (115) gives a region of spacetime filled with such spherical photon orbits.

We use the screen coordinates (α, β) [Eq. (52)] to describe the image on the sky. The edge of a black hole shadow is given by the curve (α, β) with Eq. (113) for $\hat{\lambda}$ and $\hat{q}$ being plugged in, as

$$\alpha(r) = -\frac{\hat{\lambda}(r)}{\sin\theta_o}, \tag{116a}$$

$$\beta(r) = \pm\sqrt{\hat{q}(r)^2 + a^2\cos^2\theta_o - \hat{\lambda}(r)^2\cot^2\theta_o - \hat{f}_\theta(\theta_o)} = \pm\sqrt{\Theta(\theta_o)}. \tag{116b}$$

The parameter r ranges over the *photon region* where unstable spherical photon orbits exist. The photon region is determined by the Eq. (115) (spherical) and $\Theta(\theta_o) \geq 0$ (i.e., β is real such that the photons can reach to a distant observer thus the orbits are unstable).

3.3.1 *Extremal limit and NHEKline*

Now we consider the extremal limit following the procedure of Ref. [5]. Letting $a \to M$ in Eqs. (113), we have

$$M\hat{\lambda} = M^2 + Mr(1+\sqrt{1-\delta}) - r^2 M\sqrt{1-\delta}, \tag{117a}$$

$$M\hat{q} = \left[r^3\Big(2M(1+\sqrt{1-\delta}) - r + (r-2M)\delta\Big) - M^2\hat{f}_r(r)\right]^{1/2}. \tag{117b}$$

Then the condition (115) on the radius r is expressed explicitly as

$$\frac{r^3}{M^2}\left[2M(1+\sqrt{1-\delta}) - r + (r-2M)\delta\right] \geq \hat{f}_r(r) + \hat{f}_\theta(\theta) \tag{118}$$

The shadow edge is then obtained by plugging Eqs. (117) into Eqs. (52), as follows

$$\alpha = -\left[M + r(1+\sqrt{1-\delta}) - \frac{r^2}{M}\sqrt{1-\delta}\right]\csc\theta_o, \tag{119a}$$

$$\begin{aligned}\beta = \pm\Bigg[&\frac{r^3}{M^2}\Big(2M(1+\sqrt{1-\delta}) - r + (r-2M)\delta\Big)\\ &+(M^2-\alpha^2)\cos^2\theta_o - \hat{f}_\theta(\theta_o) - \hat{f}_r(r)\Bigg]^{1/2}.\end{aligned} \tag{119b}$$

For different choices of a plasma model and an inclination θ_o of the observer, the curves given by Eqs. (119) may either be closed or open. In case of an open curve, there are two endpoints correspond to $r = M$, (i.e., photons originate from the event horizon). For a radial power-law-like plasma with

$$f_r(r) = M^{2-k}\omega_c^2 r^k, (0 \leq k \leq 2), \quad f_\theta(\theta) = 0, \tag{120}$$

the endpoints are at [plugging $r = M$ into Eqs. (119)],

$$\alpha_{\text{end}} = -2M \csc\theta_o, \tag{121a}$$

$$\beta_{\text{end}} = \pm M\sqrt{3 + \cos^2\theta_o - 4\cot^2\theta_o - \hat{\omega}_c^2}. \tag{121b}$$

These endpoints exist provided that β_{end} is real, which gives a critical inclination for the observer, $\theta_{\text{crit}} < \theta_o < \pi - \theta_{\text{crit}}$, where

$$\theta_{\text{crit}} = \arctan\sqrt{\frac{8 - \hat{\omega}_c^2 - \sqrt{(12 - \hat{\omega}_c^2)(4 - \hat{\omega}_c^2)}}{\sqrt{(12 - \hat{\omega}_c^2)(4 - \hat{\omega}_c^2)} - 6 + \hat{\omega}_c^2}}. \tag{122}$$

Note that there are no endpoint at all for $\hat{\omega}_c > \sqrt{3}$ and in that case the given curve is closed. Note also that a real β_{end} also requires that

$$\hat{\omega}_c \leq \hat{\omega}_{\text{crit}} = \sqrt{3 + \cos^2\theta_o - 4\cot^2\theta_o}. \tag{123}$$

Later we will consider that the observer is located at a nearly edge-on inclination, $\theta_o = 84.27°$ (corresponding to $\hat{\omega}_{\text{crit}} \approx \sqrt{2.97}$), thus, for this observer the endpoints exist provided that $\hat{\omega}_c \lesssim \sqrt{2.97}$. For later reference, we refer to the plasma with $\hat{\omega}_c \lesssim \sqrt{2.97}$ as "low density" plasma, otherwise as "high density" plasma.

Since the edge of a shadow does close for all $a < M$, such an open curve has missed an important piece originating from the near-horizon sources. To recover the missing part, we consider the extremal limit again by introducing

$$a = M\sqrt{1 - \kappa^2}, \qquad r = M(1 + \kappa R), \tag{124}$$

where κ is a small parameter. Then for photons orbits which cross the near-horizon region, Eqs. (113) give

$$\hat{\lambda} = 2M + \mathcal{O}(\kappa), \quad \hat{q} = \sqrt{M^2(3 - \frac{4}{R}) - \hat{f}_r^{(0)}(r)} + \mathcal{O}(\kappa), \tag{125}$$

where $\hat{f}_r^{(0)}(r)$ represents the leading order term in κ. Note that the plasma has no influence on $\hat{\lambda}$ in this limit. For the radial power-law-like plasma with (120), we have

$$\hat{\lambda} = 2M + \mathcal{O}(\kappa), \quad \hat{q} = M\sqrt{(3 - \hat{\omega}_c^2) - \frac{4}{R^2}} + \mathcal{O}(\kappa). \tag{126}$$

Then the other piece of shadow edge (originate from near-horizon region) is traced by

$$\alpha(R) = -2M \csc\theta_o + \mathcal{O}(\kappa), \tag{127a}$$

$$\beta(R) = \pm M\sqrt{3 + \cos^2\theta_o - 4\cot^2\theta_o - \hat{\omega}_c^2 - \frac{4}{R^2}} + \mathcal{O}(\kappa). \tag{127b}$$

From the condition (115) and the requirement $\beta \in \mathbb{R}$, we can get the allowed range of R, as

$$R \in \Big[\frac{2}{\sqrt{3 + \cos^2\theta_o - 4\cot^2\theta_o - \hat{\omega}_c^2}}, \infty\Big) + \mathcal{O}(\kappa). \tag{128}$$

As $\kappa \to 0$ and in the allowed range of R, we have

$$\alpha = -2M \csc\theta_{\theta_o}, \tag{129a}$$

$$|\beta| < M\sqrt{3 + \cos^2\theta_o - 4\cot^2\theta_o - \hat{\omega}_c^2}. \tag{129b}$$

This gives precisely the missing part of an open curve, which is the generalized NHEKline [5] in the presence of a plasma. Note that since both of the plasma models (108) and (109) have the form of (120), this NHEKline [Eq. (129)] is applicable for both of them and is exactly the same for each particular value of $\hat{\omega}_c$. However, curves given by Eq. (119) for these models are different.

To summarize, for an observer at $\theta_o = 84.27°$, the shadow is given either by Eq. (119) for $\hat{\omega}_c > \sqrt{2.97}$ or by the union of Eqs. (119) and (129) for $0 \le \hat{\omega}_c \lesssim \sqrt{2.97}$. Note that any near-horizon source in a plasma having the above mentioned models with $\hat{\omega}_c > \sqrt{2.97}$ can not be seen by this observer. We will show these with figures and discuss them in detail in subsection 3.3.2.

3.3.2 *Silhouette of black hole*

We now show the silhouette of a black hole shadow observed at $\theta_o = 84.27°$ for the two specific plasma models (108) and (109) in Fig. 11. For model 1, $\omega_p^2 = \omega_c^2 M^2/(r^2 + a^2\cos^2\theta)$, we choose $f_r = \omega_c^2 M^2$ and $f_\theta = 0$ (or equivalently, $f_r = 0$ and $f_\theta = \omega_c^2 M^2$); for model 2, $\omega_p^2 = \omega_c^2 Mr/(r^2 + a^2\cos^2\theta)$, we choose $f_r = \omega_c^2 Mr$ and $f_\theta = 0$. The silhouettes are obtained by plugging these specific functions $\hat{f}_r$ and $\hat{f}_\theta$ into Eq. (119) [and Eq. (129)] over the allowed range of r for each given value of $\hat{\omega}_c$. This allowed range can be found numerically from the inequality (118).

These exhibit the following dependencies of the shadows on the plasma model and on the value of $\hat{\omega}_c$. Each of the shadow edges for a "low density" plasma has a vertical part while that for a "high density" plasma does not. The shadows shrink in both model 1 and model 2 when $\hat{\omega}_c$ is increased. Moreover, at a given value of $\hat{\omega}_c$, the shadow shrinks more in model 2 than in model 1. This is because the model 2 has a larger plasma density at a given distance r since the density scales like $1/r$ while in model 1 it scales like $1/r^2$. Furthermore, in both model 1 and 2, photons in the near-horizon region have contributions to the shadows only for $\hat{\omega}_c < \sqrt{2.97}$ (which gives the NHEKlines). At each same value of $\hat{\omega}_c$, the NHEKlines for these two models are the same. When $\hat{\omega}_c$ goes from 0 to $\sqrt{2.97}$, the NHEKline appears at the same coordinate of α while the maximum absolute value of β decreases.

Note that the plasma distributions of example 2 and example 3 in Ref. [107] also have the power-law-like form (107) with $\omega_p^2 \sim r^{-2}$ and $r^{-3/2}$, respectively. The results in [107] are exhibited with figures for an observer at $r_o = 5M$ and $\theta_o = \pi/2$ and for spin $a = 0.999M$. While our models 1 and 2 have $\omega_p^2 \sim r^{-2}$ and r^{-1}, respectively, and the results are obtained for $a \to M$, $r_o \to \infty$ and $\theta_o = 84.27°$. We find a good agreement between our results and those in [107] on the general features discussed above (except details of the NHEKlines since these have not been discussed in [107]). Moreover, the critical ratios for the photon regions are also quantitatively comparable among these results up to factors in these plasma models and the approximations of observers' locations and black hole spins. Furthermore, these features for the power-law-like plasma models also qualitatively agree with those for the power-law models [with the form of (106)] which have been numerically performed in [109] for $\omega_p^2 \propto r^{-1}$, r^{-2} and r^{-3}. Therefore, even through the separation condition (97) has been proposed based on a mathematical motivation [107], it is nevertheless physically effective.

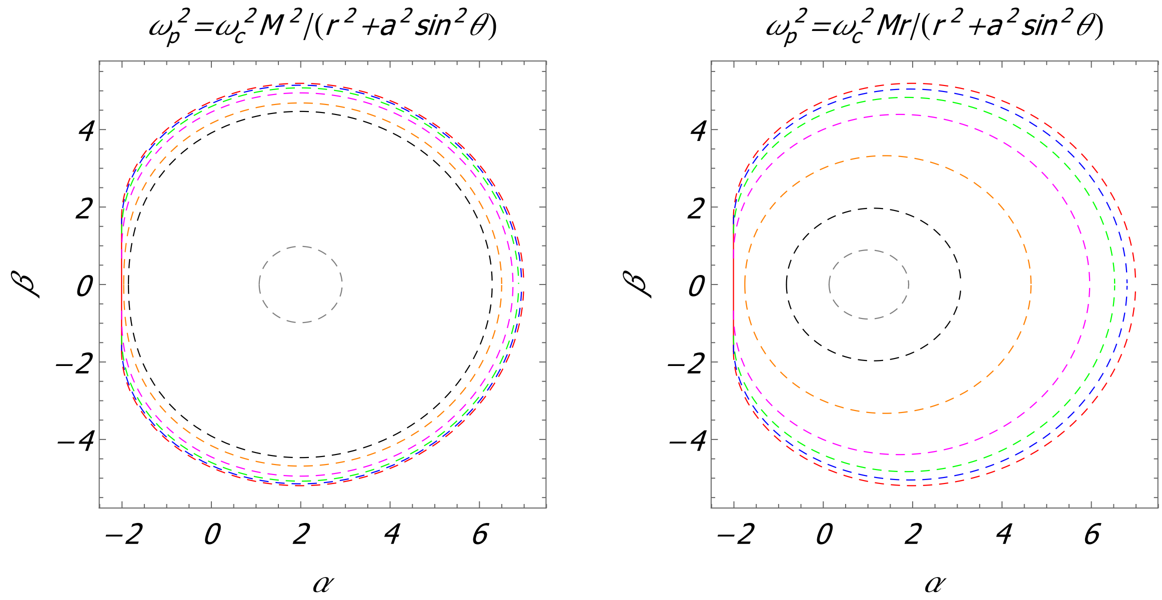

Figure 11.: Shadow edge of an extremal Kerr black in the presence of a plasma for model 1 (left) and model 2 (right), respectively, seen from an inclination of $\theta_o = 84.27°$. For model 1, we have $\omega_p^2 = \omega_c^2 M^2/(r^2 + a^2\cos^2\theta)$; for model 2, we have $\omega_p^2 = \omega_c^2 Mr/(r^2 + a^2\cos^2\theta)$. The photon regions for a spherical orbit crossing the equatorial plane vanish at $\hat{\omega}_c^2 \approx 27$ for model 1 and at $\hat{\omega}_c^2 \approx 8$ for model 2. For both models, we have $\hat{\omega}_c^2 = \omega_c^2/\omega_0^2 = 0$ (red), 0.5 (blue), 1.2 (green), 2.5 (magenta), 5 (orange) and 7 (black). In addition, the gray curves have $\hat{\omega}_c^2 = 26$ (left) and 7.8 (right). The dashed lines are given by Eq. (119) and the solid vertical lines are given by Eq. (129). Note that for $\hat{\omega}_c^2 = 0.5, 1.2$ and 2.5, the NHEKlines are overlapped with the red solid lines but have shorter lengths which begin and end at the endpoints of the corresponding dashed lines.

3.4 ORBITING EMITTER IN A PLASMA

Now we consider an isotropic point emitter (hot spot) orbiting on a circular and equatorial geodesic at radius r_s around a Kerr black hole in the presence of a plasma. This point emitter is supposed to be much heavier than the plasma, thus, we may neglect the influence of the plasma on the motion of this emitter. The angular velocity for such an emitter is given by [83] (same as in vacuum Kerr spacetime)

$$\Omega_s = \pm \frac{M^{1/2}}{r_s^{3/2} \pm aM^{1/2}}, \tag{130}$$

and the innermost stable circular orbit (ISCO) is given by

$$r_{\text{ISCO}} = M\Big[3 + Z_2 - \sqrt{(3 - Z_1)(3 + Z_1 + 2Z_2)}\Big], \tag{131}$$

where

$$Z_1 = 1 + (1 - a_\star^2)^{1/3}\big[(1 + a_\star)^{1/3} + (1 - a_\star)^{1/3}\big], \quad Z_2 = \sqrt{3a_\star^2 + Z_1^2}, \quad a_\star = \frac{a}{M}. \tag{132}$$

3.4.1 *Lens equations*

The orbiting emitter at $(t_s, r_s, \theta_s, \phi_s)$ is connected to an observer at $(t_o, r_o, \theta_o, \phi_o)$ by photon trajectories described by Eqs. (101). In these equations, the lower and upper bounds for the radial integrals are chosen as r_s and r_o, respectively, while the lower and upper bounds for the angular integrals are chosen as θ_s and θ_o, respectively. In addition, we have $\Delta\phi = \phi_o - \phi_s$ and $\Delta t = t_o - t_s$. Using the relation $\phi_s = \Omega_s t_s$, we have

$$\Delta\phi - \Omega_s \Delta t = \phi_o - \Omega_s t_o, \tag{133}$$

then the unknowns ϕ_s and t_s can be decoupled from the Eqs. (101b) and (101c).

Following Ref. [5], we rearrange these Eqs. (101) as the Kerr lens equations in the presence of a plasma. First, we introduce parameters $b \in \{0, 1\}$, $m \in \mathbb{Z}^{\geq 0}$ to denote the number of radial and angular turning points, respectively, and $s \in \{-1, 1\}$ to denote the final orientation of p_θ. Then we set $\phi_o = 2\pi N$ with $N \in \mathbb{Z}$ recording the net winding number executed by the photon relative to the emitting source between its emission time and reception time. Finally, the lens equations can be written as

$$I_r + b\tilde{I}_r = G_\theta^{m,s}, \tag{134a}$$

$$J_r + b\tilde{J}_r + \frac{\hat{\lambda} G_\phi^{m,s} - \Omega_s a^2 G_t^{m,s}}{M} = -\Omega_s t_o + 2\pi N, \tag{134b}$$

where I_r, $\tilde{I}_r$, J_r and $\tilde{J}_r$ are radial integrals defined in appendix A and $G_i^{m,s}$ ($i \in \{t, \theta, \phi\}$) are angular integrals defined in appendix B. These equations have the same formulae as those in vacuum Kerr spacetime, however, the differences are implied in the integrals. Solving these lens equations for given parameters m, s, b and given values of r_s and θ_o, we can write the conserved quantities $\hat{\lambda}$ and $\hat{q}$ in terms of t_o which label the photon trajectories connecting the source to an observer.

3.4.2 *Near-extremal solutions*

We assume the emitter is on, or near, the direct ISCO of a near-extremal Kerr black hole. It is convenient to introduce a dimensionless radial coordinate R which is defined through the Boyer-Lindquist radius r by

$$R = \frac{r - M}{M}. \tag{135}$$

We also introduce a small parameter $\epsilon \ll 1$ to describe the condition for the near-extremality of a black hole, as follows,

$$a = M\sqrt{1 - \epsilon^3}. \tag{136}$$

Under this condition, the ISCO [Eq. (131)] is located away from the event horizon a coordinate distance $\sim \epsilon$,

$$R_{\text{ISCO}} = 2^{1/3}\epsilon + \mathcal{O}(\epsilon^2), \tag{137}$$

thus, the radial coordinate for the emitter can be written as

$$r_s = M(1+\epsilon\bar{R}) + \mathcal{O}(\epsilon^2), \qquad \bar{R} \geq 2^{1/3}, \tag{138}$$

which means that the emitter is in the near-horizon region. Even though the motion of this emitter is not affected by the plasma, its image can only possibly be seen if the plasma density has $\hat{\omega}_c \lesssim \sqrt{3}$ as the light rays are refracted by the plasma, and in that case the image appears on the NHEKline (see discussions in Sec. 3.5.1).

Following Ref. [4, 5], we introduce new quantities λ and q instead of using $\hat{\lambda}$ and $\hat{q}$

$$\hat{\lambda} = 2M(1+\epsilon\lambda), \qquad \hat{q} = M\sqrt{3-q^2}. \tag{139}$$

As mentioned below Eq. (99), we have $Q - f_\theta(\theta) \geq 0$ for those photons emitted from equatorial plane. Thus, we have

$$q^2 \leq 3 - \frac{\hat{f}_\theta(\theta)}{M^2}. \tag{140}$$

In the equatorial plane, motion of photons has $q = \sqrt{3 - \hat{f}_\theta(\theta)/M^2}$. We will show in Sec. 3.4.2.3 that a light ray originating from this emitter to an observer at far region must also have lower bounds on q^2 and thus we can always have a positive q. Together with the upper bound (140), we can get the range for a specific plasma model. For the model 1 [Eq. (108)], we may either choose $f_r(r) = 0$ and $f_\theta(\theta) = \omega_c^2 M^2$, then we have

$$0 < q^2 \leq 3 - \hat{\omega}_c^2\ ; \tag{141}$$

or choose $f_r(r) = \omega_c^2 M^2$ and $f_\theta(\theta) = 0$, then we have

$$\hat{\omega}_c^2 < q^2 \leq 3. \tag{142}$$

Note that the range of q may depend on the choice of f_r and f_θ, however, the quantity $\hat{q}^2 - \hat{f}_\theta$ remains unchanged in any case. For the model 2 [Eq. (109)], we choose $f_r(r) = \omega_c^2 Mr$ and $f_\theta(\theta) = 0$, then we have

$$(5\hat{\omega}_c^2 - \hat{\omega}_c^4)/4 < q^2 \leq 3, \qquad q^2 > \hat{\omega}_c^2. \tag{143}$$

Plugging the expressions (136), (138) and (139) into the lens equations (134) gives the near-extremal lens equations. Then for given values of r_s and θ_o, we solve these equations to the subleading order in ϵ for the plasmas with distributions (108) and (109), respectively, following the procedure of Ref. [5].

Note that even though we have considered a near-extremal black hole with the condition (136), it turns out that the results are identical to the subleading order in ϵ if we considered an extremal black hole with $a = M$ (same as in the vacuum case [5]).

3.4.2.1 *Model 1:* $\omega_p^2 = \omega_c^2 M^2/(r^2 + a^2 \sin^2\theta)$

We choose $f_r(r) = 0$ and $f_\theta(\theta) = \omega_c^2 M^2$. In this case, the radial potential is the same as that in the vacuum Kerr case [5], thus, we have the same radial integrals and then we obtain the same formulae of solutions for the lens equations up to corrections in the angular integrals. These angular integrals are performed in App. B.

First, we make a choice of the parameters b, m and s. Then, from the first equation (245a) we can obtain the condition for the existence of a solution,

$$\bar{R} < \frac{4\Upsilon}{q^2}\left(1 + \frac{2}{\sqrt{4-q^2}}\right) \quad \text{if} \quad b = 0, \tag{144a}$$

$$\bar{R} > \frac{4\Upsilon}{q^2}\left(1 + \frac{2}{\sqrt{4-q^2}}\right) \quad \text{if} \quad b = 1, \tag{144b}$$

and the solution, as follows,

$$\lambda = \frac{2\Upsilon}{4-q^2}\left[2 - q\sqrt{1 + \frac{4-q^2}{2\Upsilon}\bar{R}}\right]. \tag{145}$$

Here, $\Upsilon > 0$ is defined by

$$\Upsilon \equiv \frac{q^4 R_o}{q^2 + 2R_o + qD_o} e^{-qG_\theta^{\bar{m},s}}, \tag{146}$$

where

$$D_o = \sqrt{q^2 + 4R_o + R_o^2}, \tag{147}$$

and $G_\theta^{\bar{m},s}$ is defined in Eq. (307), with

$$\bar{m} = m + \frac{1}{qG_\theta} \log \epsilon. \tag{148}$$

Next, regarding the second equation (245b), we introduce a dimensionless time coordinate $\hat{t}_o$ which is restricted to unit period of the emitter,

$$\hat{t}_o = \frac{t_o}{T_s} = \frac{\Omega_s t_o}{2\pi} = \frac{t_o}{4\pi M} + \mathcal{O}(\epsilon). \tag{149}$$

Thus, the second equation can be written in terms of this dimensionless time coordinate, as

$$\hat{t}_o = N - \frac{1}{2\pi}\left(J_r + b\tilde{J}_r + 2G_\phi^{m,s} - \frac{1}{2}G_t^{m,s}\right), \tag{150}$$

where J integrals and G integrals are given in Appendices. A and B.

Note that we have already obtained a function $\lambda(q)$ [Eq. (263)] in the allowed range of q [Eq. (144)] from the first equation, the second then gives a function $\hat{t}_o(q)$. Inverting this function in each monotonic domain gives a function $q_i(\hat{t}_o)$ for a given choice of integer N. Here we have introduced a discrete integer i to label the monotonic parts of $\hat{t}_o(q)$ in each of the allowed ranges of q. Since the observational quantities can be expressed in terms of the conserved quantities λ and q, each $q_i(\hat{t}_o)$ corresponds to a specific track segment of the emitter's image which can be labeled by (m, b, s, N, i).

3.4.2.2 *Model 2:* $\omega_p^2 = \omega_c^2 Mr/(r^2 + a^2 \sin^2\theta)$

We choose $f_r(r) = \omega_c^2 Mr$ and $f_\theta(\theta) = 0$. Since the lens equations for this case are similar as those for model 1 (see Sec. 3.4.2.3 for details), we can find the solutions in a similar way for a given choice of parameters b, m and N. For convenience, we introduce a new parameter $\tilde{q} = \sqrt{q^2 - \hat{\omega}_c^2}$.

The solution of the first equation (245a) and the condition of its existence are given by replacing q with $\tilde{q}$ in the formulas (263) and (144), respectively, where the expression of Υ is corrected as

$$\Upsilon \equiv \frac{\tilde{q}^4 R_o}{\tilde{q}^2 + (2 - \frac{\hat{\omega}_c^2}{2})R_o + \tilde{q}D_o} e^{-\tilde{q}G_\theta^{\bar{m},s}}, \tag{151}$$

with

$$D_o = \sqrt{\tilde{q}^2 + (4 - \hat{\omega}_c^2)R_o + R_o^2}, \tag{152}$$

and $G_\theta^{\bar{m},s}$ is given in Eq. (307) with $\bar{m} = m + \log\epsilon/(\tilde{q}G_\theta)$.

The second equation (245b) can also be rewritten in a form as (150), however, the J integrals and G integrals therein are different from those for model 1 (see Appendices A and B).

Similarly, we can also obtain the image track segment $q_i(\hat{t}_o)$ of the emitter labeled by (m, b, s, N, i).

3.4.2.3 *Lens equations for two plasma models*

In Sec. 3.4.2, we have solved the lens equations for the power-law-like plasma models 1 and 2 [Eqs. (108) and (109)] by choosing $f_r(r) = 0$, $f_\theta(\theta) = \omega_c^2 M^2$ for model 1 and $f_r(r) = \omega_c^2 M r$, $f_\theta(\theta) = 0$ for model 2. In order to compare the len equations for these two models, we may equivalently choose $f_r(r) = \omega_c^2 M^2$, $f_\theta(\theta) = 0$ for model 1 instead. Thus, the difference of the lens equations between these two models are only imposed in the radial integrals with the function $f_r(r)$ taken the form of $f_r(r) = M^{2-k}\omega_c^2 r^k$. Next we expand the radial potential (102) for $f_r(r) = M^{2-k}\omega_c^2 r^k$ $(0 \leq k \leq 2)$ in the near-horizon region and in the far region, respectively. Then we have

$$\mathcal{R}_n(R \sim \epsilon) = M^4\epsilon^2\left[(q^2 - \hat{\omega}_c^2)\tilde{R}^2 + 4\lambda(2\tilde{R} + \lambda)\right], \tag{153a}$$

$$\mathcal{R}_f(R \sim 1) = M^4\left[q^2 + 4R + R^2 - (1 - R)^k\hat{\omega}_c^2\right], \tag{153b}$$

where we have introduced $\tilde{R} = R/\epsilon$. At every point along a photon trajectory that originates in the NHEK region and reaches to the far region, one must have nonnegative potential $\mathcal{R}(r) \geq 0$. To guarantee that this condition is hold in the near region, we should take $q^2 > \hat{\omega}_c^2$; to guarantee that this condition is hold in the far region, we should take $q^2 > \hat{\omega}_c^2$ for $k = 0$ or $q^2 > (5\hat{\omega}_c^2 - \hat{\omega}_c^4)/4$ for $k = 1$. Moreover, from the expansions (153) we see that the near-horizon piece of the radial integrals for the two models are exactly the same, while even though the far region piece contains differences among these two models, the plasma densities are very small in that region since they scale like $1/r^h$ (h=2 and 1, respectively).

3.5 OBSERVATIONAL APPEARANCE OF THE ORBITING EMITTER

In the vacuum case, the images of an emitter orbiting on the ISCO of a rapidly rotating black hole appearing on the NHEKline has a rich structure [5]. Next, we will study the influence of plasma on these images.

3.5.1 *Observational quantities*

From the previous section, the photon conserved quantities $q(\hat{t}_o)$ and $\lambda[q(\hat{t}_o)]$ (along trajectories) are obtained for the plasma models (108) and (109). These conserved quantities help to describe the observational appearance of the emitter: the image position, redshift and flux. We have briefly reviewed this for a general black hole (in vacuum) in Sec. 2.6.1 and will give the results for a near-extremal black hole (in a plasma) in the following.

In the near-extremal limit and to the leading order in ϵ, we have (see Sec. 3.4.2)

$$a = M, \qquad r_s = M(1+\epsilon\bar{R}), \tag{154a}$$

$$\hat{\lambda} = 2M(1+\epsilon\lambda), \qquad \hat{q} = M\sqrt{3-q^2}. \tag{154b}$$

Then, the apparent position (52) on the celestial sphere is expanded as

$$\alpha = -2M\csc\theta_o + \mathcal{O}(\epsilon), \tag{155a}$$

$$\beta = sM\Big(3 - q^2 + \cos^2\theta_o - 4\cot^2\theta_o - \frac{\hat{f}_\theta(\theta_o)}{M^2}\Big)^{1/2} + \mathcal{O}(\epsilon), \tag{155b}$$

where s is the final orientation of p_θ. Note that the position does not depend on λ to the leading order and q should be in a range such that β is real. For an observer at $\theta_o = 84.27°$, this range is obtained as $0 \leq q \lesssim \sqrt{2.97 - \hat{f}_\theta(\theta_o)/M^2}$. Combining with another range of q discussed in Sec. 3.4.2, we find that the images of a hot spot in a plasma with models 1 and 2 appear on the NHEKline (see Sec. 3.3.1). The redshift factor is expanded as

$$g = \frac{1}{\sqrt{3} + \frac{4}{\sqrt{3}}\frac{\lambda}{\bar{R}}} + \mathcal{O}(\epsilon). \tag{156}$$

The flux (336) is expanded as

$$\frac{F_o}{F_N} = \frac{\sqrt{3}\epsilon\bar{R}}{2D_s}\frac{qg^3}{\sin\theta_o\sqrt{\Theta_0(\theta_o)}\sqrt{3 - q^2 - \frac{\hat{f}_\theta(\theta_s)}{M^2}}}\left|\det\frac{\partial(B,A)}{\partial(\lambda,q)}\right|^{-1}, \tag{157}$$

where A and B are defined in Eqs. (333), and

$$\Theta_0(\theta_o) = 3 - q^2 + \cos^2\theta_o - 4\cot^2\theta_o - \frac{\hat{f}_\theta(\theta_o)}{M^2}, \tag{158}$$

and

$$D_s = \sqrt{q^2\bar{R}^2 - 8\lambda\bar{R} + 4\lambda^2 - \frac{\hat{f}_r^{(0)}(r_s)}{M^2}\bar{R}^2}, \tag{159}$$

with $\hat{f}_r^{(0)}(r_s)$ being the leading order term of $\hat{f}_r(r_s)$ in ϵ.

Note that these results are obtained for each given choice of discrete parameters m, s, b and N, which corresponds to a specific image track. The full time-dependent image is completed by finding all such tracks for all choices of these parameters. The influences of plasma on these observables are introduced from the functions $\hat{f}_r$ and $\hat{f}_\theta$, as well as from the quantities λ and q which label different photon trajectories.

3.5.2 *Hot spot image*

We now describe the observational quantities of the hot spot's image with figures following the procedure of Ref. [5] and using the open numerical code therein. The image depends on the choice of the plasma distribution and the physical parameters R_o, θ_o, ϵ and $\bar{R}$. We will consider the two plasma models (108) and (109) with several certain values of $\hat{\omega}_c$, respectively. In order to compare the results with those for the vacuum case [5], we make the following choice for these parameters:

$$R_o = 100, \qquad \theta_o = \frac{\pi}{2} - \frac{1}{10} = 84.27^\circ, \tag{160a}$$

$$\epsilon = 0.01, \qquad \bar{R} = \bar{R}_{\text{ISCO}} = 2^{1/3}. \tag{160b}$$

As described in Sec. 3.4.2, for each choice of discrete parameters m, b, s, N and an additional label i, we can obtain an image track segment $q(\hat{t}_o)$ [and $\lambda(\hat{t}_o)$]. The main observables for the segment are given in Eqs. (155), (156) and (157). The completed information of the hot spot image is built up by including all such choices of parameters (in practice, we consider only a few values of m and N since the image for others are vanishingly small) [5]. Below we show the brightest few images for model 1 [Eq. (108)] in Fig. 12 and for model 2 [Eq. (109)] in Fig. 13, respectively. We consider four different values of the ratio $\hat{\omega}_c$ for each of the models and also colour-code continuous image tracks in each of these plots.

Comparing Fig. 12 with Fig. 13, we find that the images of model 1 and model 2 (with a given value of $\hat{\omega}_c$) are very similar. This is because the difference between the lens equations (134) among these two models is negligibly small. Firstly, the lens equations in the near horizon region are the same to the leading order in ϵ for both models. Secondly, even though there are differences appearing in the far region, these have a negligible influence on the image since the plasma densities decrease with r in an inverse power-law behavior [See the results and discussions for plasma distributions with $f_r(r) = M^{2-k}\omega_c^2 r^k$, $(k = 0, 1)$, and $f_\theta(\theta) = 0$ in Sec. 3.4.2.3]. Therefore, here we will only discuss the features exhibited in Fig. 12 for the model 1.

Fig. 12 shows the main observables in a plasma with $\omega_p^2 = \omega_c^2 M^2/(r^2 + a^2 \sin^2\theta)$, where we have taken four different values for $\hat{\omega}_c^2 = \omega_c^2/\omega_0^2$ as 0, 0.5, 1.2 and 2.5. In each case, the green line is for the brightest primary image while others are for the secondary images. Note that the secondary images are, in general, much fainter than the primary image and are important only when

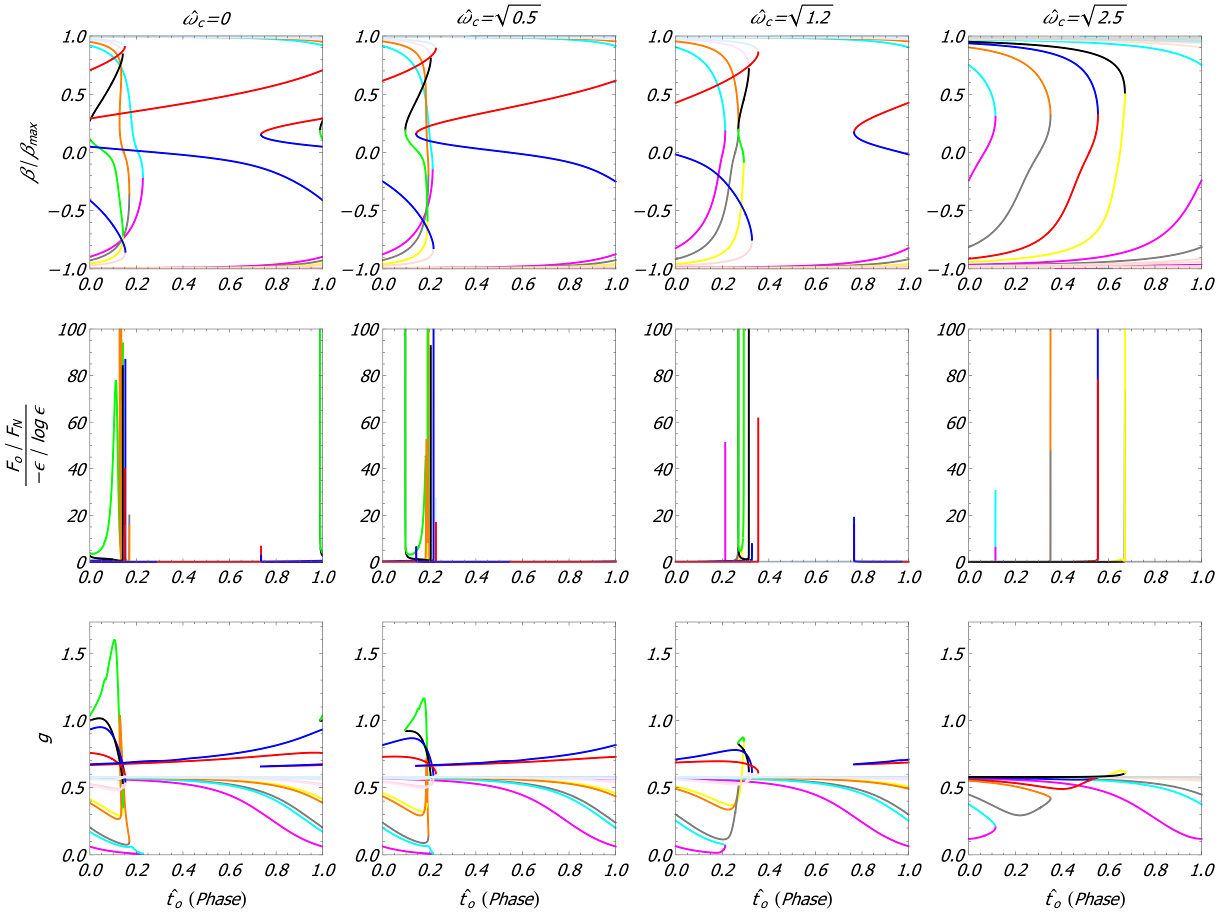

Figure 12.: Positions, fluxes and redshifts of the brightest few images of the hot spot for $\omega_p^2 = \omega_c^2 M^2/(r^2 + a^2\cos^2\theta)$ (model 1). From left to right, we have $\omega_c/\omega_0 = 0$, $\sqrt{0.5}$, $\sqrt{1.2}$ and $\sqrt{2.5}$, respectively. We have color-coded the images in the same way as that of Ref. [5] and each monochromatic line may be composed of several continuous track segments labeled by (m, b, s, N, i).

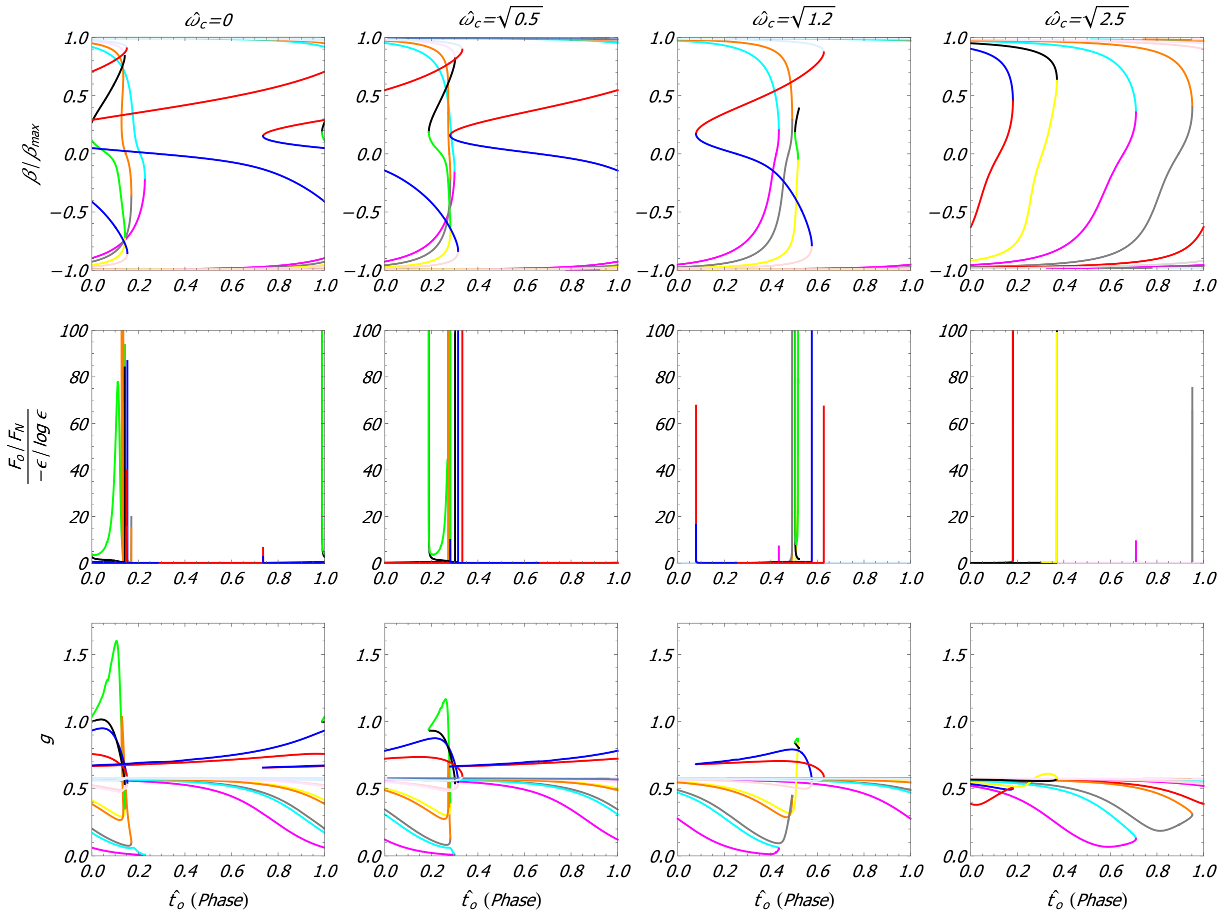

Figure 13.: Positions, fluxes and redshifts of the brightest few images of the hot spot for $\omega_p^2 = \omega_c^2 Mr/(r^2 + a^2\cos^2\theta)$ (model 2). From left to right, we have $\omega_c/\omega_0 = 0$, $\sqrt{0.5}$, $\sqrt{1.2}$ and $\sqrt{2.5}$, respectively. We have color-coded the images in the same way as that of Ref. [5] and each monochromatic line may be composed of several continuous track segments labeled by (m, b, s, N, i).

different image tracks intersect. Therefore, below we will focus on the feature of the primary image. In each of these cases, the primary image (if any) appears near the center of the NHEKline before moving downward while peaking in brightness. The image appears periodically and the period stays unchanged when $\hat{\omega}_c$ is increased. For $\hat{\omega}_c^2 = 0$, this corresponds to the vacuum case and the results are agree with Ref. [5]. For a non-zero plasma, there are remarkable influences on the image position and redshift while smaller influence on the image flux. When $\hat{\omega}_c$ is increased from zero, not only the maximum elevation of the NHEKline (β_{max}) decreases but also the relative portion of the NHEKline on which appears the image (β/β_{max}) decreases, and so do the redshift factor and time duration of the image. Note that for smaller values of $\hat{\omega}_c$ the primary image is blueshifted while for larger ones it becomes redshifted. The primary image vanishes when $\hat{\omega}_c$ is greater than a critical value and the entire images vanish when $\hat{\omega}_c \gtrsim \sqrt{2.97}$.

3.6 SUMMARY AND CONCLUSION

In this chapter, we investigated the observational signature of a high-spin Kerr black hole in the presence of a surrounding plasma. We considered the plasma as a dispersive medium for photons but neglect its gravitational effects. We assumed that the plasma distributions satisfied a separation condition (97) proposed by Perlick and Tsupko [107] such that the photon trajectory could be solved analytically. Then we studied the shadow of the black hole and the signal produced by a nearby hot spot.

To obtain the optical appearance, we first found the equation of motion for photons by solving the H-J equations under the separation condition. We found that the corrections of these equations to the vacuum case were imposed only from the radial potential $\mathcal{R}(r)$ and angular potential $\Theta(\theta)$ [see Eqs. (101)]. We also introduced two special power-law-like models [(108) and (109)] which satisfied the separation condition in Sec. 3.2.2 as simple examples which were studied in detail.

Next, we analytically studied the photon region and shadow of an extremal Kerr black hole surrounded by a plasma. For a power-law-like plasma, the photon region was determined by Eq. (118) and the edge of a shadow was described either by the union of Eqs. (119) and (127) or by Eq. (119) only, depending on whether the near-horizon source was in the photon region ("low" density plasma) or not ("high" density plasma). The size of shadow decreased when the density of plasma was increased and the shape of shadow was different for plasma with "low" or "high" density. Moreover, in case of "low" density plasma, the near-horizon sources all terminated at a vertical line: the NHEKline. We showed these in Fig. 11 and discussed the features in Sec. 3.3.2.

Then we studied the signal produced by a hot spot orbiting at the ISCO of the black hole in the presence of a power-law-like plasma. We solved the lens equations in the near-extremal limit in Sec. 3.4 and obtained analytical formulae for the observational quantities: the image position (155), the image redshift (156) and the image flux (157). Noted that since the ISCO of a high-spin black hole was in the near-horizon region, this signal could only possible be seen in a "low" density plasma. The plasma had a remarkable influence on the brightest image: the segment on the celestial sphere for the image to appear was smaller than that in the vacuum case and so was the redshift. We showed these in Fig. 12 and 13 and discussed the features in Sec. 3.5.2.

In a real astrophysical setup (given the parameters for the black hole and the surrounding plasma), the ratio $\hat{\omega}_c$ depends on the frequency of photon, thus, the observational signatures that we discussed above are all chromatic. Note that the ratio $\hat{\omega}_c$ is greater for a photon with lower frequency, thus, there is a larger influence on the trajectory of such photon. Combining the information of black hole shadow and hot spot signal, we can sketch a picture (template) for what we may see from the EHT.

4

KERR-MOG

4.1 INTRODUCTION

Black holes play an important role both in understanding gravity theories and in explaining astronomical phenomena. There have been abundant observational evidences for black holes in our universe [110, 111, 112]. Inspiringly, we are entering a new era of more precise astronomical observations with the efforts of LIGO, Virgo, eLISA, EHT, BlackHoleCam, ATHENA, SKA et al. Among those, EHT is particularly interesting since it aims at observing the event horizon of a black hole which is its most striking feature. Thus we will be able to observe black holes significantly closer to the event horizon and obtain their images (shadows). Hence there is an urgent need for theoretical templates to identify the images that one expects to observe. This has stimulated recent theoretical works predicting the signals that EHT may possibly observe [113, 114, 115, 116, 117, 5, 55] and examining the type of properties of gravity that the shadows can inform us of [35, 118, 119].

Recently, an analytical method was proposed to compute the observational signature of a near-extremal (high-spin) Kerr black hole [5]. The authors considered an isotropically emitting point source ("hot spot") orbiting near a rapidly spinning Kerr black hole and found that the primary image and secondary images appear on a vertical line segment which constitutes a portion of the black hole shadow. Ref. [5] also discussed the positions, fluxes and redshift factors of these images in detail, which provide a unique signature for identifying a high-spin Kerr black hole.

Even though the Kerr solution predicted by general relativity (GR) is widely expected to describe astrophysical black holes, there are indications both from physics and astrophysics that GR is modified. Therefore, it is important to obtain templates based on different gravitational theories [81, 120, 121, 122, 123, 124, 125, 77]. One of these candidates is the scalar-tensor-vector (STVG) modified gravitational (MOG) theory [77]. The motivation of this theory is to construct a covariant theory of gravity without invoking dark matter, since the hypothesized dark matter has not been observed so far, to release the discrepancies between theoretical predictions of GR and some astronomical observations at the cosmological or galactic scale. For the same motivation, a series of theories has been proposed prior to the MOG theory, namely, the Modified Newtonian Dynamics theory (MOND) [79] and its relativistic extensions (for a review see Ref. [126]). Independently, Moffat proposed the MOG theory by adding a massive vector field to the Einstein-Hilbert action and replacing constants of the ordinary gravity theory by scalar fields [77]. The MOG theory has successfully explained Solar system observations [77], galactic rotation curves [127], dynamics of clusters of galaxies [128] and cosmological data [129]. However, it still remains to be tested in the strong gravity regime [130]. The EHT might hopefully provide such a test.

The static and rotating solutions of MOG were obtained in Ref. [80] and followed by research works examining various aspects of these black holes [131, 44, 132, 133, 134, 130, 135, 136, 137]. The particular case of rotating black holes known as Kerr-MOG (KM) black holes have gained more astrophysical interests since the observed black holes are thought to be rotating. For example, the particle dynamics [135], the innermost stable circle orbit [134], the accretion disks [130] and the relativistic jets [133] have been studied. Furthermore, the shadows cast by MOG black holes have been studied in Ref. [44], in which it was shown that the sizes of these shadows increase significantly as the free modified parameter is increased. However, the shadow is expected to exhibit further signals which need to be clarified, such as its shape and images of orbiting hot spots (if any) on it.

The aim of this chapter is to obtain the shadow cast by a near-extremal KM black hole, following the method of Ref. [5]. Moreover, we will study the images of an isotropically emitting point source orbiting this black hole to explore further signatures. There are two reasons for us to consider the near-extremal case. First, the nice properties that the near-extremal case possess enable us to apply a powerful computational method. Second, a large amount of observed supermassive black holes are thought to be rotating very rapidly [4], which is the near-extremal case at least in Kerr spacetime. The signatures we obtained have the following properties. The sizes of shadows cast by near-extremal KM black holes decrease when the modified parameter is increased. The signals produced by the orbiting hot spot are similar to those produced in a high spin Kerr (the extremal value of the reduced spin J/M^2 is 1) [5]. However, the extremal KM black hole can have a reduced spin with a finite amount below 1 (for the cases we will consider, it ranges from 0.717 to 1) which gives a wider range of possible spin for a near-extremal astrophysical black hole. Furthermore, the observational appearance of the hot spot is also quantitatively different from Kerr. For example, when the modified parameter is increased from zero, the flux increases and the typical redshift factor for the secondary images also increases. These signatures appear periodically with period greater than that of Kerr. The critical allowed inclination for an observer to see this effect also increases in the MOG cases. This provides other possible signatures for the EHT to test.

This chapter is organized as follows. In Sec. 4.2, we present a brief introduction to the MOG theory and KM black hole. In Sec. 4.3, we set up the ray-tracing problem for a general KM black hole and write down the equations to be solved. In Sec. 4.4, we solve the equations in the near-extremal limit to the subleading order in the deviation from extremality. In Sec. 4.5, we compute the shadow of a non-extremal KM black hole and discuss its extremal limit. In Sec. 4.6, we present our results with figures and discuss these in detail. We furthermore compare our results with that of the Kerr black hole. We give a summary in Sec. 4.7.

4.2 MOG THEORY AND KERR-MOG BLACK HOLE

We will restore the Newtonian constant G_N for a while in order to introduce the modified gravity (MOG) theory. The MOG theory is also referred to as the scalar-tensor-vector gravity (STVG), whose action is given by [77]

$$S = S_{\text{Grav}} + S_{\phi} + S_{\text{S}} + S_{\text{M}}, \tag{161}$$

where

$$S_{\text{Grav}} = \frac{1}{16\pi} \int d^4x \sqrt{-g} \frac{1}{G} R, \tag{162}$$

$$S_{\phi} = -\int d^4x \sqrt{-g} \Big[\omega \Big(\frac{1}{4} B^{\mu\nu} B_{\mu\nu} - \frac{1}{2} \tilde{\mu}^2 \phi^{\mu} \phi_{\mu} \Big) \Big], \tag{163}$$

$$\begin{aligned} S_{\text{S}} = \int d^4x \sqrt{-g} \Big[& \frac{1}{G^3} \Big(\frac{1}{2} g^{\mu\nu} \nabla_{\mu} G \nabla_{\nu} G - V(G) \Big) \\ & + \frac{1}{\tilde{\mu}^2 G} \Big(\frac{1}{2} g^{\mu\nu} \nabla_{\mu} \tilde{\mu} \nabla_{\nu} \tilde{\mu} - V(\tilde{\mu}) \Big) + \frac{1}{G} \Big(\frac{1}{2} g^{\mu\nu} \nabla_{\mu} \omega \nabla_{\nu} \omega - V(\omega) \Big) \Big]. \end{aligned} \tag{164}$$

Here, $g_{\mu\nu}$ is the spacetime metric and ∇_{μ} is the covariant derivative compatible with this metric, R is the Ricci scalar, ϕ^{μ} represents a Proca-type massive vector field with $\tilde{\mu}$ being its mass, and $B_{\mu\nu} = \partial_{\mu}\phi_{\nu} - \partial_{\nu}\phi_{\mu}$ is the strength tensor of the vector field; $G(x)$, $\tilde{\mu}(x)$ and $\omega(x)$ are the scalar fields and $V(G)$, $V(\tilde{\mu})$ and $V(\omega)$ are the corresponding self-interaction potentials. The term S_{M} in the MOG action stands for possible matter distributions.

In order to find black hole solutions in the MOG theory, it is plausible [80] to make some simplifications for the action by neglecting the mass $\tilde{\mu}$ of the vector field, fixing the vector coupling to $\omega \equiv 1$ and defining an enhanced gravitational constant as

$$G = G_N(1+\chi), \qquad \partial_{\mu} G = 0 \tag{165}$$

with χ being a free modified parameter of the MOG theory. Given this approximation, the matter-free MOG action becomes

$$S = \frac{1}{16\pi G}\int d^4x\sqrt{-g}R - \frac{1}{4}\int d^4x\sqrt{-g}B^{\mu\nu}B_{\mu\nu}. \tag{166}$$

The field equations are then given by

$$G_{\mu\nu} = -8\pi G T_{\phi\mu\nu}, \quad \nabla_\nu B^{\mu\nu} = 0, \quad \nabla_\lambda B_{\mu\nu} + \nabla_\nu B_{\lambda\mu} + \nabla_\mu B_{\nu\lambda} = 0 \tag{167}$$

where $G_{\mu\nu}$ is the Einstein tensor and $T_{\phi\mu\nu}$ is the energy-momentum tensor for the vector field ϕ_μ given by

$$T_{\phi\mu\nu} = -\frac{1}{4}\Big(B_\mu^{\ \sigma}B_{\nu\sigma} - \frac{1}{4}g_{\mu\nu}B^{\sigma\beta}B_{\sigma\beta}\Big). \tag{168}$$

We observe that this MOG action and field equations appear similar as those for the Einstein-Maxwell theory [see Eqs. (3) and (4) and note the difference from $G = (1+\chi)G_N$]. The solution for a stationary, axisymmetric metric $g_{\mu\nu}$ and a vector field ϕ_μ of these MOG field equations (167) were found in [80], which in Boyer-Lindquist coordinates read [133]

$$ds^2 = -\frac{\Delta}{\Sigma}(dt - a\sin^2\theta d\phi)^2 + \frac{\sin^2\theta}{\Sigma}[(r^2+a^2)d\phi - adt]^2 + \frac{\Sigma}{\Delta}dr^2 + \Sigma d\theta^2, \tag{169}$$

$$\boldsymbol{\phi} = -\frac{\sqrt{\chi G_N}Mr}{\Sigma}(dt - a\sin^2\theta d\theta), \tag{170}$$

where

$$\Sigma(r,\theta) = r^2 + a^2\cos^2\theta, \tag{171}$$

$$\Delta(r) = r^2 - 2G_{\rm N}(1+\chi)Mr + a^2 + G_{\rm N}^2\chi(1+\chi)M^2. \tag{172}$$

The form of the metric (169) is similar as the KN metric (5) but it describes a rotating Kerr-like black hole in the MOG theory which has a neutral gravitational charge K (instead of an electric charge) corresponding to the vector field ϕ_μ by the postulate [80, 138, 77]

$$K = \sqrt{\chi G_N}M. \tag{173}$$

This Kerr-like black hole is referred to as the Kerr-MOG (KM) black hole. M and a are mass and spin parameters of the KM black hole, respectively.

4.3 ORBITING EMITTER NEAR KERR-MOG BLACK HOLE

For convenience, we rewrite the KM metric (169) in the standard form

$$ds^2 = -\frac{\Delta\Sigma}{\Xi}dt^2 + \frac{\Sigma}{\Delta}dr^2 + \Sigma d\theta^2 + \frac{\Xi\sin^2\theta}{\Sigma}(d\phi - \Omega_{\text{bh}}dt)^2, \tag{174}$$

where we have reset Newtonian constant $G_N = 1$ and defined

$$\Sigma = r^2 + a^2\cos^2\theta, \qquad \Delta = r^2 - 2M_\chi r + a^2 + Q_\chi^2, \tag{175a}$$

$$\Omega_{\text{bh}} = \frac{a(2M_\chi r - Q_\chi^2)}{\Xi}, \qquad \Xi = (r^2 + a^2)^2 - \Delta a^2\sin^2\theta, \tag{175b}$$

with

$$M_\chi = (1+\chi)M, \qquad Q_\chi^2 = (1+\chi)K^2 = \frac{\chi}{1+\chi}M_\chi^2. \tag{176}$$

Here, M_χ and $J = M_\chi a$ are the ADM mass and angular momentum of the KM black hole, respectively [139].

Solving the equation $\Delta = 0$ gives radii of the inner and outer event horizons,

$$r_\pm = M_\chi \pm \sqrt{M_\chi^2 - (a^2 + Q_\chi^2)}. \tag{177}$$

The extremal limit is obtained for $a^2 + Q_\chi^2 = M_\chi^2$.

Note that the quantities under the square roots of (173) and (177) should be non-negative, thus we obtain physical bounds on the parameter χ as [139]

$$0 \le \chi \le \frac{M_\chi^2}{a^2} - 1. \tag{178}$$

We assume that there exists an isotropic point emitting source orbiting on a circular, equatorial geodesic at radius r_s. The coordinate angular velocity of this source is [139]

$$\Omega_s = \pm\frac{\Gamma(r_s)}{r_s^2 \pm a\Gamma(r_s)}, \tag{179}$$

where $\Gamma^2(r) = M_\chi r - Q_\chi^2$, and the upper or lower sign corresponds to prograde (direct) or retrograde orbits, respectively. Here and hereafter, we use the subscript s to represent "source".

4.3.1 *Photon conserved quantities along trajectories*

The photon trajectories which connect a source to an observer are null geodesics in the KM spacetime. There are four conserved quantities for a photon along its trajectory: the invariant mass $\mu^2 = 0$, the total energy E, the angular momentum L and the Carter constant $\mathcal{Q}$ [85]. It is convenient to scale out the energy E from the trajectory by introducing two rescaled quantities related to the conserved quantities L and $\mathcal{Q}$ by

$$\hat{\lambda} = \frac{L}{E}, \qquad \hat{q} = \frac{\sqrt{\mathcal{Q}}}{E}. \tag{180}$$

Note that the Carter constant $\mathcal{Q}$ is non-negative for any photon passing through the equatorial plane. Thus we will always have positive and real $\hat{q}$ for the photons emitted from the equatorial plane.

Using the Hamilton-Jacobi method we can obtain the geodesic equations in integral form, which connect a source $(t_s, r_s, \theta_s, \phi_s)$ to an observer $(t_o, r_o, \theta_o, \phi_o)$ [80, 85], as

$$\fint_{r_s}^{r_o} \frac{dr}{\pm\sqrt{\mathcal{R}(r)}} = \fint_{\theta_s}^{\theta_o} \frac{d\theta}{\pm\sqrt{\Theta(\theta)}}, \tag{181a}$$

$$\Delta\phi = \fint_{r_s}^{r_o} \frac{a}{\pm\Delta\sqrt{\mathcal{R}(r)}}\left(2M_\chi r - Q_\chi^2 - a\hat{\lambda}\right)dr + \fint_{\theta_s}^{\theta_o} \frac{\hat{\lambda}\csc^2\theta}{\pm\sqrt{\Theta(\theta)}}d\theta, \tag{181b}$$

$$\begin{aligned}\Delta t = &\fint_{r_s}^{r_o} \frac{1}{\pm\Delta\sqrt{\mathcal{R}(r)}}\left[r^4 + a^2\left(r^2 + 2M_\chi r - Q_\chi^2\right) - a\left(2M_\chi r - Q_\chi^2\right)\hat{\lambda}\right]dr \\ &+ \fint_{\theta_s}^{\theta_o} \frac{a^2\cos^2\theta}{\pm\sqrt{\Theta(\theta)}}d\theta,\end{aligned} \tag{181c}$$

where $\Delta\phi = \phi_o - \phi_s$, $\Delta t = t_o - t_s$, and

$$\mathcal{R}(r) = \left(r^2 + a^2 - a\hat{\lambda}\right)^2 - \Delta\left[\hat{q}^2 + \left(a - \hat{\lambda}\right)^2\right], \tag{182a}$$

$$\Theta(\theta) = \hat{q}^2 + a^2\cos^2\theta - \hat{\lambda}^2\cot^2\theta. \tag{182b}$$

The function $\mathcal{R}(r)$ is called the radial "potential" and $\Theta(\theta)$ is called the angular "potential". $\mathcal{R}(r) = 0$ corresponds to turning points in the r direction and $\Theta(\theta) = 0$ corresponds to turning points in the θ direction. Here and hereafter, the subscript o stands for "observer".

Since the integrals are to be evaluated as path integrals along a trajectory connecting the source and observer, we have used the slash notation $\fint$ to distinguish them from ordinary integrals. The radial and angular turning points in the trajectory appear any time when the effective potential $\mathcal{R}(r) = 0$ or $\Theta(\theta) = 0$. The $\pm$ signs in these geodesic equations are chosen such that the corresponding terms are always integrated along the propagation direction of the photon trajectory. Given these turning points, there are different possibilities for light rays connecting a source to an observer. Thus we will introduce parameters b, m and s to distinguish them. For the r direction, we let $b = 0$ label those direct trajectories with no radial turning points and $b = 1$ label those reflected trajectories with one radial turning point. For the θ direction, we use $m \geq 0$ to record the number of angular turning points and use $s \in \{+1, -1\}$ to denote the final sign of p_θ (the θ-component of the photon's four-momentum).

Note that we have a relation between the unknowns, $\phi_s = \Omega_s t_s$, it then follows from Eqs. (181b) and (181c) that

$$\Delta\phi - \Omega_s \Delta t = \phi_o - \Omega_s t_o. \tag{183}$$

We will place the observer at $\phi_o = 2\pi N$ for an integer N (physically equivalent to $\phi_o = 0$) for all time t_o. Plugging $\phi_o = 2\pi N$ into Eq. (183), one can see that N is the net winding number which records the extra windings underwent by the photon relative to the source between its emission time and reception time [5]. Then the geodesic Eqs.(181) can be rewritten as the "KM lens equations"

$$I_r + b\tilde{I}_r = G_\theta^{m,s}, \tag{184a}$$

$$J_r + b\tilde{J}_r + \frac{\hat{\lambda} G_\phi^{m,s} - \Omega_s a^2 G_t^{m,s}}{M_\chi} = -\Omega_s t_o + 2\pi N, \tag{184b}$$

where we have introduced the factor of M_χ such that both lens equations become dimensionless, and I_r, $\tilde{I}_r$, J_r, $\tilde{J}_r$ and $G_i^{m,s}$ ($i \in \{t, \theta, \phi\}$) are defined in the same way as Ref. [5] (see also Sec. 2.6 and Appendices A & B).

For given values of N, m, s, b, $\hat{\lambda}$ and $\hat{q}$, Eqs. (184) determine the observer coordinates t_o, r_o, θ_o for given values of the source coordinates r_s, θ_s [note that we have chosen $\phi_o = 2\pi N$ and decoupled t_s and ϕ_s using Eq. (183)]. For a distant observer we have $r_o = \infty$ and for an equatorial source we have $\theta_s = \pi/2$. From another point of view, by solving Eq. (184) for given choice of N, m, s, b and given values of θ_o and r_s, one may find the solutions of $\hat{\lambda}$ and $\hat{q}$ in terms of t_o which are associated with the time-dependent images of the emitter seen by a distant observer.

4.3.2 *Observational appearance*

Following Refs. [90, 46, 5], we now consider the observational appearance of the point emitter: the images positions, redshift factors and fluxes. These observational quantities can be expressed in terms of the conserved quantities $\hat{\lambda}$ and $\hat{q}$.

The apparent position (α, β) of images on the observer's screen is given by

$$\alpha = -\frac{\hat{\lambda}}{\sin\theta_o}, \tag{185a}$$

$$\beta = \pm\sqrt{\hat{q}^2 + a^2\cos^2\theta_o - \hat{\lambda}^2\cot^2\theta_o} = \pm\sqrt{\Theta(\theta_o)}. \tag{185b}$$

The $\pm$ sign in front of β is equal to the sign of p_θ at the observer (i.e., the value of s), which represents whether the light ray arrives (relative to the observer) from above or below.

The "redshift factor" g is given by

$$g = \frac{1}{\gamma}\sqrt{\frac{\Delta_s\Sigma_s}{\Xi_s}}(1 - \Omega_s\hat{\lambda})^{-1}, \tag{186}$$

where we have introduced the boost factor γ, which is defined as

$$v_s = \frac{\Xi_s}{\Sigma_s\sqrt{\Delta_s}}[\Omega_s - \Omega_{\mathrm{bh}}(r_s)], \quad \gamma = \frac{1}{\sqrt{1 - v_s^2}}. \tag{187}$$

The ratio between the image flux F_o and the comparable "Newtonian flux" F_N is given by

$$\frac{F_o}{F_N} = g^3\frac{\hat{q}M_\chi}{\gamma\sin\theta_o}\sqrt{\frac{\Sigma_s\Delta_s}{\Xi_s\Theta(\theta_o)\Theta(\theta_s)\mathcal{R}(r_s)}}\left|\det\frac{\partial(B, A)}{\partial(\hat{\lambda}, \hat{q})}\right|^{-1}, \tag{188}$$

where we have defined

$$A \equiv I_r + b\tilde{I}_r - G_\theta^{m,s} \pm M_\chi \int_{\pi/2}^{\theta_s} \frac{d\theta}{\sqrt{\Theta(\theta)}}, \tag{189a}$$

$$B \equiv J_r + b\tilde{J}_r + \frac{\hat{\lambda} G_\phi^{m,s} - \Omega_s a^2 G_t^{m,s}}{M_\chi}. \tag{189b}$$

The plus or minus sign in Eqs. (189a) corresponds to pushing the emitter above or below the source plane $\theta_s = \pi/2$. The integrals are given in Appendices.

Note that the conserved quantities (185), (186) and (188) have the same form as that of Kerr case [5], but the difference is implied via the specific expressions for M_χ, Δ_s, $\Omega_{\rm bh}$ and Ω_s. If we take $\chi = 0$, the above results reduce to the Kerr case [5].

4.4 NEAR-EXTREMAL EXPANSION

Without loss of generality, we will choose $\theta_o \in (0, \pi/2)$ and set $M_\chi = 1$ in the following. We consider an emitter orbiting on (or near) the direct ISCO of a near-extremal KM black hole. We introduce a dimensionless radial coordinate R for convenience, which is related the Boyer-Lindquist radius r by

$$R = r - 1, \tag{190}$$

We also introduce a small parameter ϵ to describe the near-extremality of the black hole,

$$a^2 + Q_\chi^2 = 1 - \epsilon^3 \tag{191}$$

For simplicity, instead of using the parameter χ, we will use the spin a in the following expressions as the free parameter that describes the modified black hole. We can get the relation between χ and a from (176) and (191), as

$$\chi = \frac{1}{a^2} - 1 + \mathcal{O}(\epsilon^3). \tag{192}$$

Following the procedure introduced in Sec. 2.3.1, we find that the ISCO of a near-extremal KM black hole to the leading order in ϵ is at

$$R_{\rm ISCO} = \Big(\frac{2a^2}{2a^2-1}\Big)^{1/3}\epsilon + \mathcal{O}(\epsilon^2). \tag{193}$$

Note that we have to choose $a > \sqrt{2}/2$ to guarantee that the ISCO resides in the outside of the event horizon, this corresponds to a restriction for the modified parameter χ,

$$\chi < 1. \tag{194}$$

We consider a distant observer located at $R_o = (r_o - 1) \approx r_o$ while we put the emitter on or near the ISCO,

$$R_s = \epsilon\bar{R} + \mathcal{O}(\epsilon^2), \qquad \bar{R} \geq \Big(\frac{2a^2}{2a^2-1}\Big)^{1/3}. \tag{195}$$

Thus, to leading order in ϵ we have

$$r_s = 1 + \epsilon\bar{R}. \tag{196}$$

Following Ref. [5, 4], we will also introduce new quantities λ and q defined by

$$\hat{\lambda} = \frac{1+a^2}{a}(1-\epsilon\lambda), \qquad \hat{q} = \sqrt{4 - \frac{1}{a^2} - q^2}. \tag{197}$$

For later reference, we expand the orbital frequency Ω_s and period T_s in ϵ, leading to the expressions

$$\Omega_s = \frac{a}{1+a^2} + \mathcal{O}(\epsilon), \qquad T_s = \frac{2(1+a^2)\pi}{a} + \mathcal{O}(\epsilon). \tag{198}$$

Note that the orbital frequency/period in the near-extremal KM case for $0 < a < 1$ is smaller/greater as compared to the near-extremal Kerr case [5].

If we take $a = 1$ (corresponding to $\chi = 0$), the above results reduce to the Kerr case [5].

4.4.1 *Photon conserved quantities along trajectories*

We will seek for solutions of Eq. (245) ($\hat{\lambda}$, $\hat{q}$, or equivalently, λ, q) to subleading order in ϵ. Note that we must keep the $\mathcal{O}(\epsilon^0)$ terms in the lens equations in order to get a solution for λ.

4.4.1.1 *First equation*

We start by solving the first equation (184a),

$$I_r + b\tilde{I}_r = mG_\theta - s\hat{G}_\theta. \tag{199}$$

The I integrals and G integrals are performed in the Appendices. Since t_o does not appear in the first equation, for given choice of m, s, b, we will express λ as a function of q by plugging the results of integrals in the equation. Following the method of Ref. [5], for each choice of m, b, s, and q, we obtain the solution of Eq. (199) and the conditions for its existence. The conditions are given by

$$\bar{R} < \frac{4\Upsilon}{q^2}\left(1 + \frac{2}{\sqrt{4-q^2}}\right) \quad \text{if} \quad b = 0, \tag{200a}$$

$$\bar{R} > \frac{4\Upsilon}{q^2}\left(1 + \frac{2}{\sqrt{4-q^2}}\right) \quad \text{if} \quad b = 1, \tag{200b}$$

and the solution is

$$\lambda = \frac{4\Upsilon}{(1+a^2)(4-q^2)}\left[2 - q\sqrt{1 + \frac{4-q^2}{2\Upsilon}\bar{R}}\right]. \tag{201}$$

Here, $\Upsilon > 0$ is defined by

$$\Upsilon \equiv \frac{q^4 R_o}{q^2 + 2R_o + qD_o} e^{-qG_\theta^{\bar{m},s}} = \frac{q^4}{q+2} e^{-qG_\theta^{\bar{m},s}} + \mathcal{O}(\frac{1}{R_o}), \tag{202}$$

where D_o is defined in (301) and $G_\theta^{\bar{m},s}$ is defined in (307) and (308), with

$$\bar{m} = m + \frac{1}{qG_\theta}\log\epsilon. \tag{203}$$

Note that Υ is independent of R_o for large R_o.

4.4.1.2 *Second equation*

Next we move on to the second equation (184b) which gives another relation between t_o, λ and q for given choice of m, s, b. We will look for functions $\lambda(\hat{t}_o)$ and $q(\hat{t}_o)$ which are associated with the time-dependent tracks of images. We introduce a dimensionless time coordinate $\hat{t}_o$ such that the emitter has unit periodicity in terms of it,

$$\hat{t}_o = \frac{t_o}{T_s} = \frac{a t_o}{2(1+a^2)\pi} + \mathcal{O}(\epsilon). \tag{204}$$

We then rewrite Eq. (184b) in terms of this dimensionless time coordinate

$$\hat{t}_o = N + \mathcal{G}, \qquad \mathcal{G} \equiv -\frac{1}{2\pi}\Big(J_r + b\tilde{J}_r + \frac{1+a^2}{a}G_\phi^{m,s} - \frac{a^3 G_t^{m,s}}{1+a^2}\Big). \tag{205a}$$

The J integrals and G integrals are given in the Appendices.

Since the problem is periodic, we will consider the single period $\hat{t}_o \in [0,1]$. For each given choice of m, s, b having a non-vanishing range of q satisfying Eq. (200), the first lens Eq. (184a) gives a function $\lambda(q)$ [Eq. (201)], the second lens Eq. (184b) [or equivalently, Eq. (205)] then gives a function $\hat{t}_o(q)$ for each choice of an integer N. Note that the integral N is uniquely determined for each value of q in the given period $0 \le \hat{t}_o < 1$. Then the multivalued inverse $q(\hat{t}_o)$ corresponds to the time-dependent tracks of the emitter's images. For each allowed N within the corresponding range of q, the function $\hat{t}_o(q)$ may either be monotonic or has local maxima and/or minima. For the monotonic ones, we are able to get the inverse $q(\hat{t}_o)$. For the non-monotonic ones, we divide $\hat{t}_o(q)$ into several invertible parts to get their inverse and label each inverse $q_i(\hat{t}_o)$ with a discrete integer i. Then the image track is divided into several segments which associate with these functions $q_i(\hat{t}_o)$ and each of these track segments can be labeled by a set of (m, b, s, N, i). Finding all the track segments for all choices of $(m,\, b,\, s,\, N,\, i)$ gives all the image tracks which altogether then build up the complete observable information of the hot spot. We give an example in Sec. 4.6 describing a practical approach for realizing this process.

4.4.1.3 *Winding number around the axis of rotation*

The winding number for a light ray around the rotating axis is given by $n = \text{mod}_{2\pi}\Delta\phi$, where $\Delta\phi$ can be obtained from Eq. (181b). Using the MAE method introduced in App. A, we now compute $\Delta\phi$ to the leading order in ϵ and obtain

$$\Delta\phi = \frac{a}{(1+a^2)\lambda\epsilon}\left(\frac{D_s}{\bar{R}} - q\right) + \mathcal{O}(\log\epsilon), \tag{206}$$

where D_s is defined in (301). We observe that $\Delta\phi$ scales as ϵ^{-1} at the leading order.

4.4.2 *Observational appearance*

Recall from the beginning of Sec. 5.4 that for near-extremal KM we have

$$\chi = \frac{1}{a^2} - 1 + \mathcal{O}(\epsilon^3), \qquad r_s = 1 + \epsilon\bar{R}, \tag{207a}$$

$$\hat{\lambda} = \frac{1+a^2}{a}(1+\epsilon\lambda), \qquad \hat{q} = \sqrt{4 - \frac{1}{a^2} - q^2}. \tag{207b}$$

We now expand the observational quantities to the leading order in ϵ. The quantities involved are the apparent position (246), the redshift factor (247) and the flux (249).

4.4.2.1 *Image positions and redshift factors*

The image position (246) on the observer's screen is expanded as

$$\alpha = -\frac{1+a^2}{a}\frac{1}{\sin\theta_o} + \mathcal{O}(\epsilon), \tag{208a}$$

$$\beta = s\sqrt{4 - \frac{1}{a^2} - q^2 + a^2\cos^2\theta_o - \frac{(1+a^2)^2}{a^2}\cot^2\theta_o} + \mathcal{O}(\epsilon). \tag{208b}$$

Note that the leading order position does not depend on λ. We should impose the requirement that β is real to make sure the light rays can reach a distant observer, which gives a range of q:

$$q \in \left[0, \sqrt{4 - \frac{1}{a^2} + a^2\cos^2\theta_o - \frac{(1+a^2)^2}{a^2}\cot^2\theta_o}\right]. \tag{209}$$

As $\epsilon \to 0$, Eqs. (208) and (209) gives a vertical line segment on which all images of the hot spot appear. We call this vertical line the NHEK-MOG line, being the analog of NHEKline for Kerr [5] (Sec. 4.5). We find that when $\theta_o < \theta_{\rm crit}$ [Eq. (222)] the range of q vanishes so does the emitter's image. Note that the NHEK-MOG line also disappears at this critical inclination (Sec. 4.5).

The redshift (186) is expanded as

$$g = \frac{1}{\frac{\sqrt{4a^2-1}}{a} + \frac{2a(1+a^2)}{\sqrt{4a^2-1}}\frac{\lambda}{\bar{R}}} + \mathcal{O}(\epsilon). \tag{210}$$

Note that from the cosines of emission angles one can establish a upper bound for g [5], which is

$$g \leq \frac{a(1+2a)}{\sqrt{4a^2-1}}. \tag{211}$$

4.4.2.2 *Image fluxes*

The normalized image flux (188) is expanded as

$$\frac{F_o}{F_N} = \frac{\sqrt{4a^2-1}\epsilon\bar{R}}{2a^2 D_s}\frac{qg^3}{\sqrt{4-\frac{1}{a^2}-q^2}\sqrt{\Theta_0(\theta_o)}\sin\theta_o}\left|\det\frac{\partial(B,A)}{\partial(\lambda,q)}\right|^{-1}, \tag{212}$$

where g is given in Eq. (210) and D_s is given in Eq. (301), and [see Eq. (208)]

$$\Theta_0(\theta_o) = \Theta(\theta_o)\big|_{\lambda=0} = 4 - \frac{1}{a^2} - q^2 + a^2\cos^2\theta_o - \frac{(1+a^2)^2}{a^2}\cot^2\theta_o = \beta^2, \tag{213}$$

and [see Eqs. (189)]

$$\begin{aligned}\left|\det\frac{\partial(B,A)}{\partial(\lambda,q)}\right| = &\left|\frac{\partial}{\partial\lambda}\left(J_r + b\tilde{J}_r\right)\left[\frac{\partial}{\partial q}\left(I_r + b\tilde{I}_r\right) - \frac{\partial G_\theta^{m,s}}{\partial q}\right]\right.\\ &\left.-\frac{\partial}{\partial\lambda}\left(I_r + b\tilde{I}_r\right)\left[\frac{\partial}{\partial q}\left(J_r + b\tilde{J}_r\right) + \frac{\partial G_{t\phi}^{m,s}}{\partial q}\right]\right| + \mathcal{O}(\epsilon\log\epsilon),\end{aligned} \tag{214}$$

where we have defined

$$G_{t\phi}^{m,s} = \hat{\lambda}G_\phi^{m,s} - \Omega_s a^2 G_t^{m,s} = \frac{1+a^2}{a}G_\phi^{m,s} - \frac{a^3}{1+a^2}G_t^{m,s} + \mathcal{O}(\epsilon). \tag{215}$$

The G, I, J integrals and the variations of I, J integrals with respect to λ and q are given in the Appendices A and B.

4.5 SHADOW AND NHEK-MOG LINE

The entire image of a black hole observed from the EHT is expected to be the black hole "shadow". To understand the images of the emitter better, we compute the edge of a shadow cast by an extremal KM black hole. The boundary of a black hole shadow is determined by the threshold from which the photons can escape to asymptotic infinity [37], which corresponds to unstable spherical null geodesics with fixed $r = \tilde{r}$.

First, we consider the non-extremal case and restore M_χ. For spherical photon orbits we have

$$\mathcal{R}(\tilde{r}) = \mathcal{R}'(\tilde{r}) = 0, \tag{216}$$

where $\mathcal{R}(r)$ is defined in Eq. (182a) and the prime represents derivative with respect to $\tilde{r}$. For a generic KM black hole we have $0 < a^2 + Q_\chi^2 < M_\chi^2$. Then from Eq. (216) we get

$$\hat{\lambda} = -\frac{\tilde{r}(\tilde{r}^2 - M_\chi\tilde{r} - 2\Gamma(\tilde{r})^2) + a^2(\tilde{r} + M_\chi)}{a(\tilde{r} - M_\chi)}, \tag{217a}$$

$$\hat{q} = \frac{\tilde{r}\sqrt{4a^2\Gamma(\tilde{r})^2 - (\tilde{r}^2 - M_\chi\tilde{r} - 2\Gamma(\tilde{r})^2)^2}}{a(\tilde{r} - M_\chi)}, \tag{217b}$$

where $\Gamma(\tilde{r}) = M_\chi\tilde{r} - Q_\chi^2$. The shadow boundary (critical curve) is obtained by substituting Eqs. (217) for $\hat{\lambda}$ and $\hat{q}$ into the screen coordinates (α, β) [Eq. (185)]. The resulting curve is described by $[\alpha(\tilde{r}), \beta(\tilde{r})]$ with $\tilde{r}$ ranging over the photon region where both $\hat{q}$ and β are real.

4.5.1 *Extremal limit*

Following the procedure of Ref. [5], we now consider the extremal limit. We set $M_\chi = 1$ again and let $a^2 + Q_\chi^2 \to 1$. Then Eq. (217) yields

$$\hat{\lambda} = -\frac{1}{a}(\tilde{r}^2 - 2\tilde{r} - a^2), \tag{218a}$$

$$\hat{q} = \frac{\tilde{r}}{a}\sqrt{4a^2 - (\tilde{r} - 2)^2}, \tag{218b}$$

and the condition that $\hat{q}$ is real gives a range of $\tilde{r}$,

$$\tilde{r} \in [\tilde{r}_-, \tilde{r}_+] = [1, 2(a+1)], \tag{219}$$

Then the shadow boundary is given by the curve

$$\alpha(\tilde{r}) = \frac{1}{a}(\tilde{r}^2 - 2\tilde{r} - a^2)\csc\theta_o, \tag{220a}$$

$$\beta(\tilde{r}) = \pm\sqrt{\frac{\tilde{r}^2}{a^2}\left(4a^2 - (\tilde{r}-2)^2\right) + a^2\cos^2\theta_o - \left(\frac{\tilde{r}^2 - 2\tilde{r} - a^2}{a}\right)^2\cot^2\theta_o}. \tag{220b}$$

However, curves given by these equations are not always closed. We show the open curves for different values of a in the dashed line in Fig. 14. The two endpoints are at the positions corresponding to $\tilde{r} = \tilde{r}_- = 1$ which are given by

$$\alpha_{\text{end}} = -\frac{1+a^2}{a}\csc\theta_o, \tag{221a}$$

$$\beta_{\text{end}} = \pm\sqrt{4 - \frac{1}{a^2} + a^2\cos^2\theta_o - \frac{(1+a^2)^2}{a^2}\cot^2\theta_o}. \tag{221b}$$

Note that there are no endpoints at all when β_{end} is no longer real, and thus the curves are closed. Then we can obtain a condition for an open curve on the inclination angle, which is given by $\theta_{\text{crit}} < \theta_o < \pi - \theta_{\text{crit}}$, where

$$\theta_{\text{crit}} = \arctan\sqrt{\frac{a^2 + 3 - 2\sqrt{2+a^2}}{2\sqrt{2+a^2} - 3}}. \tag{222}$$

Therefore, we notice that an important piece for the open curve has been missed in the extremal limit. To recover the missing piece and make the curve closed in that case, we reconsider the extremal limit $a^2 + Q_\chi^2 \to 1$ by introducing

$$a^2 + Q_\chi^2 = 1 - \kappa^2, \qquad \tilde{r} = 1 + \kappa\tilde{R}. \tag{223}$$

As $\kappa \to 0$, the missing part of the shadow boundary is recovered by plugging (223) in (217), as

$$\alpha = -\frac{1+a^2}{a}\csc\theta_o, \tag{224a}$$

$$|\beta| < \sqrt{4 - \frac{1}{a^2} + a^2\cos^2\theta_o - \frac{(1+a^2)^2}{a^2}\cot^2\theta_o}. \tag{224b}$$

We show this in the solid lines in Fig. 14 and name this segment the NHEK-MOG line which is the analog of the NHEKline in Kerr spacetime [5]. We see that the images of a near-ISCO orbiting emitter appear on this NHEK-MOG line [see Eq. (208)].

Therefore, the shadow boundary of an extremal KM black hole is given by the union of the open curve (220) and the NHEK-MOG line (224).

4.6 RESULTS AND DISCUSSION

No.	a	χ	$\bar{R}_{\text{ISCO}}$	θ_{crit}
1	0.717	0.945	3.317	54.758°
2	0.75	0.778	2.080	53.228°
3	0.8	0.563	1.660	51.353°
4	0.85	0.384	1.481	49.881°
5	0.9	0.235	1.377	48.716°
6	0.95	0.108	1.309	47.792°
7	1	0	1.260	47.059°

Table 1.: The range of the deformation parameters χ, the dimensionless radii of the ISCO $\bar{R}_{\text{ISCO}}$ (Eq. (225)) and the critical observer inclinations θ_{crit} (Eq. (222)), corresponding to different values of the spin parameters a for the extremal KM black holes, where we choose $a = \sqrt{2}/2 + 10^{-2} \approx 0.717$ as the critical case.

We now describe the results with figures and discuss them in detail. First we will look at the silhouettes (shadow) of a near-extremal KM black hole and discuss how the size is changed when the free parameter χ [we will also equivalently use a as the free parameter in later discussion since there is a relation (192) between them for the near-extremal cases] is changed. Then, we will focus on a special portion of the shadow, the NHEK-MOG line, where the images of the point emitter appear. These images have some characteristic features which are similar to that of a near-extremal (high-spin) Kerr black hole.

The modified parameter that we wish to consider should satisfy the physical bounds (178) and (194), which gives a range of $0 \leq \chi < 1$ (corresponding to $1 \geq a > \sqrt{2}/2$). These choices are also in the allowed range for supermassive black holes, $0.03 < \chi < 2.47$ [130] (except for the critical case $\chi = 0$). For each choice of the modified parameter χ (in our formulae we use a instead), the observable quantities of a hot spot depend on four physical parameters, ϵ, $\bar{R}$, R_o, and θ_o. To make our approximations sufficiently accurate, one must choose $\epsilon \ll 1$ and $R_o \gg 1$. For the emitting source to be on a stable circular orbit of a near-extremal KM black hole, one must choose $\bar{R} \geq \left(\frac{2a^2}{2a^2-1}\right)^{1/3}$. To ensure that an observer can possibly see the flux, one needs to set the observer on a place with inclination satisfying $\arctan\sqrt{\frac{a^2+3-2\sqrt{2+a^2}}{2\sqrt{2+a^2}-3}} < \theta_o < \frac{\pi}{2}$. When $a = 1$ the KM case reduces to the Kerr case. We will consider a special example with the same choice of parameters as in Ref. [5], in order to compare the results. The parameters are as follows:

$$R_o = 100, \qquad \theta_o = \frac{\pi}{2} - \frac{1}{10} = 84.27^\circ, \tag{225a}$$

$$\epsilon = 0.01, \qquad \bar{R} = \bar{R}_{\mathrm{ISCO}} = \left(\frac{2a^2}{2a^2-1}\right)^{1/3}. \tag{225b}$$

This describes a hot spot (orbiting emitter) on the ISCO of a near-extremal KM black hole with spin a given in Table 1, viewed by a distant observer from a nearly edge-on inclination. (Note that the parameter a is the spin of a precisely extremal black hole, however, it is also the spin of a near-extremal black hole to leading order in ϵ. Here and hereafter, we ignore this difference.) Table 1 shows the ranges of χ, $\bar{R}_{\mathrm{ISCO}}$ and θ_{crit} corresponding to different values of a. We find that $\bar{R}_{\mathrm{ISCO}}$ and θ_{crit} [Eq. (222)] increase when χ is increased and that a decreases when χ is increased. This agrees with Ref. [134] where the authors find that the ISCOs of KM black holes are always greater than that of Kerr black hole.

4.6.1 *Silhouettes of black hole*

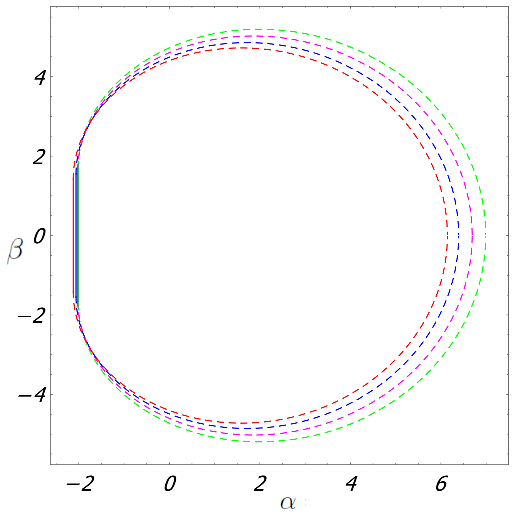

Figure 14.: Edges of near-extremal KM black hole shadows, where the dashed lines are the open parts [Eq. (220)] and the vertical solid lines are the NHEK-MOG lines [Eq. (224)]. The green, magenta, blue and red curves have $a = 1, 0.9, 0.8, 0.717$ ($\chi = 0, 0.235, 0.563, 0.945$), respectively.

Fig. 14 shows the edges of near-extremal KM black hole shadows (see Sec. 4.5). We find that the sizes of shadows cast by a near-extremal KM black hole decrease when the free parameter χ is increased from zero. The length of the NHEK-MOG line and the solid angle corresponding to it also decrease while the free parameter χ is increased from zero. In Ref. [44], Moffat found that the sizes of shadows cast by KM black holes increase significantly as the free parameter χ is increased from zero. This is not conflicting with our results because in their paper one compares the sizes of shadows for black holes with same parameter M, while we compare that for black holes with same ADM mass $M_\chi = (1 + \chi)M$.

4.6.2 *Images on the NHEK-MOG line*

Following the procedure of Ref. [5] and using the open numerical code therein, we now show the images of an emitter orbiting on ISCO. As discussed in Sec. 4.5, all the images appear on a vertical line, the NHEK-MOG line. These images correspond to photons arriving with different combinations of the parameters m, s, b, N, as well as an additional label i if $\hat{t}_o(q)$ [or equivalently $\mathcal{G}(q)$] is not monotonic [see the discussion below Eq. (205)]. In the practical approach [Fig. 15], we first choose the parameters m, s, b, and then find the allowed value of N as well as necessary labels i for those non-monotonic functions $\hat{t}(q)$. Fig. 15 shows examples of representative track segments for $a = 1$ and $a = 0.8$. We choose $m = 2$, $b = 0$, $s = +1$ for the light rays and choose the physical parameters (225), which are the same as Ref. [5] for comparison. We find that the cases with $a = 1$ (the Kerr case) and $a = 0.8$ have similar features but the modified parameter χ causes corrections to the associated functions: $\mathcal{G}$ decreases and F_o/F_N increases while a is decreased.

For each track segment $q(\hat{t}_o)$ labeled by (m, b, s, N, i), Eq. (201) gives a function $\lambda(\hat{t}_o)$. Given these two time-dependent conserved quantities λ and q, we can then obtain the main observational quantities for this track segment of the image. These observational quantities are the apparent position (α, β) [Eq.(208)], the redshift factor g [Eq. (210)], and the normalized image flux F_o/F_N [Eq. (212)]. Then we build up the most observable information of the hot spot by including several brightest track segments. Note that only a few values of N and m are important because the image flux for others are negligibly small (see Fig. 15 and Fig. 17 for details). Below we describe the most important features of the images in Fig. 16.

Fig. 16 shows the main observational quantities for three different near-extremal KM cases, $a = 1$, $a = 0.8$ and $a = 0.717$ (corresponding to $\chi = 0$, $\chi = 0.563$ and $\chi = 0.945$, respectively). In each case, the green line is a bright primary image while others are secondary images. For $a = 1$, it reduces to the Kerr case and we see that our results exactly agree with Ref. [5]. For $a = 0.8$ and

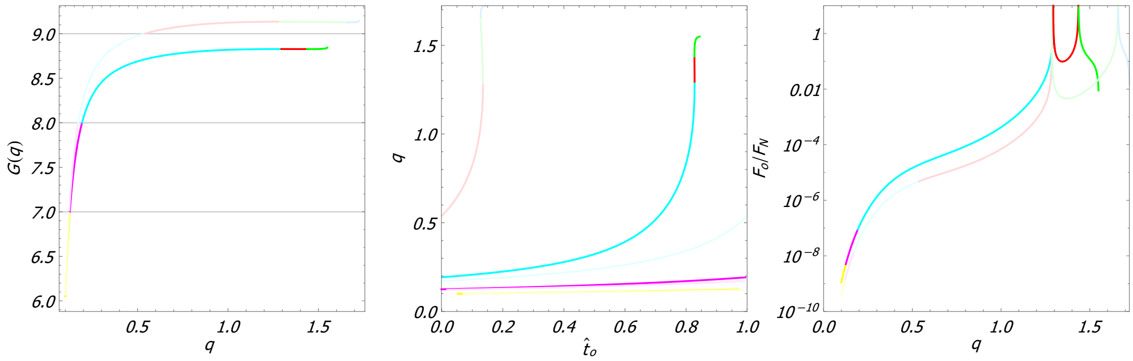

Figure 15.: Left to right: plots of $\mathcal{G}(q)$, $q(\hat{t}_o)$ and $F_o/F_N(q)$ for $a = 1$ (light curves) and $a = 0.8$ (bright curves) with $m = 2$, $b = 0$, $s = +1$ and the parameter choices of (225). For $a = 1$, the light yellow, light magenta and light cyan curves have $N = -6, -7, -8$, respectively, and no additional label i, while the light red, light green and light blue curves have $N = -9$ and $i = 1, 2, 3$, respectively. For $a = 0.8$, the yellow and magenta curves have $N = -6, -7$, respectively, and no additional label i, while the cyan, red and green curves have $N = -8$ and $i = 1, 2, 3$, respectively. Note that for $a = 1$, the KM case reduce to the Kerr case so that the light curves agree with those in Ref. [5] exactly. (Although the condition (200) allows the entire range of q, we have imposed a small-q cutoff since the corresponding image fluxes are negligibly small.)

$a = 0.717$ (the critical case), the general features are qualitatively similar to the case of $a = 1$ but quantitatively corrected. We find that there are continues tracks moving on the NHEK-MOG line which are lined up by separate track segments and that the NHEK-MOG line flashes when different tracks intersect [5]. While Fig 16 shows that the typical image positions remain unchanged for different value of a, we see from Fig. 14 that the length of the NHEK-MOG line decreases when a is decreased, i.e. the maximum value of the screen coordinate $\beta_{\max}$ decreases when the free parameter χ is increased from zero. The flux intensity increases when the black hole spin is decreased. This is also true in the near-extremal Kerr cases when considering different values of ϵ (and considering the precise spins of the black holes) [5] since the typical flux scales as $\epsilon / \log \epsilon$. In each case for $a = 1$, 0.8, 0.717, the primary image appears near the center of the NHEK-MOG line, then moves downward while blueshifts and peaks in brightness. The winding number of these segments of primary images in the modified cases are decreased when χ is increased. For example, the winding numbers range between 17 and 23, 11 and 16, 6 and 8, for spin $a = 1$, 0.8, and 0.717, respectively (see Fig. 18). For the near-extremal KM cases, the peak redshift factors are all at $g \approx 1.6$ but they correspond to different emission angles. For example, they correspond to light emitted in cones of 27°, 20° and 25° around the forward direction [5] for $a = 1$, 0.8 and 0.717, respectively. However, another typical redshift factor (corresponding to $\lambda \sim 0$) associated with the secondary images increases when the spin parameter a is decreased, at $g = a/\sqrt{4a^2 - 1}$. For the near-extremal Kerr cases, both typical redshifts for primary and secondary images do not change when the spin is increased (by choosing different value of ϵ and considering the precise spins of the black holes) [5]. The reason for this difference is that the range of spin is very limited for the near-extremal Kerr black hole, but it becomes wider for near-extremal KM black holes. This is why we only take $\epsilon = 0.01$ into consideration. In addition, the above signatures in the near-extremal KM case appear periodically with period greater than that in near-extremal Kerr case [see Eq. (198)].

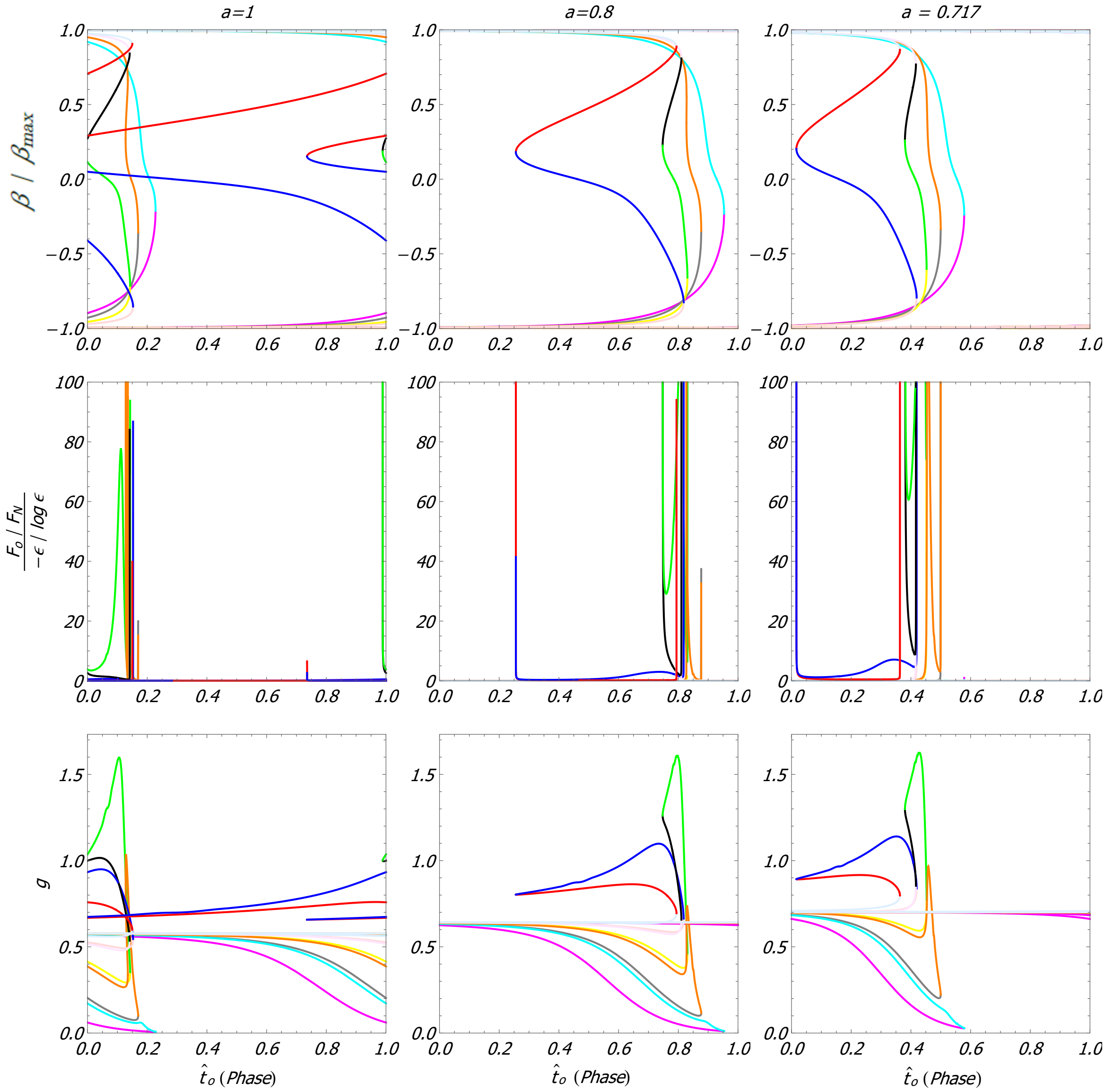

Figure 16.: Observables of the most important few images for three different values of near-extremal spin of KM black holes with the parameter choices of (225). From top to bottom, we plot positions, fluxes and redshift factors. Form left to right, we have $a = 1$ (Kerr case [5]), $a = 0.8$ and $a = 0.717$ (critical case for there exist ISCO for a near-extremal KM black hole). The color-coding is the same as that of Ref. [5]: each of these colored lines maybe a composition of several continuous track segments. For example, the green line (denoting the primary image) is consisted of 4, 3, and 3 segments in the $a = 1$, 0.8, 0.717 cases, respectively.

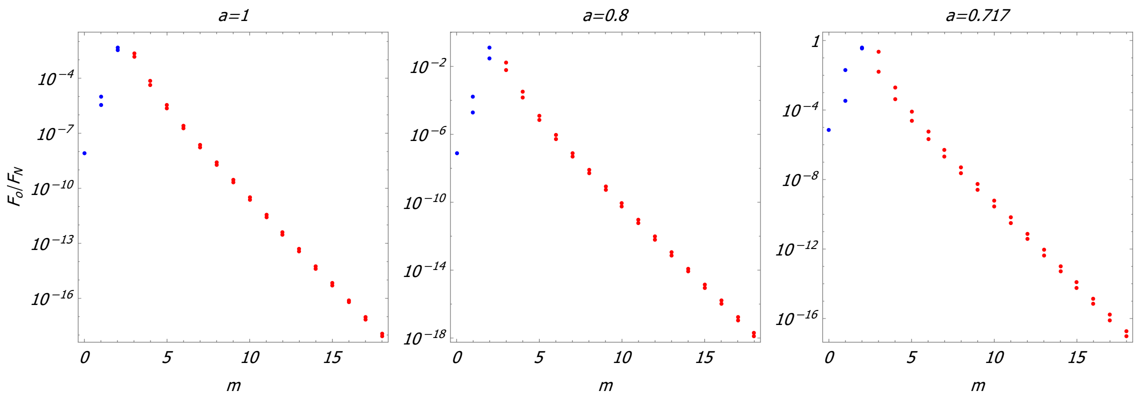

Figure 17.: Left to right: plots of F_o/F_N for $a = 1$ (Kerr case [5]), $a = 0.8$ and $a = 0.717$ (critical case for there exist ISCO for a near-extremal KM black hole) with physical parameters (225). We set $q = 1.5$, 1.38, and 1.35 for $a = 1$, 0.8, and 0.717, respectively, and let m vary in each case. We denote the direct/reflected (b=0/b=1) images by blue/red dots. For $m = 0$, we have only one image corresponding to $s = -1$, for each other value of m, we have two images corresponding to $s = \pm 1$.

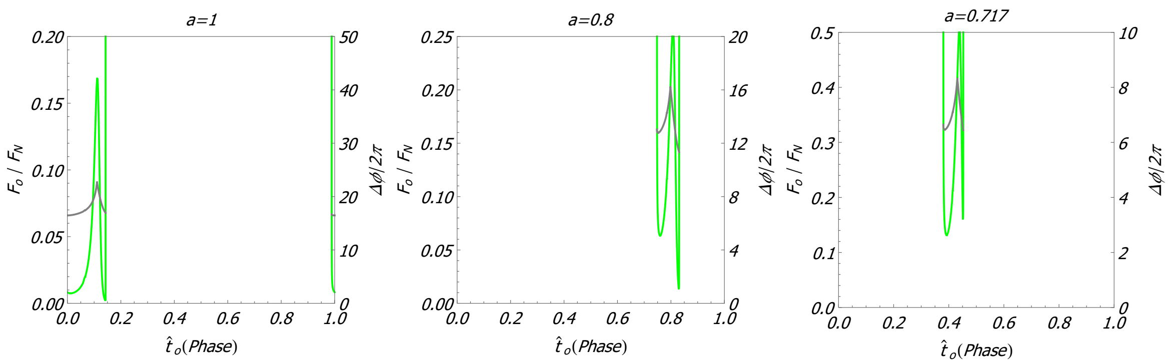

Figure 18.: Left to right: plots of flux F_o/F_N (green) and winding number $\Delta\phi/2\pi$ (gray) of the primary image for $a = 1$ (Kerr case [5]), $a = 0.8$ and $a = 0.717$ (critical case for there exist ISCO for a near-extremal KM black hole) with physical parameters (225). Note that as mentioned below Fig. 16, the single primary image for each case is a composition of multiple track segments.

The typical redshift factors are related to observations since they could shift the iron Kα line at $E_{\mathrm{FeK}\alpha} = 6.4$ keV to $6.4g$ keV. For blueshifted primary image, the factor $g \approx 1.6$ will shift the iron line to 10.2 keV. For redshifted secondary images, the redshift factors for $a = 1$, 0.8 and 0.717 will shift the iron line to 3.7 keV, 4.1 keV and 4.5 keV respectively. However, rather than close to the observed peak at 3.5 keV [92], they are even more away from it in modified cases than in Kerr case [5].

4.7 SUMMARY

In this chapter, we analytically compute the observational signature of a near-extremal rotating black hole in the modified gravity theory (MOG), which is also referred as scalar-tensor-vector theory (STVG). The rotating black hole in this theory called as the Kerr-MOG (KM) black hole, introducing a modified parameter χ in addition to the parameters of Kerr black hole. When the parameter χ goes to zero, the modified black hole reduces to Kerr black hole. The range of the modified parameter that we considered is $0 \leq \chi < 1$, which is in the supposed range for a supermassive black hole [130]. To be specific, we compute the near-extremal KM black hole's shadow and the position, redshift and flux of a orbiting hot spot's image. Compared with the signature produced in the Kerr background, the MOG case exhibits the following differences:

1. The size of the shadow cast by a KM black hole decreases when the modified parameter χ is increased.

2. The targeted astrophysical black hole could be one that has a smaller reduced spin than a corresponding near-extremal Kerr black hole, since the reduced spin parameter a can be in the range $0.717 < a < 1$. The spin of a near-extremal KM black hole decreases when the modified parameter is increased.

3. The image of the hot spot appears periodically in the leftmost vertical line (NHEK-MOG line) of the shadow with a period greater than that of Kerr. The period increases when the modified parameter is increased.

4. The flux of the image increases when the modified parameter is increased.

5. The typical redshift associated with the secondary image increases when the modified parameter is increased.

5

KERR-SEN

5.1 INTRODUCTION

Black holes are among the most important predictions of general relativity (GR), as well as other gravitational theories. Thus, attempts to discover black holes have received continuing impetus over many decades. Now it eventually has become reality with the detections of gravitational waves by LIGO and Virgo [16, 17] and with the first image of the black hole M87* photographed by the Event Horizon Telescope (EHT) Collaboration [21, 22, 23, 24, 25, 26]. Yet, there is still an urgent need for more precise theoretical templates to match these data, which has triggered exciting research among the gravity community [93, 35, 39, 32, 140].

From the first image of the M87*, a bright ring surrounding a dark region was observed as an important feature of a black hole. The dark region is known as the "black hole shadow" and the bright ring is elicited by the luminous sources outside the black hole [21]. Even though it has not been resolved yet, this observed bright ring is supposed to has an intricate substructure which may be observable on long interferometric baseline observations [32]. As we know, a black hole itself is invisible and it is the surrounding luminous matters that make it observable. Thus, the appearance of a black hole depends closely on its surroundings. Within the surrounding luminous matter, a bright point emitter (refer to as "hot spot") is particularly interesting and can produce striking observational signals. In the 1970s, the optical appearance of a hot spot (star) orbiting on a circular orbit of an extremal Kerr black hole has been studied in Refs. [90, 46]. Recently, the observational signature produced by a hot spot on, or near, the innermost stable circular orbit (ISCO) of a near-extremal Kerr black hole has been studied in Ref. [5], where a striking signature of high-spin Kerr black hole was found. Later, the influence of a surrounding plasma on that signature has been studied in Ref. [2]. Besides these, the image of a non-stationary plunging hot spot approaching a black hole has been studied in Refs. [141, 142, 49]. All these studies are based on the assumption that the underlying gravity theory is GR. Nevertheless, there are also black holes in alternative gravity theories [81, 121, 123, 124, 125, 77] based on different motivations. It is interesting to study the observational signature of a black hole (and hot spot) in these theories. Given this motivation, the signature of a Kerr-MOG (KM) black hole in the scalar-tensor-vector modified gravity theory (MOG) has been studied in Ref. [1]. Among other gravity theories that modify GR, perhaps the most theoretically important one is string theory, since it is one of the most attractive candidates for quantum gravity and unified theory. Thus, in this chapter we will study the observational signals produced by a hot spot orbiting a near-extremal rotating black hole arising from the string theory.

In a low-energy limit of heterotic string theory, a rotating black hole solution has been found in Ref. [81], known as the Kerr-Sen (KS) black hole. In addition to the mass M and angular momentum J, the KS black hole has a third physical parameter: the electric charge Q corresponding to a $U(1)$ gauge field. Much attention has been paid to the KS black hole including studies of null geodesics, photon motion and optical appearance (shadow) of a black hole [143, 144, 145, 146, 147, 43, 148]. Moreover, the apparent shape in the KS spacetime has also been compared to those in various charged/rotating black holes and naked singularities of the Kerr-Newman (KN) class of spacetimes [146, 148]. It is instructive to compare the results for the KS black hole with those for the KN black hole since the later is the charged and rotating solution in the Einstein-Maxwell theory [i.e., GR coupled to a $U(1)$ gauge field]. The main target of this chapter is therefore to compute the signature produced by a hot spot near a near-extremal KS black hole, and compare this to that of a near-extremal KN black hole. By comparison, we find that the expressions of the metrics for extremal KN and KM black hole are mathematically identical upon replacements of two corresponding parameters, and so do the observational quantities. We then quote relevant results for the KM case from Ref. [1] and transfer them to the observational quantities for the KN case. We find that the general qualitative features of the hot spot image in the KS case are the same as those in the Kerr spacetime, while quantitative corrections appear when the Sen charge is non-zero. Moreover, the $U(1)$ charges in both KS and KN cases trend to have positively correlated influences on most of the observables, however, the magnitudes are distinguishable.

This chapter is organized as follows. In Sec. 5.2, we review the KS spacetime and the geodesics in this spacetime. In Sec. 5.3, we set up the problem of the observational appearance of an orbiting emitter in the general case. We write down the lens equations to be solved and write down the observational quantities that we are interested in. In Sec. 5.4, we solve this problem for the near-extremal case to the subleading order in the deviation from extremality. In Sec. 5.5, we revisit the KN spacetime and introduce its observational appearance. In Sec. 5.6, we present our results for the KS case with a figure and compare the results with those for the KN case with a table, and we discuss these in detail.

5.2 KERR-SEN BLACK HOLE AND GEODESICS IN KERR-SEN SPACETIME

The KS black hole spacetime is described by a 4-dimensional effective action arising from heterotic string theory:

$$S = -\int d^4x \sqrt{-\mathcal{G}} e^{-\Phi} \Big(-\mathcal{R} + \frac{1}{12}\mathcal{H}^2 - \mathcal{G}^{\mu\nu}\partial_\mu\Phi\partial_\nu\Phi + \frac{1}{8}\mathcal{F}^2 \Big), \tag{226}$$

where $\mathcal{R}$ and Φ are the scalar curvature and the dilation field, respectively, and $\mathcal{F}^2 = \mathcal{F}_{\mu\nu}\mathcal{F}^{\mu\nu}$ with $\mathcal{F}_{\mu\nu}$ being the field strength corresponding to the Maxwell field $\mathcal{A}_\mu$, and

$$\mathcal{H}^2 = \mathcal{H}_{\mu\nu\rho}\mathcal{H}^{\mu\nu\rho}. \tag{227}$$

Here, the expression of $\mathcal{H}_{\mu\nu\rho}$ is of the form

$$\mathcal{H}_{\mu\nu\rho} = \partial_\mu \mathcal{B}_{\nu\rho} + \partial_\nu \mathcal{B}_{\rho\mu} + \partial_\rho \mathcal{B}_{\mu\nu} - \frac{1}{4}\big(\mathcal{A}_\mu \mathcal{F}_{\nu\rho} + \mathcal{A}_\nu \mathcal{F}_{\rho\mu} + \mathcal{A}_\rho \mathcal{F}_{\mu\nu}\big), \tag{228}$$

with $\mathcal{B}_{\mu\nu}$ being an axion field. $\mathcal{G}_{\mu\nu}$ appearing in Eq. (226) are the covariant components of the metric in the string frame, which are related to the Einstein metric by $g_{\mu\nu} = e^{-\Phi}\mathcal{G}_{\mu\nu}$. The Einstein metric, gauge field strength and electromagnetic potential in Boyer-Lindquist coordinates read [81]:

$$\begin{aligned} ds^2 &= -\frac{\Delta}{\Sigma_\alpha}(dt - a\sin^2\theta d\phi)^2 + \frac{\sin^2\theta}{\Sigma_\alpha}(adt - \delta d\phi)^2 + \frac{\Sigma_\alpha}{\Delta}dr^2 + \Sigma_\alpha d\theta^2 \\ &= -\frac{\Delta\Sigma_\alpha}{\Xi}dt^2 + \frac{\Sigma_\alpha}{\Delta}dr^2 + \Sigma_\alpha d\theta^2 + \frac{\Xi\sin^2\theta}{\Sigma_\alpha}(d\phi - \Omega_{\rm bh}dt)^2, \\ \mathbf{H} &= -\frac{2r_\alpha a}{\Sigma_\alpha}dt\wedge d\phi \wedge \big[(r^2 - a^2\cos^2\theta)\sin^2\theta dr - r\Delta\sin 2\theta d\theta\big], \\ \mathbf{A} &= -\frac{Qr}{\Sigma_\alpha}(dt - a\sin^2\theta d\phi), \qquad \Phi = 2\log\sqrt{\frac{\Sigma}{\Sigma_\alpha}}, \end{aligned} \tag{229}$$

where we have defined

$$\begin{aligned} &\Sigma = r^2 + a^2\cos^2\theta, \qquad \Sigma_\alpha = \Sigma + 2r_\alpha r, \\ &\delta = r^2 + a^2 + 2r_\alpha r, \qquad \Delta = \delta - 2Mr, \\ &\Xi = \delta^2 - \Delta a^2\sin^2\theta, \qquad \Omega_{\rm bh} = 2aMr/\Xi. \end{aligned} \tag{230}$$

This Einstein metric describes a KS black hole with mass M, $U(1)$ charge $Q = \sqrt{2Mr_\alpha}$, and angular momentum $J = Ma$ with a and r_α the spin and twist parameters, respectively. The metric reduces to the Kerr geometry when the twist parameter r_α goes to zero. The event horizons are determined by the roots of $\Delta = 0$, as

$$r_\pm = M - r_\alpha \pm \sqrt{(M - r_\alpha)^2 - a^2}, \tag{231}$$

where $r_\pm$ denote the outer and inner horizon, respectively. The regularity of the event horizons requires

$$a \leq M - r_\alpha, \tag{232}$$

and the extremal case is obtained for equality in (232) being taken. When r_α and a are bounded, respectively, we obtain the corresponding ranges for a and r_α as

$$0 \leq a \leq M, \qquad 0 \leq r_\alpha \leq M. \tag{233}$$

Now we consider a particle (including photon) of mass μ moving in the KS spacetime with four-momentum $p^\mu = \left(\frac{\partial}{\partial \tilde{\tau}}\right)^\mu$. Here, $\tilde{\tau}$ is an affine parameter, and for a timelike particle with proper time τ we have $\tilde{\tau} = \tau/\mu$. Then the four-momentum of the particle takes the general form

$$p^\mu = \dot{t}\left(\frac{\partial}{\partial t}\right)^\mu + \dot{r}\left(\frac{\partial}{\partial r}\right)^\mu + \dot{\theta}\left(\frac{\partial}{\partial \theta}\right)^\mu + \dot{\phi}\left(\frac{\partial}{\partial \phi}\right)^\mu, \tag{234}$$

where " $\cdot$ " denotes the derivative with respect to $\tilde{\tau}$. The conserved quantities of a particle along its trajectory are

$$-\mu^2 = g_{\mu\nu} p^\mu p^\nu, \tag{235a}$$

$$E = -g_{\mu\nu} p^\mu \left(\frac{\partial}{\partial t}\right)^\nu = -p_t, \tag{235b}$$

$$L = g_{\mu\nu} p^\mu \left(\frac{\partial}{\partial \phi}\right)^\nu = p_\phi, \tag{235c}$$

$$\mathcal{Q} = p_\theta^2 - \cos^2\theta(a^2 p_t^2 - p_\phi^2 \csc^2\theta) + \mu^2 a^2 \cos^2\theta, \tag{235d}$$

where E is the total energy, L is the angular momentum and $\mathcal{Q}$ is the Carter constant [85]. Using the Hamilton-Jacobi method, we obtain the four-momentum of the particle,

$$\Sigma_\alpha p^t = \frac{\delta}{\Delta}(E\delta - aL) - a(aE\sin^2\theta - L), \tag{236a}$$

$$\Sigma_\alpha p^r = \pm\sqrt{\tilde{\mathcal{R}}(r)}, \tag{236b}$$

$$\Sigma_\alpha p^\theta = \pm\sqrt{\tilde{\Theta}(\theta)}, \tag{236c}$$

$$\Sigma_\alpha p^\phi = \frac{a}{\Delta}(E\delta - aL) - \csc^2\theta(aE\sin^2\theta - L), \tag{236d}$$

where

$$\tilde{\mathcal{R}}(r) = (E\delta - aL)^2 - \Delta\left[\mu(r + 2r_\alpha r) + \mathcal{Q} + (L - aE)^2\right], \tag{237a}$$

$$\tilde{\Theta}(\theta) = \mathcal{Q} - \mu a^2 \cos^2\theta - (L^2 \csc^2\theta - a^2E^2)\cos^2\theta. \tag{237b}$$

The function $\tilde{\mathcal{R}}(r)$ is the radial potential while $\tilde{\Theta}(\theta)$ is the angular potential. The vanishing of these potentials corresponds to the radial and angular turning points in the trajectory, respectively.

5.3 ORBITING EMITTER NEAR KERR-SEN BLACK HOLE

We are interested in an isotropic emitter orbiting on a circular and equatorial geodesic at radius r_s around a KS black hole. For such an emitter, we have $\theta = \pi/2$, $\tilde{\mathcal{R}}(r) = 0$ and $\mathrm{d}\tilde{\mathcal{R}}(r)/\mathrm{d}r = 0$. Solving these radial equations simultaneously for E and L gives

$$\frac{E_\pm}{\mu} = \frac{(r + r_\alpha)^{1/2}(r - 2M + 2r_\alpha) \pm aM^{1/2}}{(r + 2r_\alpha)^{1/2}P^{1/2}}, \tag{238a}$$

$$\frac{L_\pm}{\mu} = \frac{\pm M^{1/2}[r(r + 2r_\alpha) \mp 2aM^{1/2}(r + r_\alpha)^{1/2} + a^2]}{(r + 2r_\alpha)^{1/2}P^{1/2}}, \tag{238b}$$

where

$$P = r^2 - (3r + 2r_\alpha)(M - r_\alpha) \pm 2aM^{1/2}(r + r_\alpha)^{1/2}. \tag{239}$$

Note that the existence of circular orbits requires that the denominator of Eqs. (238) is real, i.e.,

$$(r + 2r_\alpha)P > 0. \tag{240}$$

Combining Eqs. (236) and (238) we obtain the coordinate angular velocity of the emitter,

$$\Omega_s \equiv \frac{d\phi}{dt} = \frac{\pm M^{1/2}}{(r + 2r_\alpha)(r + r_\alpha)^{1/2} \pm aM^{1/2}}. \tag{241}$$

The upper and lower sign in these formulae denote the direct and retrograde orbits, respectively. Here and hereafter, we use the subscript s to represent the "source".

5.3.1 *Photon motion and lens equations*

For a photon trajectory, we have $\mu = 0$ in the geodesic equations (236). In this case, the energy E may be scaled out from these equations and it is convenient to introduce two new dimensionless parameters

$$\hat{\lambda} = \frac{L}{E}, \quad \hat{q} = \frac{\sqrt{\mathcal{Q}}}{E}, \tag{242}$$

to describe this photon trajectory. Note that we will always have positive and real $\hat{q}$ for all trajectories that intersect the equatorial plane since $\mathcal{Q} = p_\theta^2 \geq 0$. In terms of the new parameters, the potentials (237) for the null case can be written as

$$\mathcal{R}(r) = \frac{\tilde{\mathcal{R}}(r)}{E^2} = (a\hat{\lambda} - \delta)^2 - \Delta\left[\hat{q}^2 + (\hat{\lambda} - a)^2\right], \tag{243a}$$

$$\Theta(\theta) = \frac{\tilde{\Theta}(\theta)}{E^2} = \hat{q}^2 - (\hat{\lambda}^2 \csc^2\theta - a^2)\cos^2\theta. \tag{243b}$$

Integrating up the geodesic equations (236) for a photon trajectory from a source $(t_s, r_s, \theta_s, \phi_s)$ to an observer $(t_o, r_o, \theta_o, \phi_o)$, we obtain

$$⨍_{r_s}^{r_o} \frac{dr}{\pm\sqrt{\mathcal{R}(r)}} = ⨍_{\theta_s}^{\theta_o} \frac{d\theta}{\pm\sqrt{\Theta(\theta)}}, \tag{244a}$$

$$\Delta\phi = \phi_o - \phi_s = ⨍_{r_s}^{r_o} \frac{a}{\pm\Delta\sqrt{\mathcal{R}(r)}}\left(2Mr - a\hat{\lambda}\right)dr + ⨍_{\theta_s}^{\theta_o} \frac{\hat{\lambda}\csc^2\theta}{\pm\sqrt{\Theta(\theta)}}d\theta, \tag{244b}$$

$$\Delta t = t_o - t_s = ⨍_{r_s}^{r_o} \frac{dr}{\pm\Delta\sqrt{\mathcal{R}(r)}}\left(\delta^2 - a^2\Delta - 2aMr\hat{\lambda}\right) + ⨍_{\theta_s}^{\theta_o} \frac{a^2\cos^2\theta}{\pm\sqrt{\Theta(\theta)}}d\theta, \tag{244c}$$

Here and hereafter, we use the subscript o to denote the "observer". We use the slash notation to distinguish different light rays connecting the two points. That is, the integrals are to be evaluated as path integrals along each trajectory, and there appears a turning point in the trajectory every time when the effective potentials satisfy $\mathcal{R}(r) = 0$ or $\Theta(\theta) = 0$. Next, we introduce new parameters b, m and s to tell the different photon trajectories apart. For the r direction, we use $b = 0$ for those direct trajectories with no radial turning point and $b = 1$ for those reflected trajectories with one radial turning point. For the θ direction, we apply $m \geq 0$ to denote the number of angular turning points and let $s = \pm 1$ depict the final sign of p_θ (final polar orientation of the light ray). Then the trajectory equations (244) can be rewritten as the "KS lens equations",

$$I_r + b\tilde{I}_r = G_\theta^{m,s}, \tag{245a}$$

$$J_r + b\tilde{J}_r + \frac{\hat{\lambda}G_\phi^{m,s} - \Omega_s a^2 G_t^{m,s}}{M} = -\Omega_s t_o + 2\pi N, \tag{245b}$$

where we have used $\phi_s = \Omega_s t_s$ to decouple t_s from these equations and set $\phi_o = 2\pi N$ for an integral N, and I_r, $\tilde{I}_r$, J_r, $\tilde{J}_r$, and $G_i^{m,s}$ $(i \in \{t, \theta, \phi\})$ are the radial and angular integrals given in Appendices A and B, which are defined in the same way as in Ref. [5].

5.3.2 *Observational appearance*

We now consider the observational appearance of the point emitter following Refs. [90, 46, 5]. The observables are the images positions, redshift factors and fluxes which can be expressed in terms of the conserved quantities $\hat{\lambda}$ and $\hat{q}$ [Eq. (242)].

The apparent position (α, β) of images on the observer's screen is obtained as

$$\alpha = -\frac{\hat{\lambda}}{\sin\theta_o}, \tag{246a}$$

$$\beta = s\sqrt{\hat{q}^2 + a^2\cos^2\theta_o - \hat{\lambda}^2\cot^2\theta_o} = s\sqrt{\Theta(\theta_o)}, \tag{246b}$$

where $s \in \{-1, 1\}$ denotes the final sign of p_θ at the observer, which represents whether the light ray arrives from above or below.

The redshift factor g is obtained as

$$g = \frac{E}{E_s} = \frac{1}{\gamma}\sqrt{\frac{\Delta_s\Sigma_{\alpha s}}{\Xi_s}}\frac{1}{1 - \Omega_s\hat{\lambda}}, \tag{247}$$

where the boost factor γ is defined as

$$v_s = \frac{\Xi_s}{\Sigma_{\alpha s}\sqrt{\Delta_s}}[\Omega_s - \Omega_{\rm bh}(r_s)], \quad \gamma = \frac{1}{\sqrt{1 - v_s^2}}. \tag{248}$$

The normalized flux (comparing to the "Newtonian flux" F_N) F_o/F_N is given by (see App. C)

$$\frac{F_o}{F_N} = \frac{g^3 M \Sigma_{\alpha s}}{\gamma \sin\theta_o} \sqrt{\frac{\Delta_s}{\Xi_s \Theta(\theta_o) \mathcal{R}(r_s)}} \left| \det \frac{\partial(B, A)}{\partial(\hat{\lambda}, \hat{q})} \right|^{-1}, \tag{249}$$

where we have defined

$$A \equiv I_r + b\tilde{I}_r - G_\theta^{m,s} \pm M \int_{\pi/2}^{\theta_s} \frac{d\theta}{\sqrt{\Theta(\theta)}}, \tag{250a}$$

$$B \equiv J_r + b\tilde{J}_r + \frac{\hat{\lambda} G_\phi^{m,s} - \Omega_s a^2 G_t^{m,s}}{M}. \tag{250b}$$

Note that computing the flux involves a variation with regard to θ_s, thus we have generalized the lens equations (245) to allow $\theta_s \neq \pi/2$. The plus or minus sign in Eq. (250a) corresponds to pushing the emitter above or below the source plane $\theta_s = \pi/2$.

Like in the KM case [1], these observables (246), (247) and (249) also have same form as those of the Kerr case, while the differences come from the specific expressions for Ξ_s, $\Sigma_{\alpha s}$, Δ_s, Ω_{bh} and Ω_s.

5.4 NEAR-EXTREMAL EXPANSION

So far, we have set up the problem for the most general case. However it is not easy to analytically compute the emission signals for most of the situations, therefore, we will only consider the case of an emitter orbiting on, or near, the direct ISCO of a near-extremal KS black hole (as was suggested in Ref. [5]). Without loss of generality, we will choose $r_o \to \infty$ and $\theta_o \in (0, \pi/2)$ to put the observer at a distant position in the northern celestial sphere. For simplicity, we introduce a dimensionless radial coordinate R, which is defined through the Boyer-Lindquist radius r by

$$R = \frac{r - (M - r_\alpha)}{M} = \frac{r - M(1 - \tilde{r}_\alpha)}{M}, \tag{251}$$

where we have introduced the reduced twist parameter $\tilde{r}_\alpha = r_\alpha / M$. In addition, a small parameter ϵ is also introduced to describe the deviation of the KS black hole from extremity,

$$a = M(1 - \tilde{r}_\alpha)\sqrt{1 - \epsilon^3}, \tag{252}$$

The ISCO of a general KS can be obtained by following the standard procedure given in Ref. [83] and the leading order result in the near-extremal limit is obtained as

$$R_{\text{ISCO}} = \bar{R}\epsilon + \mathcal{O}(\epsilon^2), \tag{253}$$

where

$$\bar{R} = 2^{1/3}(1-\tilde{r}_\alpha)^{1/3}.$$

Thus, to the leading order in ϵ, we put the emitter on the orbit with radius

$$r_s = M(1-\tilde{r}_\alpha + \epsilon\bar{R}). \tag{254}$$

Following Refs. [5, 4], it is convenient to introduce two new quantity λ and q which are related to the parameters $\hat{\lambda}$ and $\hat{q}$ by

$$\hat{\lambda} = 2M(1-\epsilon\lambda), \quad \hat{q} = M\sqrt{(1-\tilde{r}_\alpha)(3+\tilde{r}_\alpha)-q^2}. \tag{255}$$

For later reference, we now expand the orbital frequency Ω_s and period T_s in ϵ and obtain

$$\Omega_s = \frac{1}{2M} + \mathcal{O}(\epsilon), \qquad T_s = \frac{2\pi}{\Omega_s} = 4\pi M + \mathcal{O}(\epsilon). \tag{256}$$

To the leading order in the deviation of near-extremality, the orbital frequency remains unchanged for the KS case compared to that of the Kerr case, which is different from the KM [1] and KN (Sec. 5.5) cases.

5.4.1 *Near-extremal solutions*

Now we solve the KS lens equations (245) in the near-extremal limit and express the solutions (λ, q) as functions of observer's time t_o.

5.4.1.1 *First equation*

We start with the first equation (245a),

$$I_r + b\tilde{I}_r = mG_\theta - s\hat{G}_\theta. \tag{257}$$

The I integrals (radial) and G integrals (angular) are performed in the Appendices. The results for the radial integrals are given by

$$I_r = \frac{1}{q}\log\left[\frac{4q^4 R_o}{(qD_o + q^2 + 2R_o)(qD_s + q^2\bar{R} + 4(1-\tilde{r}_\alpha)\lambda)}\right] \\ -\frac{1}{q}\log\epsilon + \mathcal{O}(\epsilon), \tag{258a}$$

$$\tilde{I}_r = \frac{1}{q}\log\left[\frac{(qD_s + q^2\bar{R} + 4(1-\tilde{r}_\alpha)\lambda)^2}{4(1-\tilde{r}_\alpha)^2(4-q^2)\lambda^2}\right] + \mathcal{O}(\epsilon), \tag{258b}$$

where

$$D_s = \sqrt{q^2\bar{R}^2 + 8(1-\tilde{r}_\alpha)\lambda\bar{R} + 4(1-\tilde{r}_\alpha)^2\lambda^2}, \tag{259}$$

$$D_o = \sqrt{q^2 + 4R_o + R_o^2}. \tag{260}$$

The results for the angular integrals are given by elliptic functions which to the desired order are some explicit functions of q.

We will introduce the main steps for solving this equation and refrain from giving detailed calculation since a similar calculation can be found in Ref. [5].

First, we introduce two quantities $\bar{m}$ and $\Upsilon > 0$ for convenience, which are defined by

$$m = -\frac{1}{qG_\theta}\log\epsilon + \bar{m}, \tag{261}$$

$$\Upsilon \equiv \frac{q^4 R_o}{q^2 + 2R_o + qD_o} e^{-qG_\theta^{\bar{m},s}}. \tag{262}$$

The logarithmic term in Eq. (261) is introduced to compensate for the corresponding term in left-hand-side of Eq. (257).

Next, we can rewrite the first lens equation (257) in a simplified form by using (261) and (262), which leads to a quadratic equation in λ. Solving this quadratic equation for $b = 0$ and $b = 1$, separately, we obtain the final result as

$$\lambda = \frac{2\Upsilon}{(1-\tilde{r}_\alpha)(4-q^2)}\left[2 - q\sqrt{1 + \frac{4-q^2}{2\Upsilon}\bar{R}}\right]. \tag{263}$$

In addition, the conditions for the solution to exist are obtained as

$$\bar{R} < \frac{4\mathrm{Y}}{q^2}\left(1+\frac{2}{\sqrt{4-q^2}}\right) \quad \text{if} \quad b=0, \tag{264a}$$

$$\bar{R} > \frac{4\mathrm{Y}}{q^2}\left(1+\frac{2}{\sqrt{4-q^2}}\right) \quad \text{if} \quad b=1. \tag{264b}$$

We observe that the first equation (257) does not include in explicity the time t_o. Thus, for given choice of m, s, and b, we have arrived at a function $\lambda(q)$ [Eq. (263)] with the supplementary conditions (264).

5.4.1.2 *Second equation*

From the second equation (245b) we will get another another relation between t_o, λ, and q for given choice of m, s, and b. For convenience, we introduce a dimensionless time coordinate $\hat{t}_o$ restricted to a single period $\hat{t}_o \in [0,1]$,

$$\hat{t}_o = \frac{t_o}{T_s} = \frac{t_o}{4\pi M} + \mathcal{O}(\epsilon). \tag{265}$$

We can then rewrite Eq. (245b) as

$$\hat{t}_o = N + \mathcal{G},\ \mathcal{G} = -\frac{1}{2\pi}\Big(J_r + b\tilde{J}_r + 2G_\phi^{m,s} - \frac{(1-\tilde{r}_\alpha)^2}{2}G_t^{m,s}\Big), \tag{266}$$

where J integrals and G integrals are given in the Appendices. The J integrals have similar structures as the I integrals [Eq. (258)] and G integrals are functions of q to the desired order. Recalling Eq. (263), we can then conclude that Eq. (266) gives a function

$$\hat{t}_o(q) = \hat{t}_o[q, \lambda(q)] \tag{267}$$

for a given choice of m, s, b with a non-vanishing range of q. Note also that in the given period of $\hat{t}_o \in [0,1]$, N is uniquely determined.

For each allowed value of N, inverting Eq. (267) in each monotonic domain gives an inverse $q_i(\hat{t}_o)$ with i a discrete integral labeling it. We know from Sec. 5.3.2 that the observables of a hot spot's image can be written as functions of λ and q, therefore, each function $q(\hat{t}_o)$ corresponds to an image track segment labeled by (m, b, s, N, i).

5.4.2 *Observational quantities*

In this subsection, we will expand the observables, including the position (246), the redshift factor (247) and the flux (249), in ϵ and pick up the leading piece. Recall from the beginning of Sec. 5.4, we have the near-extremal KS expansions

$$
\begin{aligned}
a = M(1-\tilde{r}_\alpha)\sqrt{1-\epsilon^3}, \quad r_s = M(1-\tilde{r}_\alpha+\epsilon\bar{R}), \\
\hat{\lambda} = 2M(1-\epsilon\lambda), \quad \hat{q} = M\sqrt{(1-\tilde{r}_\alpha)(3+\tilde{r}_\alpha)-q^2}.
\end{aligned} \tag{268}
$$

By expanding Eq. (246), the image position on the observer's screen is obtained as

$$
\alpha = -\frac{2M}{\sin\theta_o} + \mathcal{O}(\epsilon), \tag{269a}
$$

$$
\begin{aligned}
\beta = sM\Big[3-q^2+\cos^2\theta_o-4\cot^2\theta_o \\
-\tilde{r}_\alpha(3+\cos 2\theta_o+\tilde{r}_\alpha\sin^2\theta_o)\Big]^{1/2}+\mathcal{O}(\epsilon).
\end{aligned} \tag{269b}
$$

Note that the leading order position does not depend on λ and the leading order coordinate α has the same form as in the Kerr case. The other screen coordinate β being real gives a range of q,

$$
q \in \left[0, \sqrt{3+\cos^2\theta_o-4\cot^2\theta_o-\tilde{r}_\alpha(3+\cos 2\theta_o+\tilde{r}_\alpha\sin^2\theta_o)}\right].
$$

The boundary values of q corresponds to two endpoints of a vertical line (the analogue of NHEK line [5]), out of which the image disappears since β is no longer real. For an observer being able to see the image, the inclination is required to be in the range of $\theta_{\rm crit} < \theta_o < \pi - \theta_{\rm crit}$, where

$$
\theta_{\rm crit} = \arctan\left[\frac{2}{\sqrt{2\sqrt{3-2\tilde{r}_\alpha}-2\tilde{r}_\alpha}}\right]. \tag{270}
$$

Next, the redshift factor (247) is expanded as

$$g = \frac{\sqrt{(1+\tilde{r}_\alpha)(3+\tilde{r}_\alpha)}}{(3+\tilde{r}_\alpha)+4\frac{\lambda}{\bar{R}}} + \mathcal{O}(\epsilon). \tag{271}$$

The normalized image flux (249) is expanded as,

$$\frac{F_o}{F_N} = \frac{\sqrt{1+\tilde{r}_\alpha}\bar{R}\epsilon}{2\sqrt{1-\tilde{r}_\alpha}D_s} \frac{qg^3}{\sin\theta_o\sqrt{1-\frac{q^2}{3-2\tilde{r}_\alpha-\tilde{r}_\alpha^2}}\sqrt{\Theta_0(\theta_o)}} \left|\det\frac{\partial(B,A)}{\partial(\lambda,q)}\right|^{-1}, \tag{272}$$

where g is given in Eq. (271) and D_s is given in Eq. (259), and [see Eq. (269)]

$$\begin{aligned}\Theta_0(\theta_o) &= [\Theta(\theta_o)/M^2]|_{\lambda=0} = \beta^2/M^2 \\ &= 3-q^2+\cos^2\theta_o - 4\cot^2\theta_o - \tilde{r}_\alpha(3+\cos 2\theta_o+\tilde{r}_\alpha\sin^2\theta_o),\end{aligned} \tag{273}$$

and from the definitions of A and B [Eq. (250)], we have

$$\begin{aligned}\left|\det\frac{\partial(B,A)}{\partial(\lambda,q)}\right| = &\left|\frac{\partial}{\partial\lambda}\left(J_r+b\tilde{J}_r\right)\left[\frac{\partial}{\partial q}\left(I_r+b\tilde{I}_r\right)-\frac{\partial G_\theta^{m,s}}{\partial q}\right]\right. \\ &\left.-\frac{\partial}{\partial\lambda}\left(I_r+b\tilde{I}_r\right)\left[\frac{\partial}{\partial q}\left(J_r+b\tilde{J}_r\right)+\frac{\partial G_{t\phi}^{m,s}}{\partial q}\right]\right| + \mathcal{O}(\epsilon\log\epsilon),\end{aligned} \tag{274}$$

where we have introduced

$$G_{t\phi}^{m,s} = \left(\hat{\lambda}G_\phi^{m,s} - \Omega_s a^2 G_t^{m,s}\right)/M = 2G_\phi^{m,s} - \frac{(1-\tilde{r}_\alpha)^2}{2}G_t^{m,s} + \mathcal{O}(\epsilon). \tag{275}$$

The G, I, J integrals are given in Appendices A and B.

5.5 KERR-NEWMAN BLACK HOLE REVISITED AND ITS OBSERVATIONAL SIGNATURE

A useful reference for understanding the charged black hole in string theory (the KS black hole) is its counter partner in GR (the KN black hole). Therefore, here we briefly review the KN metric and revisit it from a mathematical comparison with the KM metric. We do the later comparison because the observational signature of a near-extremal KM black hole have been studied in Ref. [1] and we will see from below that the expressions for the near-extremal KM case can be applied to the near-extremal KN case upon replacements of the corresponding parameters in the metrics. We will use subscript ‘KN’ for physical charges of KN spacetime and we will use subscipt ‘KM’ for those of KM spacetime. Charges without subscript are for KS spacetime.

The KN metric is a stationary solution of the Einstein-Maxwell theory, which in Boyer-Lindquist coordinates reads

$$\begin{aligned} ds^2 =& -\frac{\Delta_{\rm KN}}{\Sigma_{\rm KN}}\left(dt - a_{\rm KN}\sin^2\theta d\phi\right)^2 + \frac{\Sigma_{\rm KN}}{\Delta_{\rm KN}}dr^2 \\ &+\Sigma_{\rm KN}d\theta^2 + \frac{\sin^2\theta}{\Sigma_{\rm KN}}\left[a_{\rm KN}dt - (r^2 + a_{\rm KN}^2)d\phi\right]^2, \end{aligned} \tag{276}$$

where

$$\Sigma_{\rm KN} = r^2 + a_{\rm KN}^2\cos^2\theta, \quad \Delta_{\rm KN} = r^2 - 2M_{\rm KN}r + a_{\rm KN}^2 + Q_{\rm KN}^2, \tag{277}$$

with $a_{\rm KN}$, $M_{\rm KN}$, and $Q_{\rm KN}$ being the spin, mass, and $U(1)$ charge of the black hole. For later reference, we may define a reduced charge parameter $\tilde{Q}_{\rm KN} = Q_{\rm KN}/M_{\rm KN}$. When $Q_{\rm KN} = 0$, this metric reduce to the Kerr black hole. The extremal limit for KN black hole is obtained for

$$a_{\rm KN}^2 = M_{\rm KN}^2 - Q_{\rm KN}^2. \tag{278}$$

For a comparison of the KS metric and KN metric from the action level and a comparison of their apparent shapes, readers may refer to Ref. [146].

Next, we introduce the KM metric which is a stationary solution of the scalar-tensor-vector (STVG) modified gravitational (MOG) theory. We will restore the Newtonian constant G_N to describe the KM metric for the reason that will become clear below. The KM metric in Boyer-Lindquist coordinates reads

$$\begin{aligned} ds^2 =& -\frac{\Delta_{\rm KM}}{\Sigma_{\rm KM}}\left(dt - a_{\rm KM}\sin^2\theta d\phi\right)^2 + \frac{\Sigma_{\rm KM}}{\Delta_{\rm KM}}dr^2 \\ &+\Sigma_{\rm KM}d\theta^2 + \frac{\sin^2\theta}{\Sigma_{\rm KM}}\left[a_{\rm KM}dt - (r^2 + a_{\rm KM}^2)d\phi\right]^2, \end{aligned} \tag{279}$$

where

$$\Sigma_{\rm KM} = r^2 + a_{\rm KM}^2\cos^2\theta, \quad \Delta_{\rm KM} = r^2 - 2M_\chi r + a_{\rm KM}^2 + Q_\chi^2, \tag{280}$$

with

$$M_\chi = G_N(1+\chi)M_{\mathrm{KM}}, \qquad Q_\chi^2 = \frac{\chi}{1+\chi}M_\chi^2. \tag{281}$$

Here, M_{KM} and a_{KM} are mass and spin parameters of the black hole and χ is the deformation parameter defined by $G = G_N(1+\chi)$ with G being an enhanced gravitational constant. Moreover, M_χ and $J = M_\chi a_{\mathrm{KM}}$ are, respectively, the ADM mass and angular momentum of the KM metric [139]. In addition, $K = \sqrt{\chi G_N}M_{\mathrm{KM}}$ is defined as the gravitational charge of the MOG vector field and Q_χ in (281) is a parameter related to this charge. Note that, unlike the $U(1)$ charges of the KS and KN black holes which are independent from their masses, this gravitational charge in the MOG theory is mass-dependent. The extremal limit for KM black hole is obtained for

$$a_{\mathrm{KM}}^2 = M_\chi^2 - Q_\chi^2. \tag{282}$$

As briefly introduced above, the physical starting points of the KN and KM metrics and their interpretations are both quite different. Nevertheless, it is interesting that the KN metric (276) and the KM metric (279) have very similar mathematical forms of their expressions. We will interpret M_χ as the mass of the KM black hole as suggested in Ref. [139] corresponding to M_{KN} in the KN black hole, then the only difference between these metrics comes from the mass-dependencies of their charge parameters. Furthermore, this difference become irrelevant in the expressions for the (near-)extremal cases due to the constraints (278) and (282). In those cases, we may mathematically identify the KN metric and KM metric upon $M_{\mathrm{KN}} \to M_\chi$ and $Q_{\mathrm{KN}} \to Q_\chi$. As have been shown in the previous sections (as well as in Refs. [5, 1]) that the computations for the observables of an orbiting emitter on the ISCO of a near-extremal rotating black hole only rely on the spacetime metric and the geodesics in it. Therefore, the results in Ref. [1] for the KM case can be applied to the KN case upon to the replacements: $M_\chi \to M_{\mathrm{KN}}$ and $Q_\chi[= (M_\chi^2 - a_{\mathrm{KM}}^2)^{1/2}] \to Q_{\mathrm{KN}}$. Note that in Ref. [1] it has set $M_\chi = 1$ and used spin a_{KM} to represent the modified parameter χ due to the relations (281) and (282). To be specific, the near-extremal KM cases for $a_{\mathrm{KM}} = 1$, 0.8 and

0.717 correspond to the near-extremal KN cases for $\tilde{Q}_{\text{KN}} = 0$, 0.6 and 0.7. As a particular and representative example to be compared with the corresponding KS case, we will discuss the KN case for $\tilde{Q}_{\text{KN}} = 0.6$ in Sec. 5.6, for which we have borrowed the results of the KM one for $a_{\text{KM}} = 0.8$ from Ref. [1].

5.6 RESULTS AND DISCUSSION

Now we discuss the results of the observables in practical, we will make the following choices for the physical parameters,

$$\begin{aligned} R_o &= 100, \qquad \theta_o = 84.27^\circ, \\ \epsilon &= 0.01, \qquad \bar{R} = \bar{R}_{\text{ISCO}} = 2^{1/3}\left(1 - \tilde{r}_\alpha^2\right)^{1/3}. \end{aligned} \tag{283}$$

In addition, for the reduced twist parameter $\tilde{r}_\alpha$, we will restrict ourself to a range from 0 to 0.5. As mentioned before, the $\tilde{r}_\alpha = 0$ case reduce to the Kerr one. While we take the upper bound $\tilde{r}_\alpha = 0.5$ corresponding to the $U(1)$ charge $Q = M$, since the charge for an astrophysical black hole is supposed to be quite small. (Note also, from Sec. 5.5, that the Kerr-Newman metric with a non-zero spin and a $U(1)$ charge $Q_{\text{KN}} = M_{\text{KN}}$ represents a naked singularity whose apparent shape has been studied in Ref. [146].) Thus, we have set up a hot spot on the ISCO of a near-extremal KS black hole with a charge Q ranging from 0 to M, viewed by a distant observer from a nearly edge-on inclination.

Moreover, we will compare the results for KS black hole with those for other charged rotating black holes (the KN and KM black holes). The result for KM case can be found in Ref. [1] and the result for KN case is introduced in Sec. 5.5.

The main observables of the hot spot image in near-extremal KS spacetime are given in Sec. 5.3.2, which are the apparent position (α, β) (269), the redshift factor g (271) and the normalized flux

F_o/F_N (272). The complete information of the image consists of tracks which are lined up by the track segments labeled by (m, b, s, N, i). Next, we will illustrate the feature of these observables for several selected brightest images.

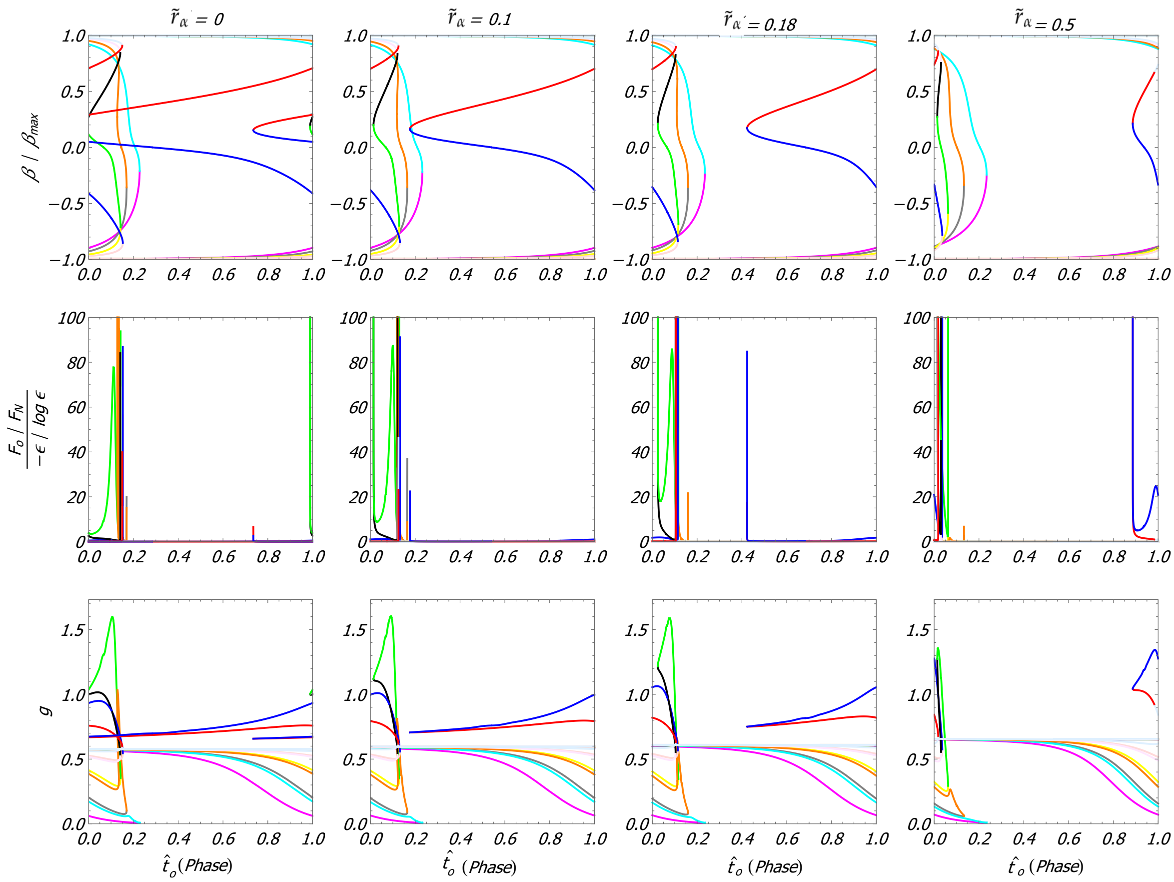

Figure 19.: Apparent positions, normalized fluxes and redshift factors of the brightest few images of the hot spot for the twist parameter $\tilde{r}_\alpha = 0$ (Kerr case), 0.1, 0.18 ($Q = 0.6M$) and 0.5 ($Q = M$). We have depicted each continuous image track by the same color following Ref. [5]. each of these continuous image tracks consists of several track segments labeled by (m, b, s, N, i).

In Fig. 19, we show the main observables of these selected brightest images in a single period for the reduced twist parameter $\tilde{r}_\alpha = 0, 0.1, 0.18$, and 0.5, respectively. Note that we choose the specific value of $\tilde{r}_\alpha = 0.18$ because it corresponds to the Sen charge $Q = 0.6M$, which will be compared, as a representative example, with the KN case for the KN charge $Q_{\mathrm{KN}} = 0.6M_{\mathrm{KN}}$. For each $\tilde{r}_\alpha$, each graph has several different colored lines of which the green one represents the primary image while the others indicate the secondary images. The secondary images are much fainter than the primary image apart from near caustics (where lines with different colors intersect). The general features of the primary image (which moves on a vertical line while blueshifts and peaks in brightness) and the secondary images (which also move on the vertical line with a typical caustic structure) are the same as those for the Kerr case [5]. Note that the graphs for $\tilde{r}_\alpha = 0$ agree exactly with [5] which is no surprise since the KS metric reduce to the Kerr metric in that case. However, when $\tilde{r}_\alpha \neq 0$, the KS case displays quantitatively corrections to the kerr case and also has differences from the KM (KN) case [1]. Regarding to the apparent position (269), the screen coordinate α stays unchanged when $\tilde{r}_\alpha$ is varied, while the maximum value of the other screen coordinate β decreases when $\tilde{r}_\alpha$ is increased from 0 (corresponding to $\beta_{\max} = 1.72M$) to 0.5 (corresponding to $\beta_{\max} = 1.31M$). From the middle line we see that the energy flux increases when $\tilde{r}_\alpha$ is increased. From the bottom line we see that, when $\tilde{r}_\alpha$ is increased, the peak redshift factor associated with the primary image stays around 1.6 (except for $\tilde{r}_\alpha = 0.5$) while the typical redshift factor (corresponding to $\lambda \sim 0$) associated with the secondary images increases. To be specific, one can obtain this typical redshift factor from Eq. (271), as $g = \sqrt{(1+\tilde{r}_\alpha)/(3+\tilde{r}_\alpha)}$. The astronomical observed iron line [92] might suppose to be shifted by these factors. Unfortunately, comparing with the predicted value in the Kerr case [5], the results obtained in the KS cases are further away from the observed value. These observational signatures appear periodically and the period in KS cases stay unchanged when $\tilde{r}_\alpha$ is varied. In addition, as in the Kerr case, these signatures are strongest when the inclination angle $\theta_o \approx 90^\circ$ (i.e., the edge-on case) and will vanish when the inclination θ_o less than a critical value θ_{crit} [see Eq. (270)]. In the KS cases, this critical inclination is increased from 47° to 56° when $\tilde{r}_\alpha$ is increased from 0 to 0.5.

Furthermore, now we illustrate the representative example for the observational signatures of near-extremal KS/KN black holes both with the same $U(1)$ charge $Q_{(\mathrm{KN})} = 0.6M_{(\mathrm{KN})}$. As mentioned before, this corresponds to the reduced twist parameter $\tilde{r}_\alpha = 0.18$ for the KS case. The results for the KN case can be obtained from a comparison with the KM case [1] which has a mass-dependent charge (see Sec. 5.5). We find that, in KS and KN cases, the charges $Q_{(\mathrm{KN})}$ trend to have positively correlated influences on most of the observables and these observables are corrected more in the KN case. However, the screen coordinate α and the period T_s in the KS case stay unchanged but they both are corrected in the KN case. We show these results explicitly in Table 2.

	Kerr	KS	KN
Q	0	0.6M	0.6M
α	$-20M$	$-20M$	$-20.53M$
$\beta_{\max}$	$1.72M$	$1.60M$	$1.55M$
g_{peak}	1.6	1.6	1.6
$g_{\lambda\sim 0}$	0.58	0.61	0.64
T_s	$4\pi M$	$4\pi M$	$4.1\pi M$
θ_{crit}	47.06°	49.66°	51.35°

Table 2.: Some typical quantities for the near-extremal KS and KN black hole both with a $U(1)$ charge $Q = 0.6M$ ($Q_{\mathrm{KN}} = 0.6M_{\mathrm{KN}}$) and the corresponding quantities for the neutral Kerr case.

6

SUMMARY AND OUTLOOK

In this thesis we analytically computed the optical appearance of high-spin black holes with accompanying hot spots in their near-horizon regions, with regard to the current and future EHT observations. While the standard studies in the literatures were based on the framework of GR and usually neglected the propagating effects of light, here we considered a broader set of possibilities and sought for alternative templates for the EHT to test. We computed the apparent boundaries (critical curves) of such black holes which are relevant to the current EHT observations. We also computed the observables of the hot spots which provides striking predictions for future EHT to test. The differences between the observational signatures predicted in GR and in alternative gravity theories present another way for testing gravity theories in their strong field regimes.

To date, the first EHT image has confirmed the most important feature of the appearance of a black hole: a bright photon ring surrounding a central dark shadow. However, GR predicts much richer substructures of this bright ring than the current image can resolve. With ongoing efforts, an image with sufficient resolution to recognize these substructures will hopefully be achieved in the future. Therefore, it would be not only theoretically interesting but also practically relevant to explore more on the optical appearance of black holes. Possible further directions include:

- Analytical theory of the photon ring [39][149] and universal substructures of the photon ring (interferometric signatures [32] and polarimetric signatures [150]) based on GR, as well as their generalizations to alternative theories of GR.

- Broadening of an emission line from the innermost part of an accretion disk surrounding a near-extremal rotating black hole [55] in alternative theories of GR.

- Optical appearance of a plunging source [49]—final images of an plunging source before it drops into the black hole.

- Black holes and hot spots viewed by an observer at finite distance [42], or by a comoving observer with cosmic expansion [151].

A

RADIAL INTEGRALS

In this appendix, we deal with the radial integrals appearing in the lens equations in the main body of the text [Eq. (66) for Kerr in vacuum, Eq. (134) for Kerr in a plasma, Eq. (184) for KM and Eq. (245) for KS]. These integrals in the different cases are defined in a similar way as [5]

$$I_r = M\int_{r_s}^{r_o} \frac{dr}{\sqrt{\mathcal{R}(r)}}, \quad \tilde{I}_r = 2M\int_{r_{\min}}^{r_s} \frac{dr}{\sqrt{\mathcal{R}(r)}}, \tag{284a}$$

$$J_r = \int_{r_s}^{r_o} \frac{\mathcal{J}_r}{\sqrt{\mathcal{R}(r)}}dr, \quad \tilde{J}_r = 2\int_{r_{\min}}^{r_s} \frac{\mathcal{J}_r}{\sqrt{\mathcal{R}(r)}}dr. \tag{284b}$$

Here, $\mathcal{R}(r)$ and $\mathcal{J}_r$ are taken differently for the corresponding cases and explicit expressions will be given in the following. $r_{\min}$ is the largest real root of $\mathcal{R}(r)$ satisfying $r_{\min} < r_s$. Note that, for the KM case, M in the first line of the equations is replaced by M_χ.

In general, these integrals are computed numerically. Here, we will compute them analytically by using the method of matched asymptotic expansion (MAE) in the near-extremal limit [4, 5]. First, we review the two examples from the vacuum Kerr case for the computations of these integrals [5]; the MAE method is applied to the first example while the second example is done for an integral only in the near-horizon region. The other radial integrals can be computed in the same way. Then, we list the results for each of these cases.

First example.

We compute the first integral in Eqs. (284a). For convenience, we repeat it here:

$$I_r = M \int_{r_s}^{r_o} \frac{dr}{\sqrt{\mathcal{R}(r)}}, \quad \mathcal{R}(r) = \left(r^2 + a^2 - a\hat{\lambda}\right)^2 - \left(r^2 - 2Mr + a^2\right)\left[\hat{q}^2 + \left(a - \hat{\lambda}\right)^2\right]. \tag{285}$$

For the near-extremal Kerr black hole, we have

$$a = M\sqrt{1-\epsilon^3}, \qquad r_s = 1 + \epsilon\bar{R}, \qquad \hat{\lambda} = 2M(1+\epsilon\lambda), \qquad \hat{q} = \sqrt{3-q^2} \tag{286}$$

It is convenient to use the dimensionless radial coordinate $R = (r-M)/M$. We then introduce two constants $0 < p < 1$ and $C > 0$ and rewrite the integral as

$$I_r = M^2 \int_{\epsilon\bar{R}}^{\epsilon^p C} \frac{dR}{\sqrt{\mathcal{R}}} + M^2 \int_{\epsilon^p C}^{R_o} \frac{dR}{\sqrt{\mathcal{R}}}. \tag{287}$$

As $\epsilon \to 0$, the scaling of ϵ^p introduces a separation of scales for the two pieces of integrals since $\epsilon \ll \epsilon^p \ll 1$. The first piece of integral is in the near-horizon region $R \sim \epsilon$ and the second piece is in the far region $R \sim 1$.

In the near-horizon region, we introduce a new variable $\tilde{R} = R/\epsilon$ and expand the first piece of integral in ϵ at fixed $\tilde{R}$. Then we have

$$\begin{aligned} M^2 \int_{\epsilon\bar{R}}^{\epsilon^p C} \frac{dR}{\sqrt{\mathcal{R}}} &= M^2 \int_{\bar{R}}^{\epsilon^{p-1}C} \left(\frac{1}{\sqrt{q^2\tilde{R}^2 + 8\lambda\tilde{R} + 4\lambda^2}} + \mathcal{O}(\epsilon)\right) d\tilde{R} \\ &= \frac{1}{q}\log\left[\frac{2q^2}{qD_s + q^2\bar{R} + 4\lambda} + (p-1)\log\epsilon + \log C\right] + \mathcal{O}(\epsilon^p), \end{aligned} \tag{288}$$

where $D_s = \sqrt{q^2\bar{R}^2 + 8\lambda\bar{R} + 4\lambda^2}$.

In the far region, we expand the second piece of integral in ϵ at fixed R. Then we have

$$\begin{aligned} M^2 \int_{\epsilon^p C}^{R_o} \frac{dR}{\sqrt{\mathcal{R}}} &= \int_{\epsilon^p C}^{R_o} \left(\frac{dR}{R\sqrt{q^2 + 4R + R^2}} + \mathcal{O}(\epsilon)\right) \\ &= M^2 \frac{1}{q}\log\left[\frac{2q^2 R_o}{qD_o + q^2 + 2R_o} - p\log\epsilon - \log C\right] + \mathcal{O}(\epsilon^p), \end{aligned} \tag{289}$$

where $D_o = \sqrt{q^2 + 4R_o + R_o^2}$.

By adding Eqs. (288) and (289), we get result for the complete integral

$$I_r = -\frac{1}{q}\log\epsilon + \frac{1}{q}\log\left[\frac{4q^4 R_o}{(qD_o + q^2 + 2R_o)(qD_s + q^2\bar{R} + 4\lambda)}\right] + \mathcal{O}(\epsilon). \tag{290}$$

Second example.

We then perform second integral of Eq. (284a). The integral is:

$$\tilde{I}_r = 2M\int_{r_{\min}}^{r_s}\frac{dr}{\sqrt{\mathcal{R}(r)}}, \quad \mathcal{R}(r) = \left(r^2 + a^2 - a\hat{\lambda}\right)^2 - \left(r^2 - 2Mr + a^2\right)\left[\hat{q}^2 + \left(a - \hat{\lambda}\right)^2\right]. \tag{291}$$

This integral is in the near horizon region (the NHEK region to be precise) $R \sim \epsilon$. We work with $\tilde{R} = R/\epsilon$ and find the larger root of $\mathcal{R}(r)$,

$$\tilde{R}_{\min} = \frac{1 + a^2}{q^2}\left(-2\lambda + |\lambda|\sqrt{4 - q^2}\right). \tag{292}$$

Since $r_{\min} < r_+$ for $\lambda > 0$, we should then exclude the case of positive λ. However, note that we have the $1/\Delta$ factor in Eq. (303b) (which is meaningless when it goes through the event horizon), the integral of $\tilde{J}_r$ does not exist at all in that case which precludes the existence of a valid light ray. Therefore, we may still perform the integral regardless whether λ is negative or positive. After computing we get the result for the integral

$$\begin{aligned}\tilde{I}_r &= 2M^2\int_{\tilde{R}_{\min}}^{\bar{R}}\left[\frac{d\tilde{R}}{\sqrt{q^2\tilde{R}^2 + 8\lambda\tilde{R} + 4\lambda^2}} + \mathcal{O}(\epsilon)\right] \\ &= \frac{1}{q}\log\left[\frac{(qD_s + q^2\bar{R} + 4\lambda)^2}{4(4 - q^2)\lambda^2}\right] + \mathcal{O}(\epsilon).\end{aligned} \tag{293}$$

A.1 RESULTS FOR KERR IN VACUUM

For the vacuum Kerr case, we have

$$\mathcal{R}(r) = \left(r^2 + a^2 - a\hat{\lambda}\right)^2 - \Delta\left[\hat{q}^2 + \left(a - \hat{\lambda}\right)^2\right], \tag{294a}$$

$$\mathcal{J}_r = \frac{1}{\Delta}\left[a(2Mr - a\hat{\lambda}) - \Omega_s r\left(r^3 + a^2(r + 2M) - 2aM\hat{\lambda}\right)\right], \tag{294b}$$

where $\Delta = r^2 - 2Mr + a^2$ and $\Omega_s = M^{1/2}/(r_s^{3/2} + aM^{1/2})$. In the near-extremal regime, we have the expansions (286). The list of results for the integrals and their variations with respect to λ and q are given in Eqs. (300) and (302) for $a = 1$.

A.2 RESULTS FOR KERR IN A PLASMA

For the case of the Kerr black hole in a plasma, we have

$$\mathcal{R}(r) = \left(r^2 + a^2 - a\hat{\lambda}\right)^2 - \Delta\left[\hat{q}^2 + \left(a - \hat{\lambda}\right)^2 + \hat{f}_r(r)\right], \tag{295a}$$

$$\mathcal{J}_r = \frac{1}{\Delta}\left[a(2Mr - a\hat{\lambda}) - \Omega_s r\left(r^3 + a^2(r + 2M) - 2aM\hat{\lambda}\right)\right], \tag{295b}$$

where $\Delta = r^2 - 2Mr + a^2$, $\Omega_s = M^{1/2}/(r_s^{3/2} + aM^{1/2})$, and $\hat{f}_r(r)$ is a function appearing in the expression of plasma density (see Sec. 3.2.2).

In the near-extremal regime, we have the expansions (154). Next, we list the results of integrals for $\hat{f}_r(r) = \hat{\omega}_c^2 Mr$, as follows,

$$I_r = \frac{1}{\tilde{q}}\log\left[\frac{4\tilde{q}^4 R_o}{\left(\tilde{q}^2 + (2 - \frac{\hat{\omega}_c^2}{2})R_o + \tilde{q}D_o\right)\left(\tilde{q}D_s + \tilde{q}^2\bar{R} + 4\lambda\right)}\right] - \frac{\log\epsilon}{\tilde{q}} + \mathcal{O}(\epsilon), \tag{296a}$$

$$\tilde{I}_r = \frac{1}{\tilde{q}}\log\left[\frac{\left(\tilde{q}D_s + \tilde{q}^2\bar{R} + 4\lambda\right)^2}{4(4 - \tilde{q}^2)\lambda^2}\right] + \mathcal{O}(\epsilon), \tag{296b}$$

$$\begin{aligned} J_r = {} & \log\left[\frac{\bar{R}(2 + \tilde{q})(2 - \frac{\hat{\omega}_c^2}{2} + \tilde{q})^{1 + \frac{1}{4}\hat{\omega}_c^2}}{(D_s + 2\bar{R} + 2\lambda)(2 - \frac{\hat{\omega}_c^2}{2} + D_o + R_o)^{1 + \frac{1}{4}\hat{\omega}_c^2}}\right] - \frac{7}{2}I_r + \frac{3}{8\lambda}(D_s - \tilde{q}\bar{R}) \\ & + \frac{1}{2}(\tilde{q} - D_o) + \mathcal{O}(\epsilon), \end{aligned} \tag{296c}$$

$$\tilde{J}_r = -\frac{7}{2}\tilde{I}_r - \frac{3}{4}\frac{D_s}{\lambda} + \log\left[\frac{(D_s + 2\bar{R} + 2\lambda)^2}{(4 - \tilde{q}^2)\bar{R}^2}\right] + \mathcal{O}(\epsilon), \tag{296d}$$

where $\tilde{q} = \sqrt{q^2 - \hat{\omega}_c^2}$, and

$$D_s = \sqrt{\tilde{q}^2\bar{R}^2 + 8\lambda\bar{R} + 4\lambda^2}, \quad D_o = \sqrt{\tilde{q}^2 + (4 - \hat{\omega}_c^2)R_o + R_o^2}. \tag{297a}$$

Note that for $\hat{\omega}_c = 0$, these give the results for $\hat{f}_r(r) = 0$.

For $\hat{f}_r(r) = M^2\hat{\omega}_c^2$, the expansions (153) are similar as those for $\hat{f}_r(r) = 0$ up to a replacement of $q \to \sqrt{q^2 - \hat{\omega}_c^2}$. Thus, the final results of the integrals are obtained by including this replacement in those for $\hat{f}_r(r) = 0$.

A.3 RESULTS FOR KERR-MOG

For the KM case, we have

$$\mathcal{R}(r) = \left(r^2 + a^2 - a\hat{\lambda}\right)^2 - \Delta\left[\hat{q}^2 + \left(a - \hat{\lambda}\right)^2\right], \tag{298a}$$

$$\mathcal{J}_r = \frac{1}{\Delta}\left[a\left(2M_\chi r - Q_\chi^2 - a\hat{\lambda}\right) - \Omega_s[r^4 + a^2(r^2 + 2M_\chi r - Q_\chi^2) - a(2M_\chi r - Q_\chi^2)\hat{\lambda}]\right], \tag{298b}$$

where

$$\Delta = r^2 - 2M_\chi r + a^2 + Q_\chi^2, \quad \Omega_s = \frac{(M_\chi - Q_\chi^2)^{1/2}}{r_s^2 + a(M_\chi - Q_\chi^2)^{1/2}} \tag{299}$$

with $M_\chi = (1+\chi)M$ and $Q_\chi = (\chi M_\chi^2)/(1+\chi)$. Later we set $M_\chi = 1$ for convenience.

For the near-extremal regime of KM, we have the expansions (207). We now list the radial integrals appearing in the KM len equations (245),

$$I_r = -\frac{1}{q}\log\epsilon + \frac{1}{q}\log\left[\frac{4q^4 R_o}{(qD_o + q^2 + 2R_o)(qD_s + q^2\bar{R} + 2(1+a^2)\lambda)}\right] + \mathcal{O}(\epsilon), \tag{300a}$$

$$\tilde{I}_r = \frac{1}{q}\log\left[\frac{(qD_s + q^2\bar{R} + 2(1+a^2)\lambda)^2}{(1+a^2)^2(4-q^2)\lambda^2}\right] + \mathcal{O}(\epsilon), \tag{300b}$$

$$\begin{aligned} J_r = &-\frac{a(6+a^2)}{1+a^2}I_r - \frac{a}{1+a^2}(D_o - q) - \frac{4a^2-1}{2a(1+a^2)^2}\left(\frac{q\bar{R}}{\lambda} - \frac{D_s}{\lambda}\right) \\ &+\frac{2a}{1+a^2}\log\left[\frac{(q+2)^2\bar{R}}{(D_o + R_o + 2)(D_s + 2\bar{R} + (1+a^2)\lambda)}\right] + \mathcal{O}(\epsilon), \end{aligned} \tag{300c}$$

$$\tilde{J}_r = -\frac{a(6+a^2)}{1+a^2}\tilde{I}_r - \frac{4a^2-1}{a(1+a^2)^2}\frac{D_s}{\lambda} + \frac{2a}{1+a^2}\log\left[\frac{(D_s + 2\bar{R} + (1+a^2)\lambda)^2}{(4-q^2)\bar{R}^2}\right] + \mathcal{O}(\epsilon), \tag{300d}$$

where

$$D_s = \sqrt{q^2\bar{R}^2 + 4(1+a^2)\lambda\bar{R} + (1+a^2)^2\lambda^2}, \quad D_o = \sqrt{q^2 + 4R_o + R_o^2}. \tag{301}$$

Next, we list the variations of these integrals with respect to λ and q,

$$\frac{\partial I_r}{\partial \lambda} = \frac{1}{\lambda}\left(\frac{\bar{R}}{D_s} - \frac{1}{q}\right), \tag{302a}$$

$$\frac{\partial \tilde{I}_r}{\partial \lambda} = -\frac{2}{\lambda}\frac{\bar{R}}{D_s}, \tag{302b}$$

$$\frac{\partial I_r}{\partial q} = -\frac{1}{q}I_r - \frac{1}{q(4-q^2)}\left[(8-q^2)\left(\frac{\bar{R}}{D_s} + \frac{1}{D_o} - \frac{2}{q}\right) + \frac{2(1+a^2)\lambda}{D_s} + \frac{2R_o}{D_o}\right], \tag{302c}$$

$$\frac{\partial \tilde{I}_r}{\partial q} = -\frac{1}{q}\tilde{I}_r + \frac{2}{q(4-q^2)}\left[(8-q^2)\frac{\bar{R}}{D_s} + 2(1+a^2)\frac{\lambda}{D_s}\right], \tag{302d}$$

$$\frac{\partial J_r}{\partial \lambda} = -\frac{1}{2aD_s} - \frac{1}{\lambda}\left(\frac{1+a^2}{a}\frac{\bar{R}}{D_s} - \frac{a(6+a^2)}{1+a^2}\frac{1}{q}\right) - \frac{4a^2-1}{2a(1+a^2)^2}\frac{D_s - q\bar{R}}{\lambda^2}, \tag{302e}$$

$$\frac{\partial \tilde{J}_r}{\partial \lambda} = \frac{1}{aD_s} + \frac{2(1+a^2)\bar{R}}{aD_s\lambda} + \frac{(4a^2-1)D_s}{a(1+a^2)^2\lambda^2}, \tag{302f}$$

$$\begin{aligned}\frac{\partial J_r}{\partial q} = {} & \frac{a(6+a^2)I_r}{(1+a^2)q} + \frac{4a^2-1}{2a(1+a^2)^2}\left(\frac{D_s}{q\lambda} - \frac{\bar{R}}{\lambda}\right) + \frac{a}{1+a^2} - \frac{2a(10+a^2)}{(1+a^2)q^2} - \frac{8a(2+a^2)}{(1+a^2)(4-q^2)q^2} \\ & + \frac{\left[2a^2(2+a^2)(8-q^2) + 4(4-q^2)\right]\bar{R} + (1+a^2)\left[4a^2(2+a^2) + (4-q^2)\right]\lambda}{2a(1+a^2)(4-q^2)qD_s} \\ & + \frac{a\left[(8-q^2+2R_o)(6+a^2-q^2)\right]}{(1+a^2)(4-q^2)qD_o},\end{aligned} \tag{302g}$$

$$\begin{aligned}\frac{\partial \tilde{J}_r}{\partial q} = {} & \frac{a(6+a^2)\tilde{I}_r}{(1+a^2)q} - \frac{\left[2a^2(2+a^2)(8-q^2) + 4(4-q^2)\right]\bar{R} + (1+a^2)\left[4a^2(2+a^2) + (4-q^2)\right]\lambda}{a(1+a^2)(4-q^2)qD_s} \\ & - \frac{(4a^2-1)D_s}{a(1+a^2)^2 q\lambda}.\end{aligned} \tag{302h}$$

A.4 RESULTS FOR KERR-SEN

For the KS case, we have

$$\mathcal{R}(r) = (a\hat{\lambda} - \delta)^2 - \Delta\left[\hat{q}^2 + (\hat{\lambda} - a)^2\right], \tag{303a}$$

$$\mathcal{J}_r = \frac{1}{\Delta}\left[a(2Mr - a\hat{\lambda}) - \Omega_s\left(\delta^2 - a^2\Delta - 2aMr\hat{\lambda}\right)\right], \tag{303b}$$

where

$$\delta = r^2 + a^2 + 2r_\alpha r, \quad \Delta = \delta - 2Mr, \quad \Omega_s = \frac{M^{1/2}}{(r+2r_\alpha)(r+r_\alpha)^{1/2} + aM^{1/2}}. \tag{304}$$

In the near-extremal regime, we have the expansions (268). We now list the results for these integrals which appear in the KS lens equations (245),

$$I_r = \frac{1}{q}\log\Big[\frac{4q^4R_o}{(qD_o+q^2+2R_o)(qD_s+q^2\bar{R}+4(1-\tilde{r}_\alpha)\lambda)}\Big] - \frac{1}{q}\log\epsilon + \mathcal{O}(\epsilon), \tag{305a}$$

$$\tilde{I}_r = \frac{1}{q}\log\Big[\frac{(qD_s+q^2\bar{R}+4(1-\tilde{r}_\alpha)\lambda)^2}{4(1-\tilde{r}_\alpha)^2(4-q^2)\lambda^2}\Big] + \mathcal{O}(\epsilon), \tag{305b}$$

$$\begin{aligned} J_r = &-\frac{7-2\tilde{r}_\alpha-\tilde{r}_\alpha^2}{2}I_r - \frac{1}{2}(D_o-q) - \frac{3+\tilde{r}_\alpha}{8}\Big(\frac{q\bar{R}}{\lambda}-\frac{D_s}{\lambda}\Big) \\ &+\log\Big[\frac{(q+2)^2\bar{R}}{(D_o+R_o+2)(D_s+2\bar{R}+2(1-\tilde{r}_\alpha)\lambda)}\Big] + \mathcal{O}(\epsilon), \end{aligned} \tag{305c}$$

$$\tilde{J}_r = -\frac{7-2\tilde{r}_\alpha-\tilde{r}_\alpha^2}{2}\tilde{I}_r - \frac{3+\tilde{r}_\alpha}{4}\frac{D_s}{\lambda} + \log\Big[\frac{(D_s+2\bar{R}+2(1-\tilde{r}_\alpha)\lambda)^2}{(4-q^2)\bar{R}^2}\Big] + \mathcal{O}(\epsilon), \tag{305d}$$

where $\tilde{r}_\alpha = r_\alpha/M$ and

$$D_s = \sqrt{q^2\bar{R}^2 + 8(1-\tilde{r}_\alpha)\lambda\bar{R} + 4(1-\tilde{r}_\alpha)^2\lambda^2}, \quad D_o = \sqrt{q^2+4R_o+R_o^2}. \tag{306}$$

B

ANGULAR INTEGRALS

In this appendix, we deal with the angular integrals appearing in the lens equations in the main body of the text [Eq. (66) for Kerr in vacuum, Eq. (134) for Kerr in a plasma, Eq. (184) for KM and Eq. (245) for KS]. These integrals in the different cases are defined in a similar way as [5]

$$G_i^{m,s} = \begin{cases} \hat{G}_i & m = 0, \\ mG_i - s\hat{G}_i & m \geq 1, \end{cases} \quad i \in \{t, \theta, \phi\}\,. \tag{307}$$

with

$$G_i = M \int_{\theta_-}^{\theta_+} g_i(\theta) d\theta, \quad \hat{G}_i = M \int_{\theta_o}^{\pi/2} g_i(\theta) d\theta, \tag{308}$$

and

$$g_\theta = \frac{1}{\sqrt{\Theta(\theta)}}, \quad g_\phi = \frac{\csc^2\theta}{\sqrt{\Theta(\theta)}}, \quad g_t = \frac{\cos^2\theta}{\sqrt{\Theta(\theta)}}, \tag{309}$$

where $\Theta(\theta)$ is the angular potential for each case and $\theta_\pm$ are roots of it. Note that M in Eq. (308) is replaced by M_χ for the KM case.

These integrals can be expressed in terms of elliptic functions [84]. Taking the vacuum Kerr case [5] for example, we have

$$\Theta(\theta) = \hat{q}^2 + a^2 \cos^2\theta - \hat{\lambda}^2 \cot^2\theta. \tag{310}$$

We make the change of variables by $u = \cos^2\theta$, then by solving angular potential $\Theta(u) = \hat{q} + u[a^2 - \hat{\lambda}^2(1-u)^{-1}] = 0$ we find the roots [5]

$$u_\pm = \Delta_\theta \pm \sqrt{\Delta_\theta^2 + \frac{\hat{q}^2}{a^2}}, \qquad \Delta_\theta = \frac{1}{2}\left(1 - \frac{\hat{q}^2 + \hat{\lambda}^2}{a^2}\right). \tag{311}$$

Therefore $\Theta(\theta)$ has roots at $\theta_\pm = \arccos \mp\sqrt{u_+}$, with the relation $0 < \theta_- < \theta_+ < \pi$. Note that we also have $u_- < 0 < u_+$. Then, the expressions for the angular integrals are given by [5]:

$$G_\theta = M\int_{\theta_-}^{\theta_+} \frac{d\theta}{\sqrt{\Theta(\theta)}} = \frac{2M}{|a|\sqrt{-u_-}} K\left(\frac{u_+}{u_-}\right), \tag{312a}$$

$$\hat{G}_\theta = M\int_{\theta_o}^{\pi/2} \frac{d\theta}{\sqrt{\Theta(\theta)}} = \frac{M}{|a|\sqrt{-u_-}} F\left(\Psi_o \middle| \frac{u_+}{u_-}\right), \tag{312b}$$

$$G_\phi = M\int_{\theta_-}^{\theta_+} \frac{\csc^2\theta}{\sqrt{\Theta(\theta)}} d\theta = \frac{2M}{|a|\sqrt{-u_-}} \Pi\left(u_+ \middle| \frac{u_+}{u_-}\right), \tag{312c}$$

$$\hat{G}_\phi = M\int_{\theta_o}^{\pi/2} \frac{\csc^2\theta}{\sqrt{\Theta(\theta)}} d\theta = \frac{M}{|a|\sqrt{-u_-}} \Pi\left(u_+; \Psi_o \middle| \frac{u_+}{u_-}\right), \tag{312d}$$

$$G_t = M\int_{\theta_-}^{\theta_+} \frac{\cos^2\theta}{\sqrt{\Theta(\theta)}} d\theta = -\frac{4Mu_+}{|a|\sqrt{-u_-}} E'\left(\frac{u_+}{u_-}\right), \tag{312e}$$

$$\hat{G}_t = M_\alpha\int_{\theta_o}^{\pi/2} \frac{\cos^2\theta}{\sqrt{\Theta(\theta)}} d\theta = -\frac{2M_\alpha u_+}{|a|\sqrt{-u_-}} E'\left(\Psi_o \middle| \frac{u_+}{u_-}\right), \tag{312f}$$

where $E'(\phi|m) = \partial_m E(\phi|m)$, and $F(\phi|m)$, $E(\phi|m)$, $\Pi(n;\phi|m)$ are the incomplete elliptic integrals of the first, second and third kind, and $K(m)$, $E(m)$, $\Pi(n|m)$ are the complete elliptic integrals of the first, second and third kind, and $\Psi_o = \arcsin\sqrt{\cos^2\theta_o/u_+}$.

B.1 RESULTS FOR KERR IN VACUUM

In the near-extremal limit for the vacuum Kerr case, we have the expansions (286). Then [5]

$$u_\pm = \mathcal{I}_\pm + \mathcal{O}(\epsilon), \quad \mathcal{I}_\pm = \frac{q^2}{2} - 3 \pm \sqrt{12 - (2q)^2 + \left(\frac{q^2}{2}\right)^2}, \tag{313}$$

$$\Psi_o = \arcsin\sqrt{\frac{\cos^2\theta_o}{\mathcal{I}_+}} + \mathcal{O}(\epsilon), \tag{314}$$

and the results for angular integrals are

$$G_\theta = \frac{2}{\sqrt{-\mathcal{I}_-}} K\left(\frac{\mathcal{I}_+}{\mathcal{I}_-}\right) + \mathcal{O}(\epsilon), \quad \hat{G}_\theta = \frac{1}{\sqrt{-\mathcal{I}_-}} F\left(\Psi_o \middle| \frac{\mathcal{I}_+}{\mathcal{I}_-}\right) + \mathcal{O}(\epsilon), \tag{315a}$$

$$G_\phi = \frac{2}{\sqrt{-\mathcal{I}_-}} \Pi\left(\mathcal{I}_+ \middle| \frac{\mathcal{I}_+}{\mathcal{I}_-}\right) + \mathcal{O}(\epsilon), \quad \hat{G}_\phi = \frac{1}{\sqrt{-\mathcal{I}_-}} \Pi\left(\mathcal{I}_+; \Psi_o \middle| \frac{\mathcal{I}_+}{\mathcal{I}_-}\right) + \mathcal{O}(\epsilon), \tag{315b}$$

$$G_t = -\frac{4\mathcal{I}_+}{\sqrt{-\mathcal{I}_-}} E'\left(\frac{\mathcal{I}_+}{\mathcal{I}_-}\right) + \mathcal{O}(\epsilon), \quad \hat{G}_t = -\frac{2\mathcal{I}_+}{\sqrt{-\mathcal{I}_-}} E'\left(\Psi_o \middle| \frac{\mathcal{I}_+}{\mathcal{I}_-}\right) + \mathcal{O}(\epsilon). \tag{315c}$$

B.2 RESULTS FOR KERR IN A PLASMA

For the case of the Kerr black hole in a plasma, we have

$$\Theta(\theta) = \hat{q}^2 + a^2 \cos^2\theta - \hat{\lambda}^2 \cot^2\theta - \hat{f}_\theta(\theta), \tag{316}$$

where $\hat{f}_\theta(\theta)$ is a function appearing in the expression of plasma density (see Sec. 3.2.2). We will perform the integrals for $f_\theta(\theta) = \omega_c^2 M^2$. In this case, the angular potential can be written as

$$\Theta(u) = \hat{q}^2 - \hat{\omega}_c^2 M^2 + u\left[a^2 - \hat{\lambda}^2 (1-u)^{-1}\right], \tag{317}$$

which are similar as those in the vacuum Kerr case up to the replacement: $\hat{q}^2 \to \hat{q}^2 - \hat{\omega}_c^2 M^2$. Therefore, the results for these integrals are obtained by just replace q by $\sqrt{q^2 + \hat{\omega}_c^2}$ in Eq. (315).

B.3 RESULTS FOR KERR-MOG

For the KM case, the angular potential $\Theta(\theta)$ takes the same form as the Kerr case, Eq. (310). Then the expressions for the results take the same form as Eq. (312) except replacing M by M_χ. Later we set $M_\chi = 1$ for convenience.

For the near-extremal regime of KM, we have the expansions (207). Then the final results for the angular integrals are

$$G_\theta = \frac{2}{a\sqrt{-\mathcal{I}_-}}K\left(\frac{\mathcal{I}_+}{\mathcal{I}_-}\right) + \mathcal{O}(\epsilon), \qquad \hat{G}_\theta = \frac{1}{a\sqrt{-\mathcal{I}_-}}F\left(\Psi_o\middle|\frac{\mathcal{I}_+}{\mathcal{I}_-}\right) + \mathcal{O}(\epsilon), \tag{318a}$$

$$G_\phi = \frac{2}{a\sqrt{-\mathcal{I}_-}}\Pi\left(\mathcal{I}_+\middle|\frac{\mathcal{I}_+}{\mathcal{I}_-}\right) + \mathcal{O}(\epsilon), \quad \hat{G}_\phi = \frac{1}{a\sqrt{-\mathcal{I}_-}}\Pi\left(\mathcal{I}_+;\Psi_o\middle|\frac{\mathcal{I}_+}{\mathcal{I}_-}\right) + \mathcal{O}(\epsilon), \tag{318b}$$

$$G_t = -\frac{4\mathcal{I}_+}{a\sqrt{-\mathcal{I}_-}}E'\left(\frac{\mathcal{I}_+}{\mathcal{I}_-}\right) + \mathcal{O}(\epsilon), \qquad \hat{G}_t = -\frac{2\mathcal{I}_+}{a\sqrt{-\mathcal{I}_-}}E'\left(\Psi_o\middle|\frac{\mathcal{I}_+}{\mathcal{I}_-}\right) + \mathcal{O}(\epsilon), \tag{318c}$$

where

$$\mathcal{I}_\pm = \frac{q^2-6}{2a^2} \pm \frac{1}{a^2}\sqrt{8-3q^2+(4-q^2)a^2+\left(\frac{q^2}{2}\right)^2}, \quad \Psi_o = \arcsin\sqrt{\frac{\cos^2\theta_o}{\mathcal{I}_+}}. \tag{319}$$

B.4 RESULTS FOR KERR-SEN

For the KS case, the angular potential $\Theta(\theta)$ takes the same form as the Kerr case, Eq. (310). In the near-extremal regime, we have the expansions (268), then the results for the angular integrals are

$$G_\theta = \frac{2}{(1-\tilde{r}_\alpha^2)\sqrt{-\mathcal{I}_-}}K\left(\frac{\mathcal{I}_+}{\mathcal{I}_-}\right) + \mathcal{O}(\epsilon), \tag{320a}$$

$$\hat{G}_\theta = \frac{1}{(1-\tilde{r}_\alpha^2)\sqrt{-\mathcal{I}_-}}F\left(\Psi_o\middle|\frac{\mathcal{I}_+}{\mathcal{I}_-}\right) + \mathcal{O}(\epsilon), \tag{320b}$$

$$G_\phi = \frac{2}{(1-\tilde{r}_\alpha^2)\sqrt{-\mathcal{I}_-}}\Pi\left(\mathcal{I}_+\middle|\frac{\mathcal{I}_+}{\mathcal{I}_-}\right) + \mathcal{O}(\epsilon), \tag{320c}$$

$$\hat{G}_\phi = \frac{1}{(1-\tilde{r}_\alpha^2)\sqrt{-\mathcal{I}_-}}\Pi\left(\mathcal{I}_+;\Psi_o\middle|\frac{\mathcal{I}_+}{\mathcal{I}_-}\right) + \mathcal{O}(\epsilon), \tag{320d}$$

$$G_t = -\frac{4\mathcal{I}_+}{(1-\tilde{r}_\alpha^2)\sqrt{-\mathcal{I}_-}}E'\left(\frac{\mathcal{I}_+}{\mathcal{I}_-}\right) + \mathcal{O}(\epsilon), \tag{320e}$$

$$\hat{G}_t = -\frac{2\mathcal{I}_+}{(1-\tilde{r}_\alpha^2)\sqrt{-\mathcal{I}_-}}E'\left(\Psi_o\middle|\frac{\mathcal{I}_+}{\mathcal{I}_-}\right) + \mathcal{O}(\epsilon), \tag{320f}$$

where $\tilde{r}_\alpha = r_\alpha/M$ and

$$\mathcal{I}_\pm = \frac{q^2-6+2\tilde{r}_\alpha^2 \pm \sqrt{(4-q^2)(12-q^2-8\tilde{r}_\alpha)}}{2(1-\tilde{r}_\alpha^2)}, \quad \Psi_o = \arcsin\sqrt{\frac{\cos^2\theta_o}{\mathcal{I}_+}}. \tag{321}$$

C

IMAGE FLUX

The energy flux of an image on the observer's screen is determined by the product of observed intensity and the apparent size of solid angle [46]. In order to study the effects of gravity, it is instructive to compare the observed image flux with the corresponding "Newtonian flux". In the Newtonian case, the energy flux for a particular image of a spherical emitter with a proper radius $\rho \ll M$ is given by

$$F_{\rm N} = \frac{\pi\rho^2}{r_o^2} I_s. \tag{322}$$

In the black hole case, the observed intensity and the angular size of the image are varied, then the image flux becomes

$$F_o = \iint \frac{d\alpha d\beta}{r_o^2} I_o, \quad I_o = g^4 I_s. \tag{323}$$

Next, we introduce the procedure for computing the flux in the vacuum Kerr case [5]. In the main body, this procedure has also been applied to compute the flux for the other cases.

The flux (323) corresponds to a narrow bundle of rays that approximately have a uniform redshift g. Therefore, we can write

$$F_o = g^4 I_s \frac{\mathcal{A}}{r_o^2}, \quad \mathcal{A} = \iint d\alpha d\beta, \tag{324}$$

where $\mathcal{A}$ is the apparent area of the image on the observer's sky. This area is described by screen coordinates (α, β) [Eq. (53)], which corresponds to light rays intersecting with the observer's screen.

In order to compute the area $\mathcal{A}$, we instead consider the intersection of these rays with the "source plane"—a plane through the center of the emitter perpendicular to proper radial direction. It is convenient to define a proper coordinate system (T, X, Y, Z) of the emitter by [see Eq. (59)]

$$\frac{\partial}{\partial T} = e_{(t_s)}, \qquad \frac{\partial}{\partial X} = e_{(r_s)}, \qquad \frac{\partial}{\partial Y} = e_{(\phi_s)}, \qquad \frac{\partial}{\partial Z} = -e_{(\theta_s)}. \tag{325}$$

Then we have

$$t - t_\star = \gamma\sqrt{\frac{\Xi}{\Delta\Sigma}}(T + \Omega_s Y), \qquad r - r_\star = \sqrt{\frac{\Delta}{\Sigma}}X, \qquad \theta - \theta_\star = -\frac{1}{\sqrt{\Sigma}}Z, \tag{326a}$$

$$\phi - \phi_\star = \gamma\sqrt{\frac{\Xi}{\Delta\Sigma}}(\Omega_s T + \omega v_s Y) + \gamma\sqrt{\frac{\Sigma}{\Xi}}Y, \tag{326b}$$

where Ξ, Δ, Σ and $\Omega_{\rm bh}$ are given in Eqs. (9) and (8) and evaluated at (r_s, θ_s), and Ω_s is given in Eq. (30), γ and v_s are given in Eq. (60), and x^μ_* are the coordinates of the central position of the emitter. Then the plane with $T = X = 0$ is the source plane and the area of intersection of the bundle of rays with this plane can be described with the source plane coordinates (Y_s, Z_s).

Now we may compute the area $\mathcal{A}$ through

$$\mathcal{A} = \iint \left|\frac{\partial(\alpha,\beta)}{\partial(Y_s, Z_s)}\right| dY_s dZ_s = \left|\frac{\partial(\alpha,\beta)}{\partial(Y_s, Z_s)}\right| \mathcal{A}_s, \quad \mathcal{A}_s = \iint dY_s dZ_s. \tag{327}$$

where the Jacobian has been treated as constant under the approximation $\rho \ll M$, and $\mathcal{A}_s$ is the projected area of the emitter's surface on the source screen.

First, we compute the area $\mathcal{A}_s$. For small ρ, the narrow bundle light rays are considered to be emitted in the same direction with a unit tangent vector

$$\hat{k} = \frac{1}{p^{(t_s)}}(p^{(r_s)}\hat{X} + p^{(\phi_s)}\hat{Y} - p^{(\theta_s)}\hat{Z}). \tag{328}$$

Then the projected area $\mathcal{A}_s$ can be computed by

$$\mathcal{A}_s = \frac{\pi\rho^2}{\left|\hat{k}\cdot\hat{X}\right|} = \pi\rho^2\left|\frac{p^{(t_s)}}{p^{(r_s)}}\right| = \frac{\pi\rho^2}{g}\sqrt{\frac{\Sigma(r_s,\theta_s)\Delta(r_s)}{\mathcal{R}(r_s)}}. \tag{329}$$

Next, we compute the Jabobian in Eq. (327). We will compute it in stages

$$\left|\frac{\partial(\alpha,\beta)}{\partial(Y_s, Z_s)}\right| = \left|\frac{\partial(\phi^*_s,\theta_s)}{\partial(Y_s, Z_s)}\right| \left|\frac{\partial(\phi^*_s,\theta_s)}{\partial(\hat{\lambda},\hat{q})}\right|^{-1} \left|\frac{\partial(\alpha,\beta)}{\partial(\hat{\lambda},\hat{q})}\right|, \tag{330}$$

where we have defined $\phi_s^* = \phi_s - \Omega_s t_s$ for convenience. From Eqs. (326) we have

$$\left|\frac{\partial(\phi_s^*, \theta_s)}{\partial(Y_s, Z_s)}\right| = \frac{1}{\gamma\sqrt{\Xi(r_s, \theta_s)}} \tag{331}$$

From Eqs. (53) we have

$$\left|\frac{\partial(\alpha, \beta)}{\partial(\hat{\lambda}, \hat{q})}\right| = \frac{\hat{q}}{\sin\theta_o\sqrt{\hat{q}^2 + a^2\cos^2\theta_o - \hat{\lambda}^2\cot^2\theta_o}} = \frac{\hat{q}}{\sin\theta_o\sqrt{\Theta(\theta_o)}}. \tag{332}$$

It remains to compute the middle Jacobian, this involves to consider perturbation to the lens equations governing the rays $(\hat{\lambda}, \hat{q})$. We consider the variation of θ_s and ϕ_s^* with the rays at fixed r_s and at fixed $t_o, r_o, \theta_o, \phi_o$. In order to allow θ_s to be varied, one need to generalize the lens equations (66) to allow $\theta_s \neq \pi/2$. It is convenient to rewrite the lens equations as

$$A = 0, \qquad A \equiv I_r + b\tilde{I}_r - G_\theta^{m,s} \pm M\int_{\pi/2}^{\theta_s}\frac{\theta}{\sqrt{\Theta(\theta)}}, \tag{333a}$$

$$B = \Delta\phi^* = -\Omega_s t_o + 2\pi N, \quad B \equiv J_r + b\tilde{J}_r + \frac{1}{M}\left[\hat{\lambda}G_\phi^{m,s} - \Omega_s a^2 G_t^{m,s}\right]. \tag{333b}$$

Taking total derivatives of A and B with respect to $\hat{\lambda}$ and $\hat{q}$, we then obtain

$$\frac{\partial\theta_s}{\partial\hat{\lambda}} = \mp\frac{M}{\sqrt{\Theta(\theta_s)}}\frac{\partial A}{\partial\hat{\lambda}}, \quad \frac{\partial\theta_s}{\partial\hat{q}} = \mp\frac{M}{\sqrt{\Theta(\theta_s)}}\frac{\partial A}{\partial\hat{q}}, \quad \frac{\partial\phi_s^*}{\partial\hat{\lambda}} = -\frac{\partial B}{\partial\hat{\lambda}}, \quad \frac{\partial\phi_s^*}{\partial\hat{q}} = -\frac{\partial B}{\partial\hat{q}}. \tag{334}$$

Thus, the middle determinant in Eq. (330) is obtained as

$$\left|\frac{\partial(\phi_s^*, \theta_s)}{\partial(\hat{\lambda}, \hat{q})}\right| = \frac{\sqrt{\Theta(\theta_s)}}{M}\left|\det\begin{pmatrix}\frac{\partial B}{\partial\hat{\lambda}} & \frac{\partial B}{\partial\hat{q}} \\ \frac{\partial A}{\partial\hat{\lambda}} & \frac{\partial A}{\partial\hat{q}}\end{pmatrix}\right|. \tag{335}$$

Putting everything together, we finally obtain the normalized flux

$$\frac{F_o}{F_N} = g^3\frac{\hat{q}M}{\gamma\sin\theta_o}\sqrt{\frac{\Sigma(r_s, \theta_s)\Delta(r_s)}{\Xi(r_s, \theta_s)\Theta(\theta_o)\Theta(\theta_s)\mathcal{R}(r_s)}}\left|\det\frac{\partial(B, A)}{\partial(\hat{\lambda}, \hat{q})}\right|^{-1}. \tag{336}$$

BIBLIOGRAPHY

[1] M. Guo, N. A. Obers, and H. Yan, "Observational signatures of near-extremal Kerr-like black holes in a modified gravity theory at the Event Horizon Telescope," *Phys. Rev.* **D98** no. 8, (2018) 084063, `arXiv:1806.05249 [gr-qc]`.

[2] H. Yan, "Influence of a plasma on the observational signature of a high-spin Kerr black hole," *Phys. Rev.* **D99** no. 8, (2019) 084050, `arXiv:1903.04382 [gr-qc]`.

[3] M. Guo, S. Song, and H. Yan, "Observational signature of a near-extremal Kerr-Sen black hole in the heterotic string theory," *Phys. Rev. D* **101** no. 2, (2020) 024055, `arXiv:1911.04796 [gr-qc]`.

[4] A. P. Porfyriadis, Y. Shi, and A. Strominger, "Photon Emission Near Extreme Kerr Black Holes," *Phys. Rev.* **D95** no. 6, (2017) 064009, `arXiv:1607.06028 [gr-qc]`.

[5] S. E. Gralla, A. Lupsasca, and A. Strominger, "Observational Signature of High Spin at the Event Horizon Telescope," *Mon. Not. Roy. Astron. Soc.* **475** no. 3, (2018) 3829–3853, `arXiv:1710.11112 [astro-ph.HE]`.

[6] E. Curiel, "The many definitions of a black hole," *Nature Astron.* **3** no. 1, (2019) 27–34, `arXiv:1808.01507 [physics.hist-ph]`.

[7] J. Michell, "On the Means of Discovering the Distance, Magnitude, &c. of the Fixed Stars, in Consequence of the Diminution of the Velocity of Their Light, in Case Such a Diminution Should be Found to Take Place in any of Them, and Such Other Data Should be

Procured from Observations, as Would be Farther Necessary for That Purpose. By the Rev. John Michell, B. D. F. R. S. In a Letter to Henry Cavendish, Esq. F. R. S. and A. S.," *Philosophical Transactions of the Royal Society of London Series I* **74** (Jan., 1784) 35–57.

[8] R. M. Wald, *General Relativity*. Chicago Univ. Pr., Chicago, USA, 1984.

[9] Y. B. Zel'Dovich, "The fate of a star and the evolution of gravitational energy upon accretion," *Accretion: A Collection of Influential Papers* **5** no. 3, (1989) 57.

[10] E. Salpeter, "Accretion of Interstellar Matter by Massive Objects," *Astrophys. J.* **140** (1964) 796–800.

[11] B. L. Webster and P. Murdin, "Cygnus x-1-a spectroscopic binary with a heavy companion?," *Nature* **235** no. 5332, (1972) 37–38.

[12] C. T. Bolton, "Identification of cygnus x-1 with hde 226868," *Nature* **235** no. 5336, (1972) 271–273.

[13] F. Eisenhauer *et al.*, "SINFONI in the Galactic Center: Young stars and IR flares in the central light month," *Astrophys. J.* **628** (2005) 246–259, `arXiv:astro-ph/0502129`.

[14] C. Bambi, "Astrophysical Black Holes: A Compact Pedagogical Review," *Annalen Phys.* **530** (2018) 1700430, `arXiv:1711.10256 [gr-qc]`.

[15] A. C. Fabian and A. N. Lasenby, "Astrophysical Black Holes," `arXiv:1911.04305 [astro-ph.HE]`.

[16] **LIGO Scientific, Virgo** Collaboration, B. P. Abbott *et al.*, "Observation of Gravitational Waves from a Binary Black Hole Merger," *Phys. Rev. Lett.* **116** no. 6, (2016) 061102, `arXiv:1602.03837 [gr-qc]`.

[17] **LIGO Scientific, Virgo** Collaboration, B. P. Abbott *et al.*, "GW151226: Observation of Gravitational Waves from a 22-Solar-Mass Binary Black Hole Coalescence," *Phys. Rev. Lett.* **116** no. 24, (2016) 241103, `arXiv:1606.04855 [gr-qc]`.

[18] **LIGO Scientific, Virgo** Collaboration, B. P. Abbott *et al.*, "GW170608: Observation of a 19-solar-mass Binary Black Hole Coalescence," *Astrophys. J.* **851** no. 2, (2017) L35, `arXiv:1711.05578 [astro-ph.HE]`.

[19] **LIGO Scientific, Virgo** Collaboration, B. P. Abbott *et al.*, "GW170817: Implications for the Stochastic Gravitational-Wave Background from Compact Binary Coalescences," *Phys. Rev. Lett.* **120** no. 9, (2018) 091101, `arXiv:1710.05837 [gr-qc]`.

[20] **LIGO Scientific, Virgo** Collaboration, B. P. Abbott *et al.*, "Search for Subsolar-Mass Ultracompact Binaries in Advanced LIGO's First Observing Run," *Phys. Rev. Lett.* **121** no. 23, (2018) 231103, `arXiv:1808.04771 [astro-ph.CO]`.

[21] **Event Horizon Telescope** Collaboration, K. Akiyama *et al.*, "First M87 Event Horizon Telescope Results. I. The Shadow of the Supermassive Black Hole," *Astrophys. J.* **875** no. 1, (2019) L1, `arXiv:1906.11238 [astro-ph.GA]`.

[22] **Event Horizon Telescope** Collaboration, K. Akiyama *et al.*, "First M87 Event Horizon Telescope Results. II. Array and Instrumentation," *Astrophys. J.* **875** no. 1, (2019) L2, `arXiv:1906.11239 [astro-ph.IM]`.

[23] **Event Horizon Telescope** Collaboration, K. Akiyama *et al.*, "First M87 Event Horizon Telescope Results. III. Data Processing and Calibration," *Astrophys. J.* **875** no. 1, (2019) L3, `arXiv:1906.11240 [astro-ph.GA]`.

[24] **Event Horizon Telescope** Collaboration, K. Akiyama *et al.*, "First M87 Event Horizon Telescope Results. IV. Imaging the Central Supermassive Black Hole," *Astrophys. J.* **875** no. 1, (2019) L4, `arXiv:1906.11241 [astro-ph.GA]`.

[25] **Event Horizon Telescope** Collaboration, K. Akiyama *et al.*, "First M87 Event Horizon Telescope Results. V. Physical Origin of the Asymmetric Ring," *Astrophys. J.* **875** no. 1, (2019) L5, `arXiv:1906.11242 [astro-ph.GA]`.

[26] **Event Horizon Telescope** Collaboration, K. Akiyama *et al.*, "First M87 Event Horizon Telescope Results. VI. The Shadow and Mass of the Central Black Hole," *Astrophys. J.* **875** no. 1, (2019) L6, `arXiv:1906.11243 [astro-ph.GA]`.

[27] V. Cardoso and P. Pani, "Tests for the existence of black holes through gravitational wave echoes," *Nature Astron.* **1** no. 9, (2017) 586–591, `arXiv:1709.01525 [gr-qc]`.

[28] P. V. P. Cunha, C. A. R. Herdeiro, E. Radu, and H. F. Runarsson, "Shadows of Kerr black holes with scalar hair," *Phys. Rev. Lett.* **115** no. 21, (2015) 211102, `arXiv:1509.00021 [gr-qc]`.

[29] C. Goddi *et al.*, "BlackHoleCam: Fundamental physics of the galactic center," `arXiv:1606.08879 [astro-ph.HE]`.

[30] S. L. Liebling and C. Palenzuela, "Dynamical Boson Stars," *Living Rev. Rel.* **20** no. 1, (2017) 5, `arXiv:1202.5809 [gr-qc]`.

[31] P. O. Mazur and E. Mottola, "Gravitational vacuum condensate stars," *Proc. Nat. Acad. Sci.* **101** (2004) 9545–9550, `arXiv:gr-qc/0407075`.

[32] M. D. Johnson *et al.*, "Universal Interferometric Signatures of a Black Hole's Photon Ring," *Science advances* **6** no. 12, (2020) eaaz1310, `arXiv:1907.04329 [astro-ph.IM]`.

[33] H. Falcke, "Imaging black holes: past, present and future," *J. Phys. Conf. Ser.* **942** no. 1, (2017) 012001, `arXiv:1801.03298 [astro-ph.HE]`.

[34] J.-P. Luminet, "An Illustrated History of Black Hole Imaging : Personal Recollections (1972-2002)," `arXiv:1902.11196 [astro-ph.HE]`.

[35] P. V. P. Cunha and C. A. R. Herdeiro, "Shadows and strong gravitational lensing: a brief review," *Gen. Rel. Grav.* **50** no. 4, (2018) 42, `arXiv:1801.00860 [gr-qc]`.

[36] G. Bisnovatyi-Kogan, O. Tsupko, and V. Perlick, "Shadow of black holes at local and cosmological distances," in *13th Frascati Workshop on Multifrequency Behaviour of High Energy Cosmic Sources*. 10, 2019. `arXiv:1910.10514 [gr-qc]`.

[37] J. M. Bardeen, "Timelike and null geodesics in the Kerr metric," in *Proceedings, Ecole d'Eté de Physique Théorique: Les Astres Occlus: Les Houches, France, August, 1972*, pp. 215–240. 1973.

[38] J. Synge, "The Escape of Photons from Gravitationally Intense Stars," *Mon. Not. Roy. Astron. Soc.* **131** no. 3, (1966) 463–466.

[39] S. E. Gralla, D. E. Holz, and R. M. Wald, "Black Hole Shadows, Photon Rings, and Lensing Rings," *Phys. Rev.* **D100** no. 2, (2019) 024018, `arXiv:1906.00873 [astro-ph.HE]`.

[40] A. De Vries, "The apparent shape of a rotating charged black hole, closed photon orbits and the bifurcation set a4," *Classical and Quantum Gravity* **17** no. 1, (2000) 123.

[41] A. Abdujabbarov, F. Atamurotov, Y. Kucukakca, B. Ahmedov, and U. Camci, "Shadow of Kerr-Taub-NUT black hole," *Astrophys. Space Sci.* **344** (2013) 429–435, `arXiv:1212.4949 [physics.gen-ph]`.

[42] A. Grenzebach, V. Perlick, and C. Lammerzahl, "Photon Regions and Shadows of Kerr-Newman-NUT Black Holes with a Cosmological Constant," *Phys. Rev.* **D89** no. 12, (2014) 124004, `arXiv:1403.5234 [gr-qc]`.

[43] R. Uniyal, H. Nandan, and K. D. Purohit, "Null geodesics and observables around the Kerr-Sen black hole," *Class. Quant. Grav.* **35** no. 2, (2018) 025003, `arXiv:1703.07510 [gr-qc]`.

[44] J. W. Moffat, "Modified Gravity Black Holes and their Observable Shadows," *Eur. Phys. J.* **C75** no. 3, (2015) 130, `arXiv:1502.01677 [gr-qc]`.

[45] P. V. Cunha, C. A. R. Herdeiro, B. Kleihaus, J. Kunz, and E. Radu, "Shadows of Einstein–dilaton–Gauss–Bonnet black holes," *Phys. Lett. B* **768** (2017) 373–379, `arXiv:1701.00079 [gr-qc]`.

[46] C. Cunningham and J. M. Bardeen, "The optical appearance of a star orbiting an extreme kerr black hole," *The Astrophysical Journal* **183** (1973) 237–264.

[47] V. Dokuchaev and N. Nazarova, "Gravitational Lensing of a star by a rotating black hole," *JETP Lett.* **106** no. 10, (2017) 637–642, `arXiv:1802.00817 [astro-ph.HE]`.

[48] V. I. Dokuchaev and N. O. Nazarova, "Silhouettes of invisible black holes," `arXiv:1911.07695 [gr-qc]`.

[49] V. I. Dokuchaev and N. O. Nazarova, "The brightest point in accretion disk and black hole spin: implication to the image of black hole M87*," *Universe* **5** (2019) 183, `arXiv:1906.07171 [astro-ph.HE]`.

[50] J.-P. Luminet, "Image of a spherical black hole with thin accretion disk," *Astron. Astrophys.* **75** (1979) 228–235.

[51] J. Fukue and T. Yokoyama, "Color photographs of an accretion disk around a black hole," *Publications of the Astronomical Society of Japan* **40** (1988) 15–24.

[52] S. Viergutz, "Image generation in kerr geometry. i. analytical investigations on the stationary emitter-observer problem," *Astronomy and Astrophysics* **272** (1993) 355.

[53] S. Viergutz, "Radiation from arbitrarily shaped objects in the vicinity of kerr black holes," in *The Nearest Active Galaxies*, pp. 155–161. Springer, 1993.

[54] H. Falcke, F. Melia, and E. Agol, "Viewing the shadow of the black hole at the galactic center," *Astrophys. J. Lett.* **528** (2000) L13, `arXiv:astro-ph/9912263`.

[55] A. Lupsasca, A. P. Porfyriadis, and Y. Shi, "Critical Emission from a High-Spin Black Hole," *Phys. Rev.* **D97** no. 6, (2018) 064017, `arXiv:1712.10182 [gr-qc]`.

[56] J. M. Bardeen and G. T. Horowitz, "The Extreme Kerr throat geometry: A Vacuum analog of AdS(2) x S**2," *Phys. Rev. D* **60** (1999) 104030, `arXiv:hep-th/9905099`.

[57] P. Christe, M. Henkel, and J. Cardy, "Introduction to conformal invariance and its applications to critical phenomena," *Physics Today* **47** no. 9, (1994) 94–95, `arXiv:cond-mat/9304035 [cond-mat]`.

[58] J. M. Maldacena, "Non-Gaussian features of primordial fluctuations in single field inflationary models," *JHEP* **05** (2003) 013, `arXiv:astro-ph/0210603`.

[59] J. M. Maldacena and G. L. Pimentel, "On graviton non-Gaussianities during inflation," *JHEP* **09** (2011) 045, `arXiv:1104.2846 [hep-th]`.

[60] A. Strominger, "Inflation and the dS / CFT correspondence," *JHEP* **11** (2001) 049, `arXiv:hep-th/0110087`.

[61] A. Kehagias and A. Riotto, "High Energy Physics Signatures from Inflation and Conformal Symmetry of de Sitter," *Fortsch. Phys.* **63** (2015) 531–542, `arXiv:1501.03515 [hep-th]`.

[62] C. S. Reynolds, "Measuring Black Hole Spin using X-ray Reflection Spectroscopy," *Space Sci. Rev.* **183** no. 1-4, (2014) 277–294, `arXiv:1302.3260 [astro-ph.HE]`.

[63] L. Gou, J. E. McClintock, R. A. Remillard, J. F. Steiner, M. J. Reid, J. A. Orosz, R. Narayan, M. Hanke, and J. García, "Confirmation Via the Continuum-Fitting Method that the Spin of the Black Hole in Cygnus X-1 is Extreme," *Astrophys. J.* **790** no. 1, (2014) 29, `arXiv:1308.4760 [astro-ph.HE]`.

[64] J. E. McClintock, R. Shafee, R. Narayan, R. A. Remillard, S. W. Davis, and L.-X. Li, "The Spin of the Near-Extreme Kerr Black Hole GRS 1915+105," *Astrophys. J.* **652** (2006) 518–539, `arXiv:astro-ph/0606076`.

[65] L. W. Brenneman and C. S. Reynolds, "Constraining Black Hole Spin Via X-ray Spectroscopy," *Astrophys. J.* **652** (2006) 1028–1043, `arXiv:astro-ph/0608502`.

[66] S. E. Gralla, A. P. Porfyriadis, and N. Warburton, "Particle on the Innermost Stable Circular Orbit of a Rapidly Spinning Black Hole," *Phys. Rev. D* **92** no. 6, (2015) 064029, `arXiv:1506.08496 [gr-qc]`.

[67] S. E. Gralla, S. A. Hughes, and N. Warburton, "Inspiral into Gargantua," *Class. Quant. Grav.* **33** no. 15, (2016) 155002, `arXiv:1603.01221 [gr-qc]`. [Erratum: Class.Quant.Grav. 37, 109501 (2020)].

[68] S. Hadar, A. P. Porfyriadis, and A. Strominger, "Gravity Waves from Extreme-Mass-Ratio Plunges into Kerr Black Holes," *Phys. Rev. D* **90** no. 6, (2014) 064045, `arXiv:1403.2797 [hep-th]`.

[69] S. Hadar and A. P. Porfyriadis, "Whirling orbits around twirling black holes from conformal symmetry," *JHEP* **03** (2017) 014, `arXiv:1611.09834 [hep-th]`.

[70] S. Hadar, A. P. Porfyriadis, and A. Strominger, "Fast plunges into Kerr black holes," *JHEP* **07** (2015) 078, `arXiv:1504.07650 [hep-th]`.

[71] G. Compére, K. Fransen, T. Hertog, and J. Long, "Gravitational waves from plunges into Gargantua," *Class. Quant. Grav.* **35** no. 10, (2018) 104002, `arXiv:1712.07130 [gr-qc]`.

[72] A. Lupsasca and M. J. Rodriguez, "Exact Solutions for Extreme Black Hole Magnetospheres," *JHEP* **07** (2015) 090, `arXiv:1412.4124 [hep-th]`.

[73] A. Lupsasca, M. J. Rodriguez, and A. Strominger, "Force-Free Electrodynamics around Extreme Kerr Black Holes," *JHEP* **12** (2014) 185, `arXiv:1406.4133 [hep-th]`.

[74] G. Compére, S. E. Gralla, and A. Lupsasca, "Force-Free Foliations," *Phys. Rev. D* **94** no. 12, (2016) 124012, `arXiv:1606.06727 [math-ph]`.

[75] S. E. Gralla, A. Lupsasca, and A. Strominger, "Near-horizon Kerr Magnetosphere," *Phys. Rev. D* **93** no. 10, (2016) 104041, `arXiv:1602.01833 [hep-th]`.

[76] S. Capozziello and M. De Laurentis, "Extended Theories of Gravity," *Phys. Rept.* **509** (2011) 167–321, `arXiv:1108.6266 [gr-qc]`.

[77] J. W. Moffat, "Scalar-tensor-vector gravity theory," *JCAP* **0603** (2006) 004, `arXiv:gr-qc/0506021 [gr-qc]`.

[78] D. J. Gross, J. A. Harvey, E. Martinec, and R. Rohm, "Heterotic string," *Physical Review Letters* **54** no. 6, (1985) 502.

[79] M. Milgrom, "A Modification of the Newtonian dynamics as a possible alternative to the hidden mass hypothesis," *Astrophys. J.* **270** (1983) 365–370.

[80] J. W. Moffat, "Black Holes in Modified Gravity (MOG)," *Eur. Phys. J.* **C75** no. 4, (2015) 175, `arXiv:1412.5424 [gr-qc]`.

[81] A. Sen, "Rotating charged black hole solution in heterotic string theory," *Phys. Rev. Lett.* **69** (1992) 1006–1009, `arXiv:hep-th/9204046 [hep-th]`.

[82] P. V. P. Cunha, C. A. R. Herdeiro, E. Radu, and H. F. Runarsson, "Shadows of Kerr black holes with and without scalar hair," *Int. J. Mod. Phys. D* **25** no. 09, (2016) 1641021, `arXiv:1605.08293 [gr-qc]`.

[83] J. M. Bardeen, W. H. Press, and S. A. Teukolsky, "Rotating black holes: Locally nonrotating frames, energy extraction, and scalar synchrotron radiation," *Astrophys. J.* **178** (1972) 347.

[84] D. Kapec and A. Lupsasca, "Particle motion near high-spin black holes," *Class. Quant. Grav.* **37** no. 1, (2020) 015006, `arXiv:1905.11406 [hep-th]`.

[85] B. Carter, "Global structure of the Kerr family of gravitational fields," *Phys. Rev.* **174** (1968) 1559–1571.

[86] S. Chandrasekhar, *The mathematical theory of black holes*. 1985.

[87] S. E. Gralla and A. Lupsasca, "Null geodesics of the Kerr exterior," *Phys. Rev. D* **101** no. 4, (2020) 044032, `arXiv:1910.12881 [gr-qc]`.

[88] D. C. Wilkins, "Bound geodesics in the kerr metric," *Physical Review D* **5** no. 4, (1972) 814.

[89] S. E. Vazquez and E. P. Esteban, "Strong field gravitational lensing by a Kerr black hole," *Nuovo Cim. B* **119** (2004) 489–519, `arXiv:gr-qc/0308023`.

[90] C. Cunningham and J. Bardeen, "The optical appearance of a star orbiting an extreme kerr black hole," *The Astrophysical Journal* **173** (1972) L137.

[91] M. H. Johnson and E. Teller, "Intensity changes in the doppler effect," *Proceedings of the National Academy of Sciences* **79** no. 4, (1982) 1340–1340.

[92] E. Carlson, T. Jeltema, and S. Profumo, "Where do the 3.5 keV photons come from? A morphological study of the Galactic Center and of Perseus," *JCAP* **1502** no. 02, (2015) 009, `arXiv:1411.1758 [astro-ph.HE]`.

[93] L. Barack *et al.*, "Black holes, gravitational waves and fundamental physics: a roadmap," *Class. Quant. Grav.* **36** no. 14, (2019) 143001, `arXiv:1806.05195 [gr-qc]`.

[94] D. Gates, D. Kapec, A. Lupsasca, Y. Shi, and A. Strominger, "Polarization Whorls from M87* at the Event Horizon Telescope," *Proc. Roy. Soc. Lond. A* **476** (2020) 20190618, `arXiv:1809.09092 [hep-th]`.

[95] D. Muhleman and I. Johnston, "Radio propagation in the solar gravitational field," *Physical Review Letters* **17** no. 8, (1966) 455.

[96] D. Muhleman, R. Ekers, and E. Fomalont, "Radio interferometric test of the general relativistic light bending near the sun," *Physical Review Letters* **24** no. 24, (1970) 1377.

[97] G. S. Bisnovatyi-Kogan and O. Yu. Tsupko, "Gravitational lensing in a non-uniform plasma," *Mon. Not. Roy. Astron. Soc.* **404** (2010) 1790–1800, `arXiv:1006.2321 [astro-ph.CO]`.

[98] A. Rogers, "Frequency-dependent effects of gravitational lensing within plasma," *Mon. Not. Roy. Astron. Soc.* **451** no. 1, (2015) 17–25, `arXiv:1505.06790 [gr-qc]`.

[99] V. Morozova, B. Ahmedov, and A. Tursunov, "Gravitational lensing by a rotating massive object in a plasma," *Astrophysics and Space Science* **346** no. 2, (2013) 513–520.

[100] C. A. Benavides-Gallego, A. A. Abdujabbarov, and C. Bambi, "Gravitational lensing for a boosted Kerr black hole in the presence of plasma," *Eur. Phys. J.* **C78** no. 9, (2018) 694, `arXiv:1804.09434 [gr-qc]`.

[101] J. Schee, Z. Stuchlík, B. Ahmedov, A. Abdujabbarov, and B. Toshmatov, "Gravitational lensing by regular black holes surrounded by plasma," *Int. J. Mod. Phys.* **D26** no. 5, (2017) 1741011.

[102] G. Crisnejo and E. Gallo, "Weak lensing in a plasma medium and gravitational deflection of massive particles using the Gauss-Bonnet theorem. A unified treatment," *Phys. Rev.* **D97** no. 12, (2018) 124016, `arXiv:1804.05473 [gr-qc]`.

[103] G. Bisnovatyi-Kogan and O. Tsupko, "Gravitational Lensing in Presence of Plasma: Strong Lens Systems, Black Hole Lensing and Shadow," *Universe* **3** no. 3, (2017) 57.

[104] V. Perlick, O. Yu. Tsupko, and G. S. Bisnovatyi-Kogan, "Influence of a plasma on the shadow of a spherically symmetric black hole," *Phys. Rev.* **D92** no. 10, (2015) 104031, `arXiv:1507.04217 [gr-qc]`.

[105] F. Atamurotov, B. Ahmedov, and A. Abdujabbarov, "Optical properties of black holes in the presence of plasma: shadow," *Phys. Rev.* **D92** (2015) 084005, `arXiv:1507.08131 [gr-qc]`.

[106] A. Abdujabbarov, B. Toshmatov, Z. Stuchlík, and B. Ahmedov, "Shadow of the rotating black hole with quintessential energy in the presence of plasma," *Int. J. Mod. Phys.* **D26** no. 06, (2016) 1750051, `arXiv:1512.05206 [gr-qc]`.

[107] V. Perlick and O. Yu. Tsupko, "Light propagation in a plasma on Kerr spacetime: Separation of the Hamilton-Jacobi equation and calculation of the shadow," *Phys. Rev.* **D95** no. 10, (2017) 104003, `arXiv:1702.08768 [gr-qc]`.

[108] A. Abdujabbarov, B. Juraev, B. Ahmedov, and Z. Stuchlík, "Shadow of rotating wormhole in plasma environment," *Astrophys. Space Sci.* **361** no. 7, (2016) 226.

[109] Y. Huang, Y.-P. Dong, and D.-J. Liu, "Revisiting the shadow of a black hole in the presence of a plasma," *Int. J. Mod. Phys.* **D27** no. 12, (2018) 1850114, `arXiv:1807.06268 [gr-qc]`.

[110] A. Eckart and R. Genzel, "Observations of stellar proper motions near the Galactic Centre," *Nature* **383** (1996) 415–417.

[111] J. Casares, "Observational evidence for stellar-mass black holes," *IAU Symp.* **238** (2007) 3–12, `arXiv:astro-ph/0612312 [astro-ph]`.

[112] R. Narayan and J. E. McClintock, "Observational Evidence for Black Holes," `arXiv:1312.6698 [astro-ph.HE]`.

[113] R.-S. Lu, A. E. Broderick, F. Baron, J. D. Monnier, V. L. Fish, S. S. Doeleman, and V. Pankratius, "Imaging the Supermassive Black Hole Shadow and Jet Base of M87 with the Event Horizon Telescope," *Astrophys. J.* **788** (2014) 120, `arXiv:1404.7095 [astro-ph.IM]`.

[114] D. Psaltis, F. Ozel, C.-K. Chan, and D. P. Marrone, "A General Relativistic Null Hypothesis Test with Event Horizon Telescope Observations of the black-hole shadow in Sgr A*," *Astrophys. J.* **814** no. 2, (2015) 115, `arXiv:1411.1454 [astro-ph.HE]`.

[115] T. Johannsen, A. E. Broderick, P. M. Plewa, S. Chatzopoulos, S. S. Doeleman, F. Eisenhauer, V. L. Fish, R. Genzel, O. Gerhard, and M. D. Johnson, "Testing General Relativity with the Shadow Size of Sgr A*," *Phys. Rev. Lett.* **116** no. 3, (2016) 031101, `arXiv:1512.02640 [astro-ph.GA]`.

[116] A. Ricarte and J. Dexter, "The Event Horizon Telescope: exploring strong gravity and accretion physics," *Mon. Not. Roy. Astron. Soc.* **446** (2015) 1973–1987, `arXiv:1410.2899 [astro-ph.HE]`.

[117] D. Psaltis, N. Wex, and M. Kramer, "A Quantitative Test of the No-Hair Theorem with Sgr A* using stars, pulsars, and the Event Horizon Telescope," *Astrophys. J.* **818** no. 2, (2016) 121, `arXiv:1510.00394 [astro-ph.HE]`.

[118] P. V. P. Cunha, C. A. R. Herdeiro, and M. J. Rodriguez, "Does the black hole shadow probe the event horizon geometry?," *Phys. Rev.* **D97** no. 8, (2018) 084020, `arXiv:1802.02675 [gr-qc]`.

[119] Y. Mizuno, Z. Younsi, C. M. Fromm, O. Porth, M. De Laurentis, H. Olivares, H. Falcke, M. Kramer, and L. Rezzolla, "The Current Ability to Test Theories of Gravity with Black Hole Shadows," *Nature Astron.* **2** no. 7, (2018) 585–590, `arXiv:1804.05812 [astro-ph.GA]`.

[120] F. Moura and R. Schiappa, "Higher-derivative corrected black holes: Perturbative stability and absorption cross-section in heterotic string theory," *Class. Quant. Grav.* **24** (2007) 361–386, `arXiv:hep-th/0605001 [hep-th]`.

[121] D. Ayzenberg and N. Yunes, "Slowly-Rotating Black Holes in Einstein Dilaton Gauss-Bonnet Gravity: Quadratic Order in Spin Solutions," *Phys. Rev. D* **90** (2014) 044066, `arXiv:1405.2133 [gr-qc]`. [Erratum: Phys.Rev.D 91, 069905 (2015)].

[122] S. Capozziello and M. Francaviglia, "Extended Theories of Gravity and their Cosmological and Astrophysical Applications," *Gen. Rel. Grav.* **40** (2008) 357–420, `arXiv:0706.1146 [astro-ph]`.

[123] R. C. Myers and M. J. Perry, “Black Holes in Higher Dimensional Space-Times,” *Annals Phys.* **172** (1986) 304.

[124] L. Amarilla, E. F. Eiroa, and G. Giribet, “Null geodesics and shadow of a rotating black hole in extended Chern-Simons modified gravity,” *Phys. Rev.* **D81** (2010) 124045, `arXiv:1005.0607 [gr-qc]`.

[125] A. Abdujabbarov, F. Atamurotov, Y. Kucukakca, B. Ahmedov, and U. Camci, “Shadow of Kerr-Taub-NUT black hole,” *Astrophys. Space Sci.* **344** (2013) 429–435, `arXiv:1212.4949 [physics.gen-ph]`.

[126] B. Famaey and S. McGaugh, “Modified Newtonian Dynamics (MOND): Observational Phenomenology and Relativistic Extensions,” *Living Rev. Rel.* **15** (2012) 10, `arXiv:1112.3960 [astro-ph.CO]`.

[127] J. W. Moffat and S. Rahvar, “The MOG weak field approximation and observational test of galaxy rotation curves,” *Mon. Not. Roy. Astron. Soc.* **436** (2013) 1439–1451, `arXiv:1306.6383 [astro-ph.GA]`.

[128] J. W. Moffat and S. Rahvar, “The MOG weak field approximation - II. Observational test of Chandra X-ray clusters,” *Mon. Not. Roy. Astron. Soc.* **441** no. 4, (2014) 3724–3732, `arXiv:1309.5077 [astro-ph.CO]`.

[129] J. Moffat and V. Toth, “Modified Gravity: Cosmology without dark matter or Einstein’s cosmological constant,” `arXiv:0710.0364 [astro-ph]`.

[130] D. Pérez, F. G. Lopez Armengol, and G. E. Romero, “Accretion disks around black holes in Scalar-Tensor-Vector Gravity,” *Phys. Rev.* **D95** no. 10, (2017) 104047, `arXiv:1705.02713 [astro-ph.HE]`.

[131] J. R. Mureika, J. W. Moffat, and M. Faizal, “Black hole thermodynamics in MOdified Gravity (MOG),” *Phys. Lett.* **B757** (2016) 528–536, `arXiv:1504.08226 [gr-qc]`.

[132] J. W. Moffat, “LIGO GW150914 and GW151226 gravitational wave detection and generalized gravitation theory (MOG),” *Phys. Lett.* **B763** (2016) 427–433, `arXiv:1603.05225 [gr-qc]`.

[133] F. G. Lopez Armengol and G. E. Romero, “Effects of Scalar-Tensor-Vector Gravity on relativistic jets,” *Astrophys. Space Sci.* **362** no. 11, (2017) 214, `arXiv:1611.09918 [astro-ph.HE]`.

[134] H.-C. Lee and Y.-J. Han, “Innermost stable circular orbit of Kerr-MOG black hole,” *Eur. Phys. J.* **C77** no. 10, (2017) 655, `arXiv:1704.02740 [gr-qc]`.

[135] M. Sharif and M. Shahzadi, “Particle Dynamics Near Kerr-MOG Black Hole,” *Eur. Phys. J.* **C77** no. 6, (2017) 363, `arXiv:1705.03058 [gr-qc]`.

[136] M. Roshan, “Stellar Bar evolution in the absence of dark matter halo,” *Astrophys. J.* **854** no. 1, (2018) 38, `arXiv:1801.08592 [astro-ph.GA]`.

[137] L. Manfredi, J. Mureika, and J. Moffat, “Quasinormal Modes of Static Modified Gravity (MOG) Black Holes,” *J. Phys. Conf. Ser.* **942** no. 1, (2017) 012014.

[138] S. Rahvar and J. Moffat, “Propagation of Electromagnetic Waves in MOG: Gravitational Lensing,” *Mon. Not. Roy. Astron. Soc.* **482** no. 4, (2019) 4514–4518, `arXiv:1807.07424 [gr-qc]`.

[139] P. Sheoran, A. Herrera-Aguilar, and U. Nucamendi, “Mass and spin of a Kerr black hole in modified gravity and a test of the Kerr black hole hypothesis,” *Phys. Rev. D* **97** no. 12, (2018) 124049, `arXiv:1712.03344 [gr-qc]`.

[140] C. Bambi, K. Freese, S. Vagnozzi, and L. Visinelli, “Testing the rotational nature of the supermassive object M87* from the circularity and size of its first image,” *Phys. Rev. D* **100** no. 4, (2019) 044057, arXiv:1904.12983 [gr-qc].

[141] V. I. Dokuchaev and N. O. Nazarova, “Event horizon image within black hole shadow,” *J. Exp. Theor. Phys.* **128** no. 4, (2019) 578–585, arXiv:1804.08030 [astro-ph.HE].

[142] V. I. Dokuchaev, N. O. Nazarova, and V. P. Smirnov, “Event horizon silhouette: implications to supermassive black holes in the galaxies M87 and Milky Way,” *Gen. Rel. Grav.* **51** no. 6, (2019) 81, arXiv:1903.09594 [astro-ph.HE].

[143] J. An, J. Peng, Y. Liu, and X.-H. Feng, “Kerr-Sen Black Hole as Accelerator for Spinning Particles,” *Phys. Rev.* **D97** no. 2, (2018) 024003, arXiv:1710.08630 [gr-qc].

[144] G. N. Gyulchev and S. S. Yazadjiev, “Kerr-Sen dilaton-axion black hole lensing in the strong deflection limit,” *Phys. Rev.* **D75** (2007) 023006, arXiv:gr-qc/0611110 [gr-qc].

[145] Z. Younsi, A. Zhidenko, L. Rezzolla, R. Konoplya, and Y. Mizuno, “New method for shadow calculations: Application to parametrized axisymmetric black holes,” *Phys. Rev.* **D94** no. 8, (2016) 084025, arXiv:1607.05767 [gr-qc].

[146] K. Hioki and U. Miyamoto, “Hidden symmetries, null geodesics, and photon capture in the Sen black hole,” *Phys. Rev. D* **78** (2008) 044007, arXiv:0805.3146 [gr-qc].

[147] S. Dastan, R. Saffari, and S. Soroushfar, “Shadow of a Kerr-Sen dilaton-axion Black Hole,” arXiv:1610.09477 [gr-qc].

[148] S. V. M. Xavier, P. V. Cunha, L. C. Crispino, and C. A. Herdeiro, “Shadows of charged rotating black holes: Kerr-Newman versus Kerr-Sen,” in *5th Amazonian Symposium on Physics: Celebrating 100 years of the first experimental tests of General Relativity*. 3, 2020. arXiv:2003.14349 [gr-qc].

[149] S. E. Gralla and A. Lupsasca, "Lensing by Kerr Black Holes," *Phys. Rev. D* **101** no. 4, (2020) 044031, `arXiv:1910.12873 [gr-qc]`.

[150] E. Himwich, M. D. Johnson, A. Lupsasca, and A. Strominger, "Universal polarimetric signatures of the black hole photon ring," *Phys. Rev. D* **101** no. 8, (2020) 084020, `arXiv:2001.08750 [gr-qc]`.

[151] V. Perlick, O. Y. Tsupko, and G. S. Bisnovatyi-Kogan, "Black hole shadow in an expanding universe with a cosmological constant," *Phys. Rev. D* **97** no. 10, (2018) 104062, `arXiv:1804.04898 [gr-qc]`.